A_2B_2 Porphyrin dyes for photodynamic anticancer and antimicrobial therapy

A thesis submitted in fulfilment of the requirements for the degree of

Masters in Chemistry

RHODES UNIVERSITY
Where leaders learn

By

Vuyokazi Nobatana

Supervisor: Dist. Professor T. Nyokong

March 2025

Acknowledgement

I am deeply indebted to my supervisor**, Distinguished Professor Tebello Nyokong,** for her invaluable guidance, patience, understanding, and advice throughout my MSc; thank you for all the guidance and support.

Special thanks to Dr Nnamdi Nwahara, Mr James Oyim and Dr Azole Sindelo, thank you for your guidance. Thank you to Miss Gail Cobus for all the administrative work and support. My gratitude also goes to Dr J Britton, Papa Francis, Prof J Mack, INI colleagues, Rhodes University and the Ada & Bertie Levenstein funding.

Special thanks to my family for your love, prayers, and support. my parents, Siphokazi Joyce and Silumko Jack Nobatana, and my lovely siblings Thamsanqa, Siyabulela, and Aminathi Nobatana.

Abstract

The search for alternative treatments and non-toxic photosensitiser drugs that can effectively produce cytotoxic reactive oxygen species for biomedical applications, such as in alternative photodynamic therapy (PDT) for cancer treatment and photodynamic antimicrobial therapy (aPDT) for drug-resistant bacteria treatment, is increasing. This thesis reports on the synthesis, characterization, and photo physiochemical properties of A_2B_2 asymmetrical porphyrins. The synthesized porphyrins were conjugated to gold nanoparticles (AuNPs) and gold-coated silica nanoparticles ($AuSiO_2$) as potential photosensitizers for photodynamic anticancer and antibacterial therapy. The asymmetrical porphyrin complexes (**1)** 10,20-di(thiophene-2-yl)-5,15-diyl) dimorpholine porphyrin, complex (**3)** 5,15-Bis(4-(methylthio) phenyl)-10,20-di(pyridine-4-yl) porphyrin and their zinc derivates were conjugated on both AuNPs and $AuSiO_2$NPs through the Au-sulfur/nitrogen bond. The effect of the zinc metal was studied by comparing complex **1** to its zinc complex (**2**) and complex **3** to its zinc complex (**4**). It was observed that the zinc complexes had better singlet oxygen production as compared to their unmetalled complexes (**1** and **3**).

The photothermal activity of AuNPs and their conjugates were investigated, and a temperature increase in the porphyrins upon conjugation was observed. The lipophilicity and hydrophilicity of the porphyrins were also studied; complexes (**3** and **4**) with nitrogen substituents were found to be more lipophilic and porphyrin complexes (**1** and **2**) with oxygen substituents were found to be more hydrophobic. It was observed that the conjugation of porphyrins to the NPs enhanced the singlet oxygen quantum yield, PDT and aPDT activity. AuNPs conjugates overall had PDT and aPDT activity when compared to $AuSiO_2$ conjugates.

Table of Contents

CHAPTER ONE

CHAPTER TWO

CHAPTER THREE

CHAPTER FOUR

CHAPTER FIVE

CHAPTER SIX

List of abbreviations

AuNPs	Gold nanoparticles
$AuSiO_2$	Gold-coated silica nanoparticles
DLS	Dynamic light scattering
FT-IR	Fourier-transform infrared spectroscopy
HOMO	Highest occupied molecular orbitals
ISC	Intersystem crossing
LED	Light-emitting diode
LUMO	Lowest unoccupied molecular orbitals
MALDI-TOF	Matrix-assisted laser desorption ionization- Time of flight
MW	Microwave
MDA-MB 231	MD Anderson - Metastatic Breast - 231
MSSA	Methicillin-Sensitive *Staphylococcus aureus*
MRSA	Methicillin-Resistant *Staphylococcus aureus*
PDT	Photodynamic therapy
aPDT	antimicrobial Photodynamic therapy
PS	photosensitizer
PDI	Polydispersity index
1H-NMR	Proton Nuclear Magnetic Resonance
ROS	Reactive oxygen species
RT	Room temperature
UV-Vis	Ultraviolet-visible spectroscopy
XPS X-ray	Photoelectron spectroscopy

XRD	X-ray powder diffraction

List of symbols

α	Alpha
β	Beta
τ_F	Fluorescence lifetime
ϕ_F	Molar extinction coefficient
ε	Molar extinction coefficient
S_1	Singlet excited state
S_0	Singlet ground state
ϕ_Δ	Singlet oxygen quantum yield
τ_T	Triplet lifetime
λ	Wavelength
ζ	Zeta potential

Preamble

Public healthcare is at present dealing with a slew of issues relating to life-threatening illnesses, including cancer, as well as the rise of bacterial infections that are resistant to antibiotics. Researchers are looking for alternative methods of bacterial mitigation that have little to no risk of long-term resistance development. As an example, hospitals in the United States reported a significant rise in methicillin-resistant bacteria in 2013, including isolates of *Staphylococcus aureus* spa Type t002 [**1-4**]. These issues will result in significant additional morbidity and mortality in the coming decades if alternative ways are not discovered. Cancer remains one of the top causes of illness and mortality globally. Several cancer treatment plans have been used, but traditional chemotherapy has drawbacks such as poor specificity and selectivity [**5,6**]. Photodynamic therapy (PDT) and antimicrobial photodynamic therapy (aPDT) have been developed in recent decades as alternative anti-cancer and anti-bacterial treatments, respectively, due to their several benefits over traditional medicines such as chemotherapy [**7**].

This thesis reports on the conjugation of novel *trans*-A_2B_2 porphyrins to gold nanoparticles and gold-coated silica nanoparticles, with the aim of reducing aggregation, improving physicochemical characteristics, drug solubility, drug delivery and cancer cell selectivity against the MDA-MB-231 cancer cell line and methicillin-sensitive *Staphylococcus aureus* (MSSA) and methicillin-resistant *Staphylococcus aureus* (MRSA) bacterial strains.

Chapter one

Introduction

This chapter provides a broad overview of the thesis research project. It contains goals, objectives and a brief review of the synthesis, photophysicochemical characteristics, and singlet oxygen uses of porphyrin dyes.

1.1 Background

Cancer is the leading cause of death in all nations, accounting for more than 5 million deaths per year. Every year, almost ten million people are diagnosed with cancer worldwide [**8**]. In 2019, cancer killed more people than diabetes, neurological diseases, tuberculosis, and AIDS combined [**9**]. According to the World Health Organisation (WHO), in 2022, there were an estimated 20 million new cancer cases, with 9.7 million deaths, and over 35 million new cases are predicted by 2050 [**10**]. Female breast cancer is ranked as the second most common cancer worldwide, followed by colorectal cancer [**10**]. Triple-negative breast cancer (such as MDA-MB 231 and MDA-MB-468) accounts for 15–25% of all breast cancers [**11**]. As a result, there is a constant need to enhance or create new alternative treatments that can address this issue, preferably without the adverse effects associated with existing treatments like chemotherapy, surgery and radiotherapy.

Photodynamic therapy has long been recognised as a promising minimally invasive cancer treatment approach that employs non-toxic light-absorbing photosensitiser dyes (PS), light of the right wavelength (620 nm-850 nm) and reactive oxygen species (ROS) [**12-14**]. PDT is less expensive and kinder, with minor damage to non-malignant somatic cells [**15]**. The PDT technique involves the systematic administration of a photosensitiser dye that is specifically targeted to the tumour region, followed by irradiation with laser light of the appropriate wavelength to trigger a series of photochemical reactions that result in the production of cytotoxic singlet oxygen and other ROS, which kill the target tumour cells. Additionally, this procedure triggers immune reactions [**12-18]**.

The Jablonski diagram in **Scheme 1.1** can be used to demonstrate the technique for producing singlet oxygen and the photochemical reactions involved in PDT by a porphyrin. After the PS is administrated to the tumour cells, a light of a suitable wavelength is used to irradiate the cells. The PS in the ground single state (S_0) absorbs energy upon irradiation to occupy the first excited single state (S_1). The PS in the excited single state might either proceed through the intersystem crossing (ISC) to occupy the triplet state or fluoresce back to the ground single state. In the triplet manifold, the PS either experiences phosphorescence to revert to the S_0 state via emission of a photon or Type **I** and Type **II** electron and energy transfer pathways, respectively to produce ROS. Type **I** refers to the direct transfer of a proton or electron from a triplet-state PS or biomolecule to an oxygen molecule to produce ROS. The type **II** reaction involves the transfer of energy from PS in the triplet state to the ground state molecular oxygen ($^1O_2$), culminating in the formation of singlet oxygen.

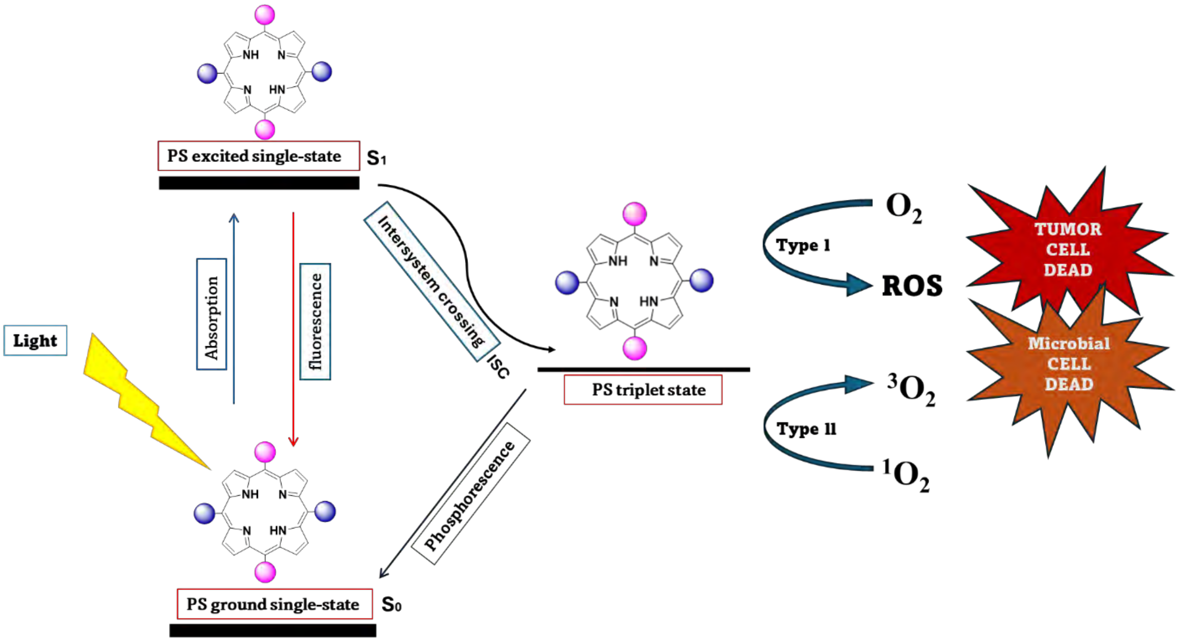

Scheme 1.1 A Jablonski diagram demonstrating the photo physicochemical processes of a PS dye following photoexcitation: absorption, fluorescence, intersystem crossing, triplet excited state, and phosphorescence.

The increasing antibiotic resistance microorganisms in hospital bacteria (such as *Staphylococcus aureus*) is a major problem for medical personnel, necessitating the development of novel antimicrobial therapies [**19**]. aPDT is a closely related approach to PDT that employs the same fundamental principle to inactivate or kill microbial cells, bacteria, and other infectious agents. aPDT inactivates bacteria by damaging their outer membranes [**20-24**]. The effectiveness of bacterial inactivation and the penetration of photosensitiser drugs into the inner membranes are largely determined by the type of bacteria and the porosity of their cytoplasmic outer membrane [**20-24**]. The absence of the protective layer (lipopolysaccharides) in the Gram- (+) bacterium (e.g. *S. aureus*) cell membrane renders it more sensitive to PSs; this is due to the existence of a rather porous layer of lipoteichoic acid and peptidoglycan with no outer membrane. aPDT is currently utilised mostly to treat mouth infections and sterilise blood products, and it is reported to be more effective than antibiotics and/or does not produce antibiotic-resistant bacterial strains [**25**]. aPDT is a viable alternative to standard antibiotics because of its capacity to treat microbial illnesses sequentially while preventing antimicrobial resistance.

This research study, therefore, sought to investigate the PDT and aPDT activities of the synthesized photosensitizer dyes (porphyrins) against triple-negative cancer cells and Gram-(+) bacterial cells, *S. aureus*.

1.2 Porphyrins

1.2.1 Porphyrin history

Porphyrins are tetrapyrrolic pigments that are widely recognised for their relevance in natural structures [**26**]. Porphyrins have been studied for decades in numerous sectors, including biomedical research dating back to the early 1840s when haemoglobin was treated with strong sulphuric acid to produce iron-free haematin [**27**]. In 1871, Hoppe-Seyler and Stokvi's termed the molecule 'hematoporphyrin' after its purple tint [**28,29**]. Küster postulated the proper structure of porphyrins as a tetrapyrrole macrocycle linked by four methine bridges in 1912 [**30**]. A porphyrin is a heterocyclic macrocyclic chemical molecule composed of four pyrroles connected by a methane bridge (=CH-) to form a heteroaromatic 16 atom 18-π electron system on the inner ligand perimeter as illustrated in **Fig**. **1.1** [**31**].

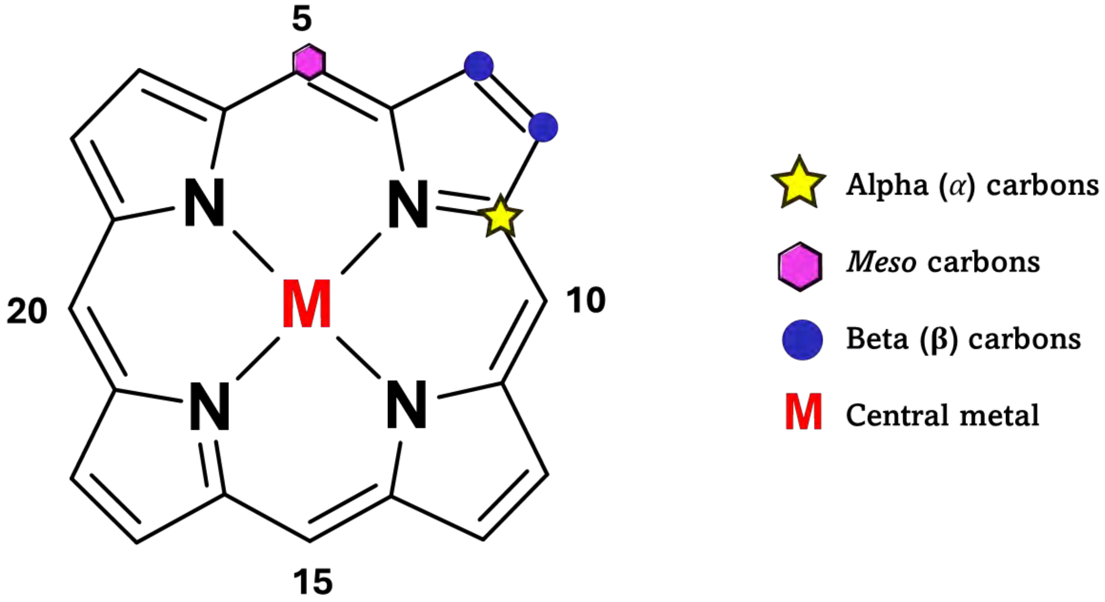

Fig. 1.1 Schematic representation of free base porphyrin macrocycle with Alpha (***α***), *Meso* and Beta(***β***) structural positions metalated with central metal (**M**).

Porphyrins are stable molecules capable of coordinating metals. Porphyrin structures have three substitution points: β, α, and *meso*, depending on their relative proximity to the core nitrogen atoms. Two NH protons are aligned in an opposite arrangement in the inner core and can be replaced by various types of central ions, primarily metal ions, to create metalloporphyrin complexes. The β- substituted porphyrin closely resembles naturally occurring porphyrins such as chlorophyll, Vitamin B12 complex, and *heme* [**31**]. Many synthetic porphyrins and porphyrins derivatives are generated using meso-aryl electrophilic substitutions; due to their aromaticity, these carbon atoms undergo a variety of electrophilic substitution processes, particularly at the meso-positions, where the electron density is high [**31-33**]. Porphyrin and its derivatives can also be functionalised with different substituent groups at the meso, beta, and core locations of the rings to suit a variety of purposes. In this study novel, trans-A_2B_2 porphyrins are employed for PDT and aPDT to address the issues related to the drug specificity and drug selectivity of porphyrin complexes.

1.2.2 Synthesis of porphyrins

Several synthetic approaches have been used to investigate electrophilic replacements at the meso-positions (the ring's 5, 10, 15, and 20 positions), where electrophilic substitutions can occur easily. These include common synthetic processes, such as the Ruthermund and Menotti, Alder-Longo, and Lindsey reaction methods, which are individually detailed below and are indicated in **Scheme 1.2**.

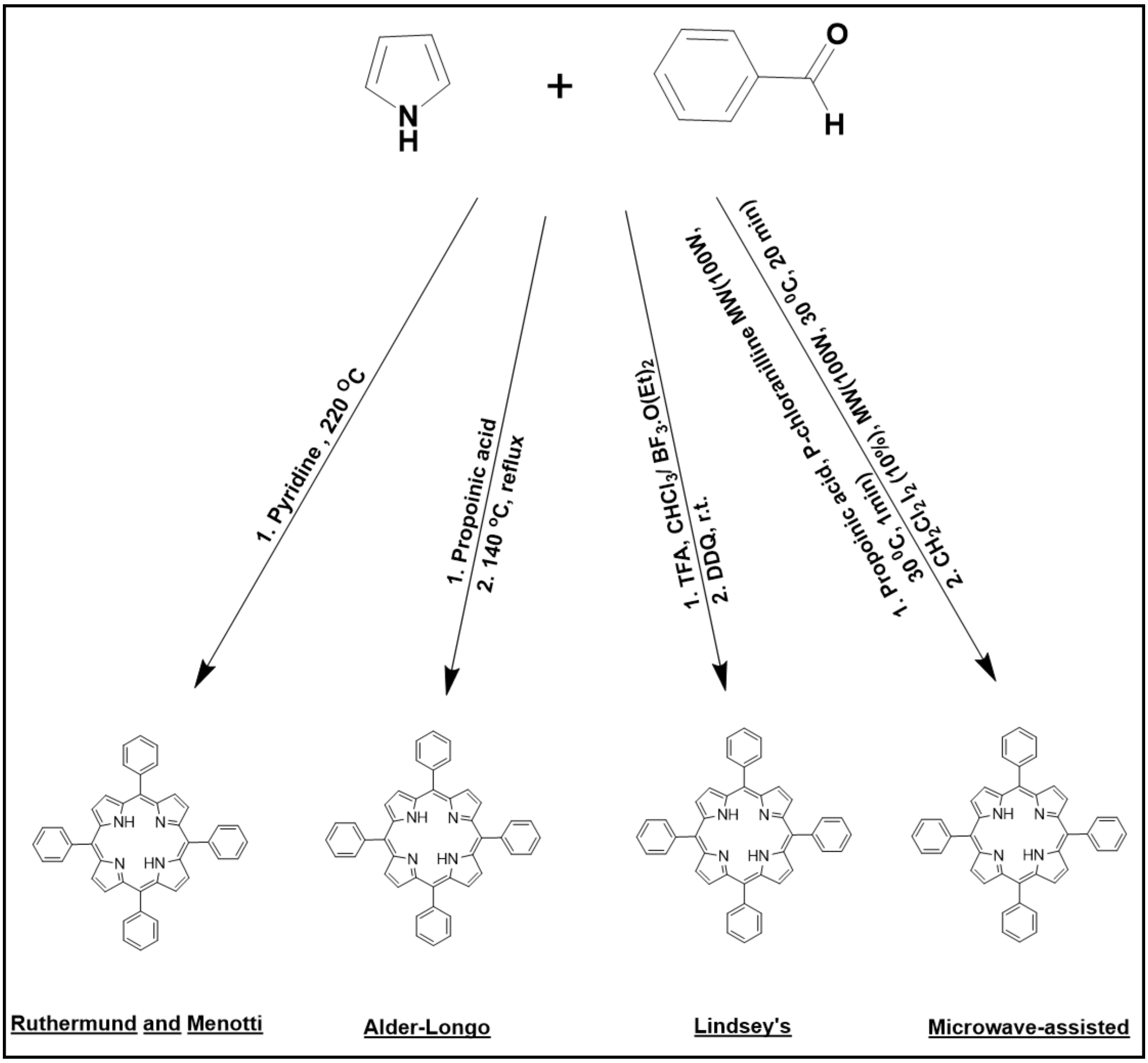

Scheme 1.2. A schematic representation of the synthesis of a free-base porphyrin employing several methods and reaction conditions: **r.t** = room temperature, **TFA** = trifluoroacetic acid, **DDQ** = 2,3-dichloro-5,6-dicyanobenzoquinone and **$BF_3.O(Et)_2$** = boron trifluoride etherate.

1.2.2.1 Rothermund and Menotti method

In 1935, Ruthermund and Menotti invented a significant synthesis procedure for symmetric free-base meso-substituted porphyrins. They heated the reaction mixture of pyrrole with benzaldehyde to 200 °C to produce a variety of meso-substituted porphyrins with a yield of about 10%. Later, they changed the reaction conditions to produce significantly greater yields. As shown in **Scheme 1.2**, they heated the sealed tubes in the presence of pyridine at a high temperature (220 °C) for 48 h, yielding 11% of the TPP [**34**].

1.2.2.2 Alde-Longo Method

Adler, Longo and coworkers developed an improved approach to synthesise meso-substituted symmetrical porphyrins to overcome the low yield challenge faced by Ruthermund and Menotti [**35,36**]. The process involved refluxing at (140 ^oC) equivalent molar amounts of pyrrole and benzaldehyde in propionic acid for 30 min in an open atmosphere. After 30 min, the red-brown solution was cooled to room temperature and filtered. This is followed by washing with methanol followed by hot water that affords purple crystals of the porphyrin with moderate yields of up to 20% (**Scheme 1.2).** Under these conditions, large-scale tetraphenyl porphyrin production was possible. The main restriction of this approach is that certain aldehydes, such as hydroxyl, thiol and amino functional groups, are sensitive to strong acid reaction conditions. In addition, recovering some porphyrin products from the reaction mixture can be problematic due to the solubility of propionic acid [**37**].

1.2.2.3 Lindsey's method

In the 1980s, Lindsey and coworkers devised a two-step procedure to accommodate aldehydes with acid-sensitive functional groups [**38**]; this method utilises equal quantities of pyrrole and benzaldehyde in the presence of an acid catalyst, typically trifluoroacetic acid (TFA) or boron trifluoride etherate ($BF_3.O(Et)_2$), employing dichloromethane as a solvent at ambient temperature under an inert atmosphere to produce a porphyrinogen intermediate complex. As indicated in **Scheme 1.2**, the porphyrinogen is then oxidised with quinines (DDQ or p-chloranil) to produce porphyrin in yields of up to 50%, depending on the aldehyde used.

Lindsey established that his approach is concentration-dependent; therefore, starting material concentrations of up to 0.01 M are recommended for maximum yield. One of the disadvantages of this approach is that large volumes of chlorinated solvents (usually CH_2Cl_2 or $CHCl_3$) are required. Lindsey's approach has a much larger scope because it can accommodate several different meso-aryl porphyrins [**39,40**].

1.2.2.4 Microwave-assisted method

Zurroaki and coworkers pioneered a microwave-assisted synthesis of meso-substituted porphyrins **[41]**, **Scheme 1.2**. This method includes a two-step synthetic microwave-activated approach to prepare B_4 or A_4 meso-tetraphenyl porphyrins. This method includes a mixture of pyrrole, benzaldehyde, and dichloromethane (DCM) in 10% molar equivalence of iodide subjected to microwave (MW) radiation, followed by the addition of p-chloranaline [**41**]. This technique provides satisfactory yields (~47%), and the reaction takes less than 30 min [**42**]. There have been reports of several solvent-free, microwave-assisted synthesis methods that produce relatively high yields quickly and don't require condensation or distillation processes [**42,43**].

1.2.2.5 Synthetic methods used in this thesis

Asymmetrical meso-substituted A_2B_2 porphyrins are less common due to their synthetic difficulties and low product yields. The methodology used in this work eliminates the need for costly oxidising agents like p-chloranil, DDQ and huge amounts of dry chlorinated solvents, contrary to the reported Lindsey's approaches. The synthesis route consists of two straightforward steps; the first step involves the condensation of pyrrole and aldehyde (A) in a molar ratio of 2:1 in a MeOH-H_2O mixture using HCl to form a dipyrromethane complex, followed by the condensation of the dipyrromethane with the second desired aldehyde (B) in an equivalent molar ratio to form the trans-A_2B_2 porphyrin.

1.2.3 Electronic absorption spectroscopy of porphyrins

Gouterman's four-orbital model, states that the two lowest unoccupied molecular orbitals (LUMOs) derived from the LUMO with $M_L = \pm 5$ nodal patterns and the two highest occupied molecular orbitals (HOMOs), derived from the HOMO of the $C_{16}H_{16}^{2-}$ species with $M_L = \pm 4$ nodal patterns produce the main porphyrin absorption bands [**44,45**]. These transitions, along with additional orbital mixing and splitting of the two energy states, result in stronger oscillations in the Soret (**B**) band, which originates from the high energy state, and weaker oscillations in the Q-bands, which originate from the lower energy state [**46**]. Because of their highly conjugated 18-π electron systems, porphyrin analogues have absorption bands in the

400-700 nm range of the electromagnetic spectrum, which give them an intense color. **Fig. 1.2** shows a standard porphyrin spectrum with a strong Soret band (B band) in the blue region at 400-500 nm from the permitted $\Delta M_L = \pm 1$ transitions, and lower absorption bands (Q bands) in the red region between 500-700 nm from the prohibited transitions of $\Delta M_L = \pm 9$ [**47**]. Due to the N-H protons splitting the symmetry, four Q-bands are seen for a free base (**Fig. 1.2**), whereas only two Q-bands are seen for a metalated porphyrin.

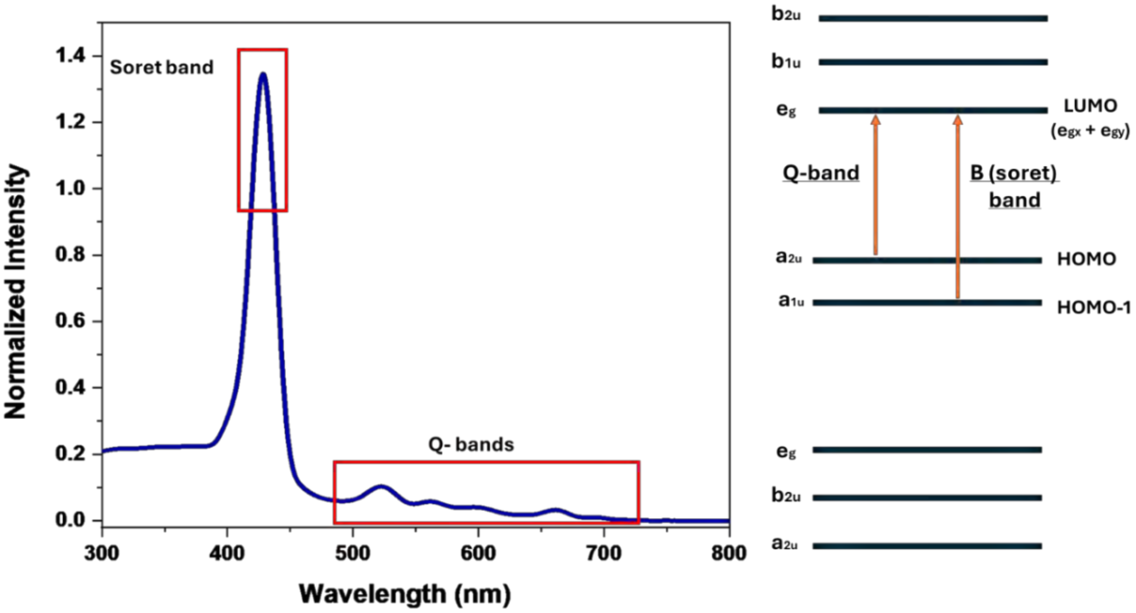

Fig. 1.2. The typical ground state absorption spectra of a free base 4,4'-(10,20-di(thiophen-2-yl)porphyrin-5,15-diyl)dimorpholine porphyrin in DMSO and the Gouterman's four orbital HOMOs and LUMOs electronic transitions showing the origin of Soret (B) band and Q-bands in a porphyrin molecule.

1.3 Photophysical and photochemical properties of porphyrins.

The photo-physicochemical processes that porphyrins go through are essential in determining whether they may be used as photosensitiser dyes in various sectors, such as PDT and aPDT. These photophysical parameters are the characteristics that a particular molecule exhibits as its energy levels transition in response to photoexcitation and can be clearly visualized by using the Jablonski diagram [**Scheme 1.1**]. The parameters being investigated include the singlet oxygen, fluorescence quantum yields and triplet state lifetimes.

1.3.1 Fluorescence quantum yields (ϕ_F)

Fluorescence occurs when a fluorophore compound is photoexcited with the light of a given wavelength, and photons are emitted with lifetimes in the ns range [**48**]. Fluorescence is characterised by Kasha's rule, which stipulates that emission takes place at the electronic state's lowest vibrational level, S_1 [**49**]. Consequently, the processes occurring in the excited states are not influenced by the wavelength of excitation. Quantifying the fluorescence quantum yield (ϕ_F) is one of the most effective ways to assess the effectiveness of photosensitisers for different applications, which is the ratio of photons absorbed to photons released through fluorescence, **Eq. 1.1** [**50,51]**.

$$\phi_F = \frac{\textbf{number of photons emitted}}{\textbf{number of protons absorbed}} \qquad \textbf{Eq. 1.1}$$

In this work, a comparative method (**Eq. 1.2**) was used to evaluate fluorescence quantum yields as published in the literature [**52**] using zinc tetraphenylporphyrin (ZnTPP) as a standard with ($\phi_F^{st} = 0.303$) [**53**] in dimethyl sulfoxide (DMSO).

$$\phi_F = \phi_F^{st} \frac{F.A^{std}.n^2}{F^{std}.A\,(n^{std})^2} \qquad \textbf{Eq. 1.2}$$

where F and F_{Std}, respectively, represent the areas under the sample's and standard's fluorescence curves. The absorbances of the sample and standard at the excitation wavelength are denoted by A and A_{Std}, respectively. The refractive indices of the solvent used for the sample and standard are denoted by n and n_{Std}, respectively.

1.3.2 Singlet oxygen quantum yield (ϕ_Δ)

The main goal in the development of photosensitisers for phototherapeutic methods is the effective generation of singlet oxygen [**54**]. In phototherapeutic applications, singlet oxygen ($^1O_2$) is the primary cytocidal agent that is essential for initiating a series of biochemical reactions leading to apoptosis, necrosis and autophagy, or bacterial death [**11-13,15-17**]. The short-lived singlet oxygen species are created when an electrically excited PS in the triplet state interacts with molecular oxygen ($^3O_2$). These species set off a series of biochemical events that eventually cause tissue damage and cell death [**40,55-57**]. The quantitatively determined quantity known as singlet oxygen quantum yield (ϕ_Δ) is dependent on how well the molecule transfers its absorbed energy to ground-state molecular oxygen ($^3O_2$) to produce singlet oxygen ($^1O_2$) [**58**].

In this work, ϕ_Δ was determined by using 9,10-dimethylanthracene (DMA) as a singlet oxygen quencher and ZnTPP (ϕ_Δ= 0.53) serving as a reference [**59**], in DMSO, using **Eq. 1.3.**

$$\boldsymbol{\Phi}_\Delta = \boldsymbol{\Phi}_{\Delta}^{Std} \cdot \frac{\mathbf{B.I^{Std}}}{\mathbf{B^{Std}.I}} \qquad \textbf{Eq. 1.3}$$

where B and B_{Std} represent the singlet oxygen quencher's photobleaching rates in the presence of the standard and the porphyrin derivatives under study, respectively. The rates of light absorption by the sample and standard are denoted by I and I_{Std}, respectively.

1.3.3 Triplet lifetimes (τ_T)

The lifetime of the photogenerated lowest excited triplet state (τ_T) can serve as a predictor of the efficiency of a photosensitiser to produce singlet oxygen due to the significance of the triplet excited state in both the Type I and II pathways responsible for the generation of ROS. This is due to the fact that longer triplet lives increases the likelihood of ground-state oxygen and the photosensitiser dyes colliding, which increases the formation of singlet oxygen. In this work, τ_T were obtained by exponential fitting the kinetic curves using the ORIGIN 8 professional software.

1.4 Different Methods of enhancing photo-physiochemical and therapeutic efficacy

Several structural alterations have been used with the purpose of increasing the optical behaviour, photo-physicochemical characteristics, and cancer/ bacterial selectivity of the porphyrins.

1.4.1 Substituents and central metals

The substituents on the porphyrin contribute to the photo-physiochemical features; substituents such as bromide, chlorine and sulphur have been found to have an internal heavy atom impact and improve the rate of intersystem crossing (ISC), which leads to larger singlet oxygen quantum yields [**60**]. The addition of central metals such as (tin, zinc, indium, gallium and others) help improve the photo-physiochemical properties through the heavy atom effect, which stimulates intersystem crossing to the triplet excited state [**61**].

1.4.2 Nanoparticles as nanocarriers

Nanoparticles (NPs) are materials with diameters ranging from 1 to 100 nanometres (nm). Compared to their bulk counterparts, their nanoscale ranges have physical and chemical features that make them attractive for innovative applications [**62**]. NPs of noble metals such as gold and silver improve characteristics for various phototherapy applications [**63-66**]. Large surface area, improved mechanical strength, and stability in chemical processes are a few of these NPs' attributes. NPs are also appealing for drug administration because of their versatility, biocompatibility, enhanced drug loading, and targeting [**67-69**]. The size and shape-dependent surface plasmon resonance (SPR) impact of metal NPs allows for efficient absorption and conversion of light energy to generate heat in photothermal therapy (PTT), which causes distress within cancer cells [**70-72**]. The NPs-drug conjugates are anticipated to target the cancer microenvironment due to the leaky vasculature around the cancer site, allowing faster entry, accumulation, and retention at cancer target sites; this is known as the enhanced permeability and retention factor (EPR) **Fig. 1.3** [**66,67**].

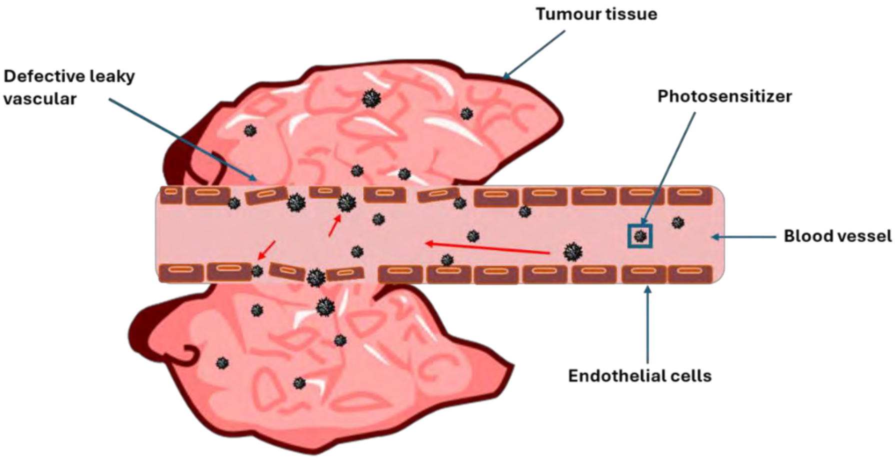

Fig. 1.3 The enhanced permeability and retention effect.

For this work, gold nanoparticles were chosen for their photothermal effect and silica in gold-coated silica nanoparticles were chosen for their stability and to enhance the aqueous solubility of nanoconjugates formed with the porphyrins. The nanoconjugates are prone to target cancer cells in PDT because of the leaky vasculature around the cancer cells, as well improve the enhanced permeability and retention effect in aPDT **[66,67]**.

1.5 Porphyrin complexes used in this work

All the porphyrin complexes that were synthesized and used in this work are outlined in **Table 1.1** and will be discussed in more detail below.

Table 1.1 Summary of all the porphyrins synthesised and employed in this study.

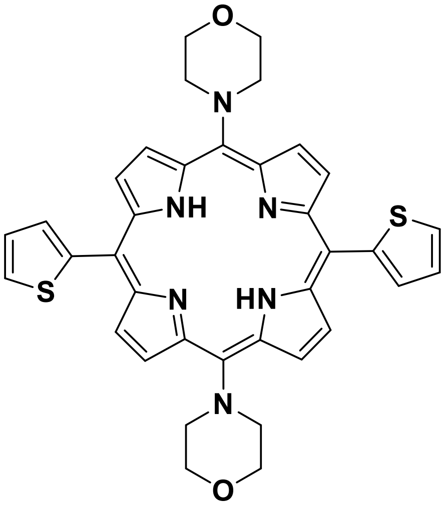 **(1)** 10,20-di(thiophene-2-yl)-5,15-diyl) dimorpholine porphyrin ***New*** Physicochemical, PDT and aPDT	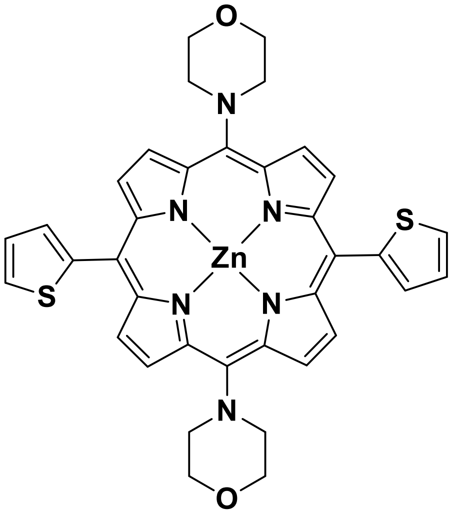 **(2)** Zinc (ii) 10,20-di(thiophene-2-yl)-5,15-diyl) dimorpholine porphyrin ***New*** Physicochemical, PDT and aPDT
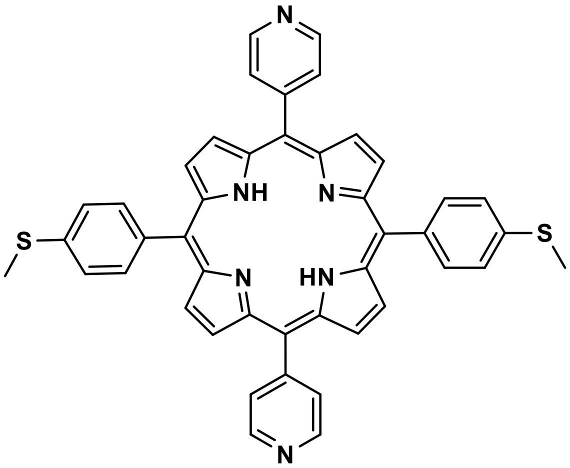 **(3)** 5,15-Bis(4-(methylthio) phenyl)-10,20-di(pyridine-4-yl) porphyrin ***New*** Physicochemical, PDT and aPDT	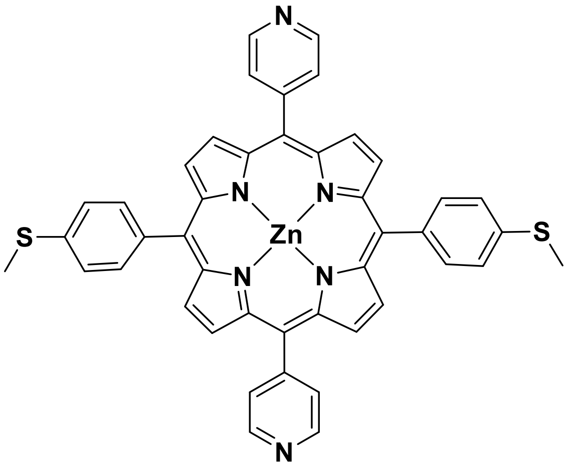 **(4)** Zinc (ii) 5,15-bis(4-(methylthio) phenyl)-10,20-di(pyridin-4-yl) porphyrin ***New*** Physicochemical, PDT and aPDT

Gold exhibits a strong affinity for sulphur and nitrogen, making it easy to conjugate complexes with sulphur **[73]** or nitrogen atoms to form nanoscale assemblies that can be used to target infections and tumours. The PDT and aPDT activities of porphyrins conjugated to gold nanoparticles with meso-thienyl, methylthiophenyl and pyridine substituents were thus evaluated in this research study. Complexes **1** and **3** were metalated with zinc for the heavy atom effect.

1.6 Nanoparticles synthesised

1.6.1 Gold nanoparticles

Gold nanoparticles (AuNPs) are microscopic gold particles that range in size from 1-100 nanometres (nm) [**65**]. They have unique features because of their small size and enormous surface area, making them particularly valuable in a range of applications. In recent years, AuNPs have gained significant attention in the field of nanomedicine, particularly for PDT and aPDT [**73-80**]. AuNPs exhibit unique optical properties, primarily due to their localized surface plasmon resonance (LSPR); When exposed to light, AuNPs absorb, and scatter light effectively, and they enhance the energy transfer to the photosensitizer leading to ROS generation. When irradiated by specific light, AuNPs can also convert light energy into heat, these properties are advantageous in photodynamic therapy and antimicrobial photodynamic therapy [**81,82**]. AuNPs have been reported to have antibacterial properties as they attach to bacteria allowing photosensitisers to bind more effectively [**83,84**]. AuNPs have also been shown to improve dye transport to treated cancer tissue due to their enhanced permeability and retention (EPR) effect [**85**] (**Fig. 1.3**).

1.6.2 Silica nanoparticles

Silica nanoparticles (SiO_2NPs) are small particles of silicon dioxide (SiO_2) with a diameter of 1–100 nm. Their distinctive qualities, such as ease of synthesis, colloidal stability, tuneable particle size, ease of surface functionalization, biocompatibility, and potentially scalable synthesis, have made them useful in a variety of disciplines of biomedicine [**85-89**]. Medical uses of SiO_2NPs for anti-cancer, anti-microbial, and theragnostic applications are especially significant because of their remarkable performance in delivering many different small molecules and pharmaceuticals (drugs, siRNA, antibodies, peptides and proteins) to specified areas [**86,87**]. Stöber and co-workers pioneered one of the early SiO_2NPs synthesis procedures, the Stöber process, in 1968. Stöber particles are solid, monodisperse SiO_2NPs with tuneable sizes. They are created by sol-gel chemistry, which involves a silica precursor, such as tetraethylorthosilicate, in water and alcohol solutions containing ammonia **[90]**. Importantly, SiO_2NPs have been demonstrated to improve the stability of different drugs without compromising their specific chemical and physical properties **[91-95].**

Gold-coated silica nanoparticles are hybrid nanomaterials that combine a core of silica (SiO_2) and a coating of AuNPs, providing the benefits of both materials. The unusual features of the silica core and gold coating give these nanoparticles tremendous potential in anticancer and antibacterial photodynamic therapy. Silica nanoparticles and gold nanoparticles are used to deliver drugs in a controlled manner **[87-96].** The silica core can encapsulate therapeutic agents, while the gold coating can enable triggered release using light to produce heat (photothermal therapy) [**65,73-85**].

1.7 Porphyrins and their corresponding conjugates are used in this work.

Porphyrins synthesised in this study are asymmetric trans-A_2B_2 porphyrins substituted with different ligands and metalled with zinc metal ions to increase their photophysical and photochemical activity and then conjugated to Au and $AuSiO_2$ nanoparticles to enhance their target delivery towards cancerous and bacterial cells. This study focuses on the photophysicochemical properties, PDT and aPDT activity of porphyrins complexes and their conjugates.

Table 1.2 [96-104] shows porphyrin complexes which have been linked to gold nanoparticles or silica nanoparticles for PDT, aPDT and biological imaging studies in literature. The table only shows porphyrins that have been conjugated to Au/ SiO_2 nanoparticles, and it is reported here for the first time porphyrin complexes conjugated to gold-coated silica nanoparticles.

Table 1.2 Porphyrins linked to gold nanoparticles and silica nanoparticles for various applications.

Porphyrin structure	**Nanoparticles and Bond**	**Application**	**Ref**
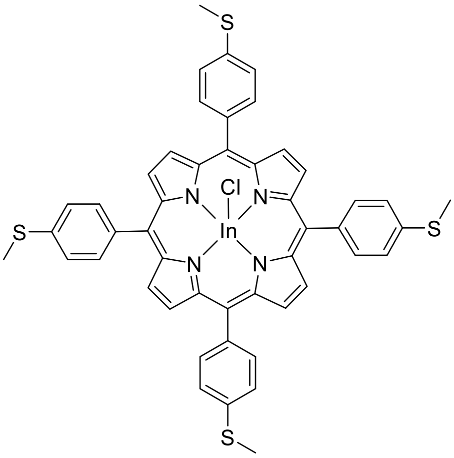	Gold nanoparticles (AuNPs) S-Au bond	Photodynamic therapy (PDT)	**[96]**
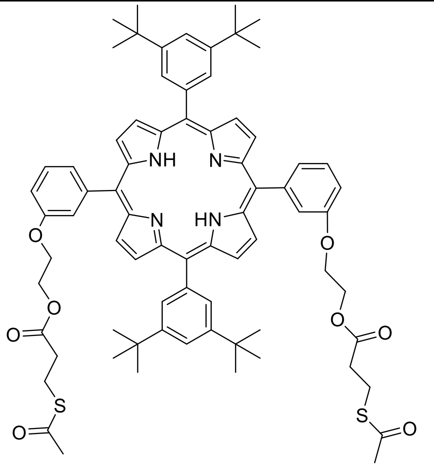	Gold nanoparticles (AuNPs)	Time-resolution fluorescence studies	**[97]**
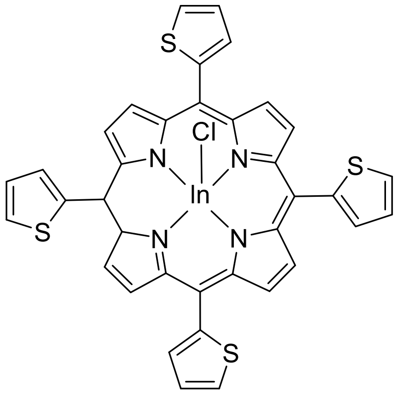	Gold nanoparticles (AuNPs) S-Au bond	Anti-microbial photodynamic therapy (aPDT)	**[98]**

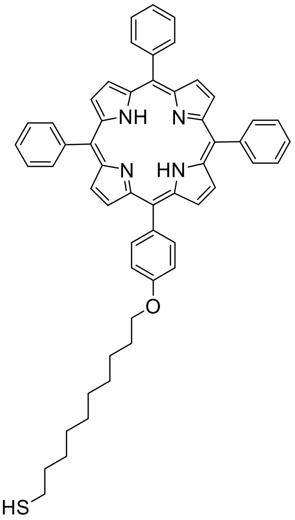	Gold nanoparticles (AuNPs) S-Au bond	Photodynamic therapy (PDT)	**[99]**
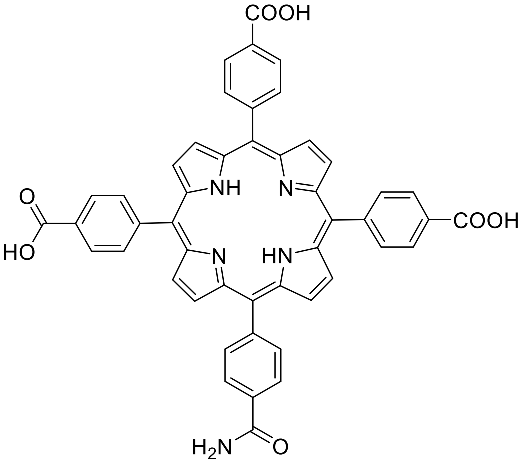	Mesoporous silica nanoparticles (MSN) Covalent linkage	Photodynamic therapy (PDT)	**[100]**
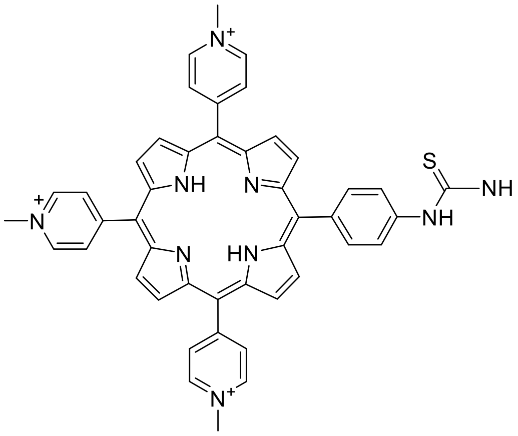	Covalently linked to porous silica nanoparticles	biological imaging	**[101]**

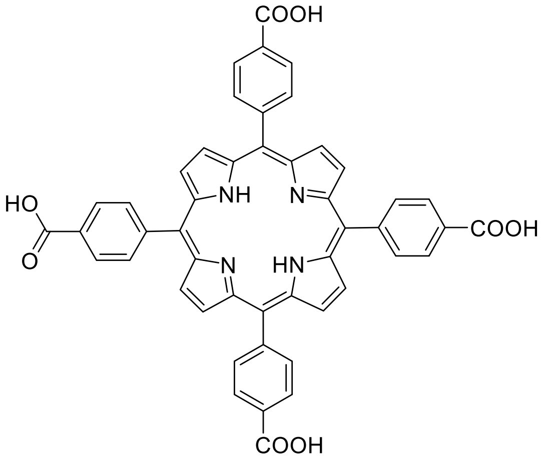	Covalently linked to silica coated magnetite nanoparticles	Anti-microbial photodynamic therapy (aPDT)	**[102]**
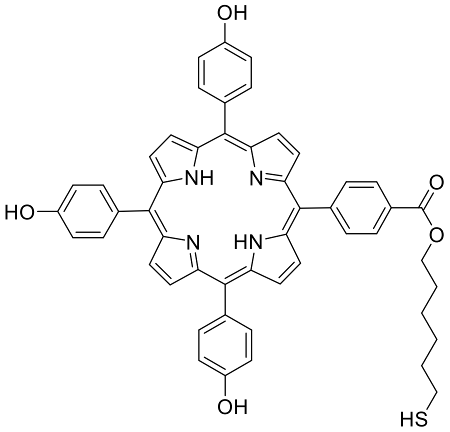	Gold nanoparticles (AuNPs) S-Au bond	Photodynamic therapy (PDT)	**[103]**
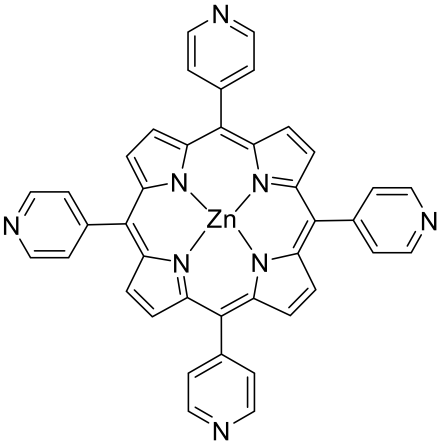	Silica nanoparticles Covalently linkage	Photodynamic therapy (PDT)	**[104]**

The thesis reports on asymmetric porphyrins, which improve aPDT and PDT activity **[105]**. **Table 1.3** outlines all the porphyrin complexes used in this work, and their conjugates to AuNPs and $AuSiO_2$ through the Au-sulfur chemical bond, and all the porphyrin and conjugates used in this work are new.

Table 1.3 Porphyrin conjugates used in this work. All complexes were studied in PDT and aPDT against Triple-negative MDA-MB 231 cancer cells and Gram-positive bacteria planktonic cells of methicillin-sensitive *Staphylococcus aureus* (MSSA) and methicillin-resistant *Staphylococcus aureus* (MRSA) bacterial cells.

Porphyrin complex	Nanoparticles and interaction	Porphyrin conjugate
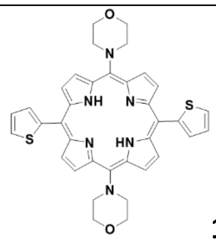 **1**	Gold nanoparticles (AuNPs) **S-Au bond**	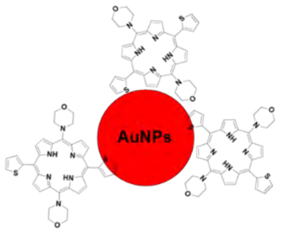 **1**-AuNPs
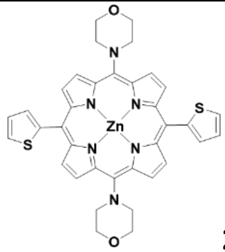 **2**	Gold nanoparticles (AuNPs) **S-Au bond**	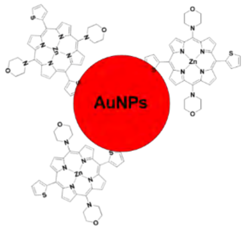 **2**-AuNPs
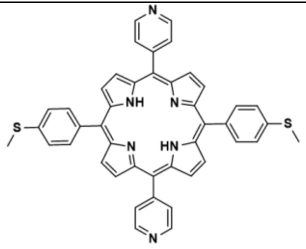 **3**	Gold nanoparticles (AuNPs) **S-Au bond**	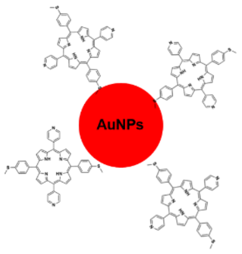 **3**-AuNPs
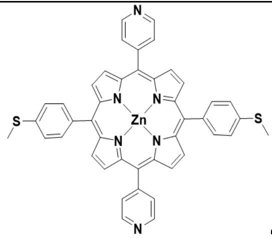 **4**	Gold nanoparticles (AuNPs) **S-Au bond**	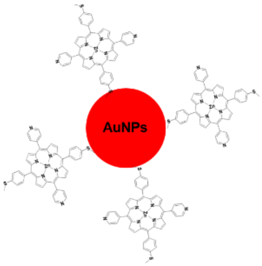

		4-AuNPs
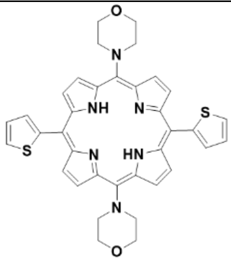 **1**	Gold-coated silica nanoparticles ($AuSiO_2$) **S-Au bond**	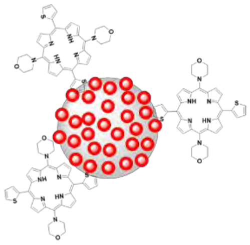 **1**-$AuSiO_2$
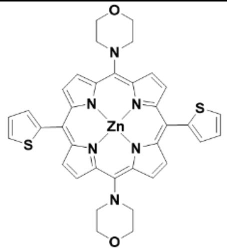 **2**	Gold-coated silica nanoparticles ($AuSiO_2$) **S-Au bond**	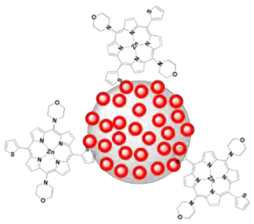 **2**-$AuSiO_2$
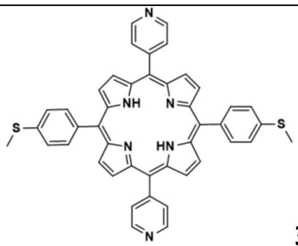 **3**	Gold-coated silica nanoparticles ($AuSiO_2$) **S-Au bond**	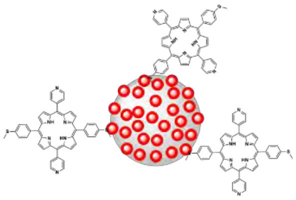 **3**-$AuSiO_2$
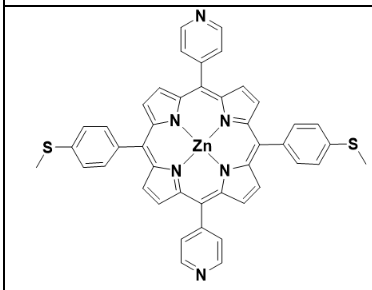 **4**	Gold-coated silica nanoparticles ($AuSiO_2$) **S-Au bond**	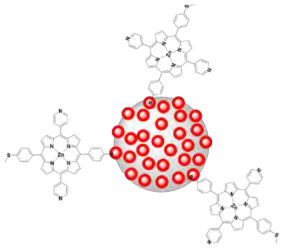 **4**-$AuSiO_2$

1.8 Thesis outline

This thesis mainly focuses on the synthesis, characterisation, and assessment of the photophysical properties of novel trans-A_2B_2 porphyrins. It is divided into four primary sections: the introduction, the experimental part, the results and discussion, and the conclusion and future perspective for the research project.

Chapter 1 is an introduction that focuses on the study's history and the difficulties it addresses. It discusses the history of using porphyrins as photosensitiser dyes and nanoparticle conjugation, including the commonly used synthetic methodologies, their fundamental photophysicochemical properties, and their use as photosensitiser drugs in PDT and aPDT treatment protocols.

Chapter 2 contains the experimental component, which includes descriptions of the instruments, materials, and experimental procedures.

Chapters 3–6 contain the results and discussion sections, which cover the synthesis and characterisation of the synthesised dyes, their optical and photophysicochemical properties, PDT and aPDT activities, conclusions, and future prospects for the work discussed.

1.9 Summary of Aims.

1. Synthesise and characterise A_2B_2 porphyrin dyes.
2. Synthesise and characterise AuNPs and AuSiO_2NPs.
3. Investigate the photothermal activity of gold nanoparticles.
4. Conjugation of porphyrins to nanoparticles using the Au-S affinity and characterisation of the resulting nanoparticle conjugates and evaluate their photophysicochemical properties.
5. aPDT activity against methicillin resistance and sensitive Gram (+) bacteria and PDT studies against MDA-MB 231 activity studies for the synthesised porphyrin dyes, nanoparticles, and their nano-conjugates.

CHAPTER TWO

Experimental

This chapter describes the materials and instruments used, as well as the synthetic procedures for the porphyrin dyes and nanoparticles, together with the characterisation methods, including the protocols for the *in vitro* PDT and aPDT activity investigations.

2.1 Materials

2.1.1 Solvents

Solvents used include chloroform, deuterated dimethylsulfoxide (DMSO-d_6), methanol (MeOH), toluene and alpha-cyano-4-hydroxycinnamic acid; all of these were obtained from Sigma-Aldrich. dichloromethane (DCM), hydrochloric acid, ethanol (EtOH), tetrahydrofuran (THF), dimethylformamide (DMF), and dimethylsulfoxide (DMSO) were purchased from Merck. Type II Millipore water was collected from an ELGA, Veolia water Purelab, flex system (Marlow, UK).

2.1.2 Chemicals and Reagents

2.1.2.1 Reagents for porphyrin synthesis

Morpholine carboxaldehyde, 4-methylthiobenzaldehyde, 2-thiophenecarboxyaldehyde, pyridine-4-carbaldehyde, pyrrole, zinc acetate dihydrate, triethylamine (TEA), hydrochloric acid (36%) and silica gel 60 (0.04-0.063 mm), was obtained from Sigma-Aldrich

2.1.2.2 Reagents for nanoparticles synthesis

Gold (III) chloride trihydrate, tetraethyl orthosilicate (TEOS), aminopropyl triethoxylsilane (APTES), and ammonium hydroxide were purchased from Sigma-Aldrich. Tri-sodium citrate was obtained from Merk.

2.1.2.3 Materials for photophysical studies

Zn 5,10,15,20-tetraphenyl-21H, 23H-porphine (ZnTPP) and 9,10 dimethylanthracene (DMA) were purchased from Sigma-Aldrich.

2.1.2.4 Reagents for cancer cell (PDT) and bacterial strain (aPDT) studies

Triton X-100, dulbecco’s phosphate-buffered saline (DPBS), trypan blue, Dulbecco’s modified eagle’s medium (DMEM), heat-inactivated fetal bovine serum (FBS, 10 % (v/v)), and trypsin were obtained from Sigma-Aldrich. Cultures of epithelial Triple-negative Breast Cancer Cell Line MDA-MB 231 were purchased from Cellonex. The bioreagent resazurin salt was purchased from Sigma-Aldrich. 100 mg mL^{-1} penicillin-100-ug. mL^{-1}-streptomycin-amphoteric B mixture was obtained from VWR.

Bacteriological BBL Muller Hinton broth and nutrient agar were purchased from Merck, the Brain heart infusion broth was purchased from Thermo Scientific, and they were all prepared according to the manufacturer's specifications. *Staphylococcus aureus* (ATCC 25923) and methicillin *Staphylococcus aureus* (ATCC 700699) were obtained from Davies Diagnostics and Microbiologics, respectively. Phosphate buffer saline (PBS 10 mM, pH 7.4) was prepared following the standard procedure using 137 mM NaCl, 10 mM $NaHPO_4$, 2.7 mM KCl, and 1.8 mM KH_2PO_4 in 1 L of type II Millipore water.

2.2 Equipment

- **The optical absorption spectra** were recorded at room temperature using a Shimadzu UV 2550 spectrophotometer with a wavelength range of 300-800 nm and a 1 cm path length cuvette.
- A Varian Eclipse spectrofluorometer was used to record **fluorescence emission and excitation spectra.** Excitation in the Soret band (crossover λ between standard and complex) and emission spectra was collected at 500-800 nm.
- **^{1}H Nuclear Magnetic Resonance (^{1}H-NMR) spectra** were recorded using a Bruker Avance II^{TM} 80 MHz and AMX 400 MHz spectrometers.
- **Mass spectral data** were acquired using a Bruker AutoFLEX III SmartbeamTOF/TOF mass spectrometer in positive ion mode, with a 354 nm nitrogen laser serving as the ionising source. The MALDI matrix included α-cyano-4-hydroxycinnamic acid.
- **The triplet state lifetime spectra** were recorded in DMSO at 470 nm using an Edinburgh Instruments LP980 spectrometer and an Ekspla NT-342B laser with an OPO to give an excitation wavelength (2.0 mJ excitation energy, 7 ns pulse duration, and

20 Hz repetition rate). The solutions were degassed with nitrogen for 30 min before measurement, and the absorbances for the Soret band were kept around 1.5. The triplet lifetimes were calculated by fitting an exponential curve to the decay curve with OriginPro 9 software.

- **Singlet oxygen quantum yields** were done using Ekspla NT 342B-20-AW laser with an Nd: YAG that pumps a 420-2300 nm optical 30 parametric oscillator (OPO) (355 nm, 2.0 mJ/7 ns, 20Hz) to provide monochromatic light at a crossover wavelength for the standard and sample. A Thermo Scientific Evolution 350 spectrometer was used to record degradation of singlet oxygen quencher (DMA) at a specific time intervals.

- **Fourier-transform infrared spectroscopy (FT-IR) spectra** were acquired using a Bruker Alpha model FT-IR spectrometer equipped with a Platinum-ATR with a range of 500-4000 cm^{-1}.

- **Dynamic light scattering (DLS)** was used to quantify the hydrodynamic diameter (Dh) and Zeta potential (ζ) of nanoparticles and nanoconjugates utilising a Malvern Zetasizer Nanoseries, Nano-ZS90 (including a 633 nm helium neon laser), disposable cuvettes, and Zeta cell.

- **X-ray powder diffraction (XRD) patterns** were acquired using a Bruker D8 discover instrument with a Lynx Eye Detector, utilising Cu Kα radiation (λ = 1.5405 A, Ni filter). Data was acquired over the 2θ = 5-100° range, scanning at 1° min^{-1}, with a filter time constant of 2.5 s per step and a 6.0 mm slit width. The samples were placed on a silicon wafer slide with zero backdrop. X-ray diffraction data was analysed with Eva (evaluation curve fitting) software. Each diffraction pattern was subjected to a baseline correction by removing a spine fitted to the curved background, and the fitted curves yielded the full width at half maximum values reported in this work.

- **The X-ray photoelectron spectroscopy (XPS)** study was performed on an AXIS Ultra DLD (provided by Kratos Analytical) with an Al (monochromatic) anode fitted with a charge neutraliser. We used the following parameters: The emission was 10 mA, the anode (HT) was set to 15 kV, and the operating pressure was less than 5 × 10^{-9} torr. A hybrid lens was employed, and the resolution for acquiring scans was adjusted at 160 eV pass energy in slot mode. The scan centre was set to 520 eV (width of 1205 eV), with 1 eV steps and a dwell time of 100 ms. High-resolution scans were collected in slot mode with 80 eV pass energy. Chemically different species were resolved using a nonlinear least squares curve fitting procedure.

- **Thermal gravimetric analysis (TGA)** was performed using a Perkin Elmer TGA 8000 thermogravimetric analyser to investigate the decomposition profiles of the porphyrin, nanoparticles, and corresponding nanoconjugates at temperatures ranging from 50 to 800 °C and nitrogen as the purge gas. Nitrogen gas purge was employed with a flow rate of 20 mL/min, and samples ranging from 1 to 4 mg were heated at a rate of 2 °C/min. Initially, the temperature was raised from 25°C to 100°C and kept for 10 min to eradicate moisture.
- MDA-MB 231 cancer cells were grown in 75 cm^3 vented flasks (Porvair) in a humidified **atmosphere incubator** with approximately 5% CO2 at 37°C (Heal Force).
- **Thorlabs M415L3, and M625L3 light-emitting diode (LEDs)** with 415 and 625 nm, respectively, were mounted onto the housing of a Modulight 7710-680 medical laser system were used to illuminate 96 well tissue culture and bacterial stains plates (127.76 × 85.48 mm).
- **Synergy 2 multi-mode microplate reader** (BioTek®) was used to measure cell and bacterial viability for PDT and aPDT.
- Each drug's cellular uptake was determined by measuring absorbance intensities at the B band maxima of the photosensitiser dye using a **Synergy 2 multi-diode microplate reader (BioTek).**
- **An autoclave from China Medical Device (RAU-530D)** was used to sterilise the Muller Hinton and Brain heart infusion broth, agar, PBS, and all the equipment required for cell culturing and bacterial culturing.
- The optical density (OD) of the bacterial culture was evaluated using the **Ledetect 96 microplate reader** Labxim from products.
- The bacterial suspensions were blended using a **Lasec® analogue vortex mixer**.

- The colony-forming units (CFU.mL-1) were determined using **Interscience's Scan® 500 series automatic colony counter**.
- The bacterial pellet was recovered from the suspension using a **Lasec® HemleZ233M-2 centrifuge.**

2.3 Synthesis

2.3.1 Porphyrins

2.3.1.1 Synthesis of 2,2'-(thiophen-2-ylmethylene) bis(1H-pyrrole) dipyrromethene, Scheme 3.1.

The 5-(4-pyridyl)-dipyrromethane was synthesized as reported in the literature [**106**], and 2,2'-(thiophen-2-ylmethylene) bis(1H-pyrrole) was synthesized as follows: 2-thiophenolcarboxaldehyde (4.05 g, 3.60 x10 $^{-2}$ mmol) was dissolved in methanol (MeOH, 180 mL) and the solution was stirred for 1 h, at room temperature under an inert atmosphere. This was followed by the addition of pyrrole (5 mL; 7.22 x10 $^{-2}$ mmol). The mixture was allowed to stir for 24 h. Separately, an aqueous HCl solution was prepared (10 mL HCl in 90 mL water) and was added to the aldehyde mixture and stirred for 24 h. Following this, the mixture was neutralized with triethylamine (TEA) (7 mL). The product was extracted using chloroform. The organic layer was obtained, and the solvent was evaporated to obtain the 2,2'-(thiophen-2-ylmethylene)bis(1H-pyrrole) as a dark brown oily product. **Yield**: 74%. **FTIR** (cm^{-1}): 3084 (-CH), 1556 (C-N), 727 (thio, C-S-C). **^{1}H NMR** (80 MHz, DMSO-d$_6$) δ (ppm) 10.68 - 10.20 (m, 2H), 7.34 -6.97 (m, 2H), 6.87 - 6.66 (m, 2H), 6.65 - 6.34 (m, 2H), 5.84 - 5.61 (m, 1H), 5.60 - 5.53 (m, 2H), 5.44 - 5.26 (m, 1H).

2.3.1.2 Synthesis of (10,20-di(thiophene-2-yl) porphyrin-5,15-diyl) dimorpholine (1), Scheme 3.1.

Complex **1** was synthesized as follows; 2,2'-(thiophen-2-ylmethylene)bis(1H-pyrrole) (2.01 g, 8.88 mmol) was dissolved in MeOH (200 mL) and the solution was stirred at room temperature under an inert atmosphere for 1 h. Morpholine carboxaldehyde (1.02 g. 8.88

mmol) was added, and the solution was stirred for a further 1 h. Aqueous HCl solution (10 mL) was added as above, and the mixture was stirred for 24 h. The mixture was neutralized with TEA (10 mL). The product was extracted in chloroform. The organic layer was obtained, and the solvent was evaporated to obtain the crude product, which was then dissolved in DMF (100 mL) and refluxed for 24 h. The resultant solution was stirred in open air in a beaker for 24 h. The solvent was removed under vacuum, and the product was purified via column chromatography. Chloroform was employed as the eluent to obtain a purple crystalline product. **Yield**: 69%. λ_{max}, nm (log ε) (DMSO): 429 (5.01), 523 (3.72), 563 (3.47), 601 (3.35), 662(3.23). **FTIR** (cm−1): 2919 (Ar, CH), 2850 (-CH), 1397 (C-N), 1589 (Ar, C=N), 1090 (C-O-C), 797 (thio, C-S-C). **^{1}H NMR** (400 MHz, DMSO) δ 9.13 – 8.73 (m, 5H, β-pyrrole), 8.59 (d, J = 16.4 Hz, 1H, β-pyrrole), 8.33 (d, J = 5.1 Hz, 1H, β-pyrrole), 8.19 (s, 2H, thienyl), 8.08 (d, J = 5.0 Hz, 1H, β-pyrrole), 8.03 (dd, J = 13.9, 5.8 Hz, 2H, thienyl), 7.60 (s, 2H, thienyl), 3.31 (s, 16H, morpholiny), -2.83 (s, 2H, N–H). **MALDI-TOF MS** (m/z). Calc: 644.81; found: 642.32 [M-H]$^+$.

2.3.1.3 Synthesis of zinc (II) 4,4'-(10,20-di(thiophen-2-yl) porphyrin-5,15-diyl) dimorpholine (2), Scheme 3.1.

A mixture of zinc acetate dihydrate (48 mg; 1.73 x 10^{-1} mmol, in 10 mL of MeOH) and complex **1** (10 mg; 5.76 x 10^{-2} mmol, in 10 mL of DCM) was stirred for 72 h at room temperature. UV-Vis absorption spectroscopy was used to monitor the completion of the reaction. The four Q bands collapsed into two Q bands for complex **2**. The crude product was washed with water and extracted using DCM. The reaction mixture was dried in the fume hood to obtain the product. **Yield:** 67% (6.7 mg). λ_{max}, nm (log ε) (DMSO): 434 (5.10), 568 (3.77), 635 (3.50). **FTIR** (cm^{-1}): 2919 (Ar, CH), 2850 (-CH), 1412 (C-N), 1548 (Ar, C=N), 1061 (C-O-C), 810 (thio, C-S-C). **^{1}H NMR** (400 MHz, DMSO) δ 9.00 – 8.76 (m, 4H, *ϐ*-pyrrole), 8.61 (s, 1H, *ϐ*-pyrrole), 8.55 (s, 1H, *ϐ*-pyrrole), 8.33 (d, *J* = 5.3 Hz, 1H), 8.13 (d, *J* = 14.8 Hz, 2H, thienyl), 7.93 (d, *J* = 10.3 Hz, 2H, thienyl), 7.79 (s, 1H, *ϐ*-pyrrole), 7.56 (s, 2H, thienyl), 3.31 (s, 16H, morpholiny). **MALDI-TOF** MS (m/z). Cal: 707.75; found: 705.06 [M-H]$^+$.

2.3.1.4 Synthesis of 15-bis(4-(methylthio) phenyl)-10,20-di(pyridin-4-yl) porphyrin (3), Scheme 3.1.

In a 300 mL round bottom flask, 4-(methylthio) benzaldehyde (297.96 µL, 2.24 mmol) and 5-(4-pyridyl)-dipyrromethane (0.5 g, 2.24 mmol) were dissolved in methanol (MeOH, 300 mL). After stirring for 1 h, 10% HCl: water (v/v) aqueous solution was added to the flask, and the reaction mixture was further stirred for 24 h under N_2. After this, TEA (10 mL) was added to neutralize the solution, and the reaction was stirred for 24 h in air. The product was extracted in chloroform. The crude product was then re-dissolved in DMF (100 mL) and refluxed for 24 h. The resultant solution was stirred in open air in a beaker for 24 h. UV-Visible absorption spectroscopy was used to monitor the reaction's completion, after which the solvent was vacuum-dried, and the crude product was purified using silica gel column chromatography. Chloroform was employed as the eluent to obtain a purple crystalline product. **Yield**: 52%. λ_{max}, nm (log ε) (DMSO): 421 (5.37), 514 (4.62), 553 (3.75), 593 (3.60), 635(3.37). **FTIR** (cm $^{-1}$): 3097 (Ar, CH), 2855 (-CH), 1419 (C-N), 1560 (Ar, C=N). **^{1}H NMR** (400 MHz, DMSO-d_6) δ 8.97 (d, *J* = 70.7 Hz, 6H, β-pyrrole), 8.76 (d, *J* = 15.4 Hz, 2H, β-pyrrole), 8.10 (d, *J* = 13.6 Hz, 3H, -*meta*), 7.66 (s, 2H, -*meta*), 7.37 (d, *J* = 8.3 Hz, 4H, -*ortho*), 7.30 (d, *J* = 8.6 Hz, 4H, -*ortho*), 7.18 (s, 1H, -*meta*), 7.05 (s, 1H, -*meta*), 6.93 (s, 1H, -*meta*), 1.19 (s, 6H, *methyl*), -2.95 (s, 1H, N-H). **MALDI-TOF MS** (m/z). Calc: 709.22; found: 709.60 $[M]^+$.

2.3.1.5 Synthesis of zinc (ii) 5,15-bis(4-(methylthio) phenyl)-10,20-di(pyridin-4-yl) porphyrin (4), Scheme 3.1.

A mixture of zinc acetate dihydrate (9.28 mg, 4.2 x 10^{-5} mmol) dissolved in methanol (10 mL) and complex **1** (10 mg, 1.41 x 10^{-5} mmol) dissolved in DCM (10 mL) was stirred at room temperature for 72 h. UV-Vis absorption spectroscopy was used to monitor the reaction where four Q bands of complex **3** collapsed into two Q bands for complex **4**. The crude product was washed with water extracted using DCM and dried in a fume hood to give the final product. **Yield**, 72% (7.2 mg). λ_{max}, nm (log ε) (DMSO): 429 (4.86), 559 (3.83), 602 (3.60). **FTIR** (cm $^{-1}$): 2916-2961 (Ar, CH), 2849 (-CH), 1397 (C-N), 1552 (Ar, C=N). **^{1}H NMR** (400 MHz, $CDCl_3$) δ 8.71 (d, *J* = 18.8 Hz, 3H, β-pyrrole), 8.51 (d, *J* = 11.3 Hz, 5H, β-pyrrole), 8.07 (s, 3H, -*meta*), 7.92 (d, *J* = 28.4 Hz, 4H, -*ortho*), 7.55 (s, 2H, -*meta*), 7.33 (d, *J* = 8.3 Hz, 1H, -*meta*), 7.20

(s, 1H, *-meta*), 6.92 (s, 4H, *-ortho*), 6.63 (s, 1H, *-meta*), 1.37 (s, 6H, *methyl*). **MALDI-TOF MS** (m/z). Cal: 772.27; found: 772.33 [M]$^{+}$.

2.3.2 Synthesis of gold nanoparticles (AuNPs) and gold-coated silica nanoparticles (AuSiO$_2$), Scheme 2.1.

Citrate-capped gold nanoparticles (AuNPs) and gold-coated silica nanoparticles (AuSiO$_2$) were synthesized following the previously described literature procedure [**107,108**]. Following the Turkevich method, solutions of sodium citrate (10 mg. mL^{-1}) and gold (III) chloride trihydrate (0.125 mol. mL$^{-1)}$ were prepared. Subsequently, 420 µL of HAuCl$_4$ was added into 94.6 mL of deionised water, and the mixture was agitated and heated at 80 °C; 5 mL of sodium citrate was rapidly introduced. The mixture was continuously stirred for 20 min at 80 °C (**Scheme 2.1A**); the suspension's colour changed from light yellow to red, showing the successful synthesis of AuNPs. The AuNPs suspension was then gradually cooled to room temperature and stored at 4 °C.

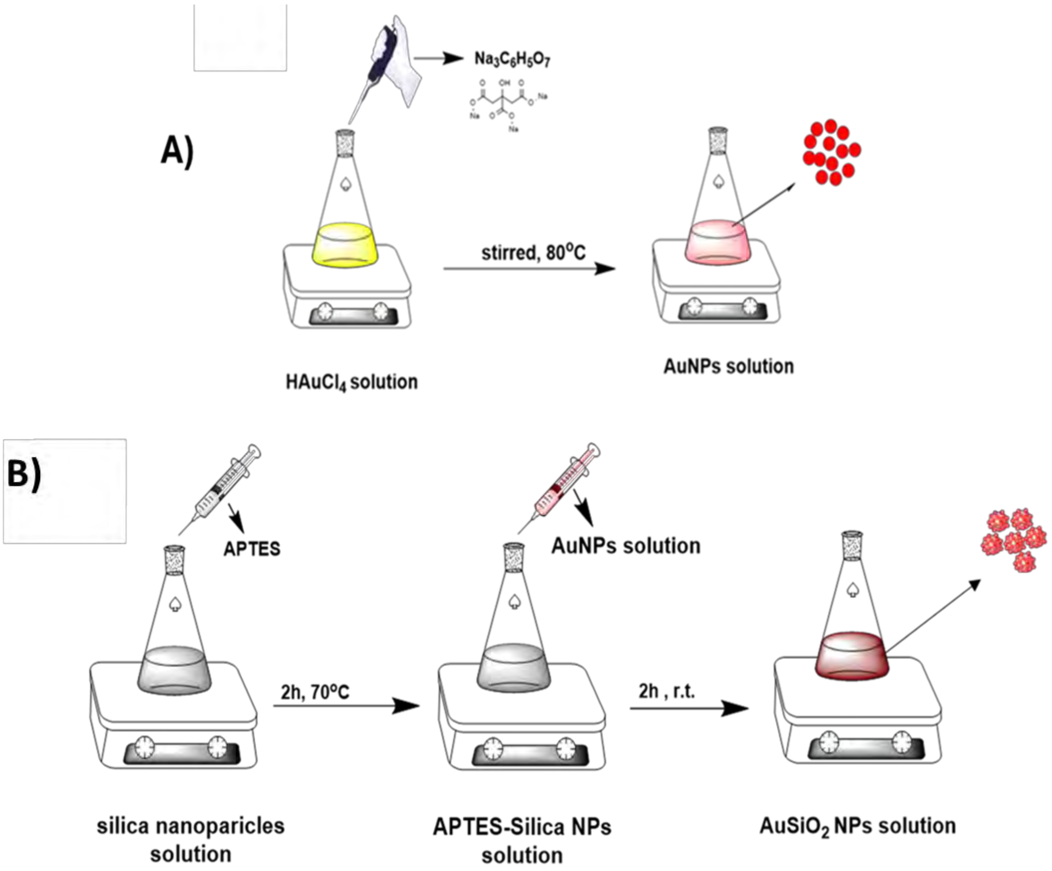

Scheme 2.1: Synthesis of sodium citrate capped **A)** AuNPs and **B)** AuSiO$_2$

Spherical silica nanoparticles were synthesized by using the Stöber process **[90]** as follows (**Scheme 2.1B**): ethanol (40 mL) was mixed with distilled water (5 mL), then ammonium hydroxide (1.5 mL) was added, and the mixture was stirred at 50 °C for 10 min. Then TEOS (1.5 mL) was added, and the solution was stirred for 2 h. To obtain the SiO_2 NPs, the solution was centrifuged 3 times at 6000 rpm for 15 min, then redispersed in absolute ethanol (40 mL). To functionalize with APTES, SiO_2 NPs solution (40 mL) prepared above was added to APTES (12 mM, 0.6 mL) and stirred for 2 h at 70 °C. The solution was left undisturbed overnight. To obtain the functionalized APTES-SiO_2 NPs, the mixture was centrifuged 3 times at 6000 rpm for 15 min, then redispersed in 40 mL of distilled H_2O. APTES in APTES-SiO_2 NPs introduces free amine groups, which serve as adhesion sites for gold nanoparticles in the following stages.

For the synthesis of $AuSiO_2$ (**Scheme 2.1B**) [**108**], citrate-capped AuNPs (30 mg) were added to APTES-SiO_2 NPs (20 mg) in THF (50 mL) and stirred for 5 min gently. The mixture was left undisturbed for 2 h, then washed 3 times with distilled water and centrifuged for 2 min at 6000 rpm and redispersed in 20 mL of distilled H_2O.

2.3.3 Formation of porphyrin complexes with AuNPs and $AuSiO_2$.

Porphyrin complexes **1-4** were conjugated to gold nanoparticles (AuNPs) through self-assembly following a previously reported procedure [**109,110**]. Briefly, each compound (10 mg) was dissolved in 5 mL of chloroform and added to a 10 mL toluene refluxing solution containing KOH. The citrate-capped AuNPs (4 mg in 2 mL toluene) solution was then promptly poured into the reaction vessel and refluxed for an additional 1 h. The reaction mixture was cooled to room temperature and agitated for a further 24 h. The conjugates were centrifuged for 2 min at 6000 rpm, successively washed with ethanol three times, and allowed to dry in the fume hood.

Porphyrin complexes **1-4** were conjugated to gold-coated silica nanoparticles ($AuSiO_2$ NPs), following a previously reported procedure [**108**]. Each complex (10 mg) was dissolved in chloroform (5 mL) and stirred for 10 min, $AuSiO_2$ NPs (0.03 g in 3 mL ethanol) was added, and the reaction mixture was stirred for 24 h at room temperature. The conjugates were centrifuged for 5 min at 6000 rpm, successively washed with ethanol three times to remove any unconjugated porphyrin complexes and allowed to dry in the fume hood.

2.4 Hyperthermia studies

The photothermal effects of AuNPs were evaluated by measuring temperature changes under irradiation. Sample concentrations of 50 µg/mL were exposed to 625 nm light under continuous irradiation. In this experimental system, the 0.3 % (v/v) DMSO: PBS solution was heated up to 37 °C, to imitate an environment in the human body. The human body temperature normally ranges from 36.2 to 37.5 °C [**111**]. To compare the photothermal conversion efficacy, complexes **1** and **2** and their AuNPs nanoconjugates (**1**-AuNPs and **2**-AuNPs) were dissolved in 0.3 % (v/v) DMSO in PBS. PBS alone and 0.3 % (v/v) DMSO: PBS solvent mixture were used as controls and irradiated using a 625 nm LED for 30 min each at 3 min intervals. During the irradiation, a digital thermometer was used to monitor the temperature changes in real time.

2.5 Lipophilicity

Lipophilicity tests were performed in triplicate on each porphyrin complex using the "shake-flask" method [**112**]. The sample solutions were produced by dissolving 0.5 mg of each dye complex in 10 mL of dry $CHCl_3$. The absorbance at the Soret band maxima (A_o) was determined for each 3 mL of the complex's $CHCl_3$. 3 mL of Millipore water was then added to each 3 mL $CHCl_3$ solution, and the mixture was stirred at room temperature for 4 h. The mixture was then centrifuged at 5000 rpm for 10 min to separate the $CHCl_3$ and water phases. The absorbance of the $CHCl_3$ layer (A_f, f-final) was then measured for each complex mixture, with the value for the water phase calculated as the difference between the initial (A_o) and final (A_f) of the dye complex in $CHCl_3$. The partition coefficient values (Log $P_{o/w}$) for the complexes in $CHCl_3$: H_2O were calculated using **Eq. 2.1 [112].**

$$\boldsymbol{P_{octanol} = [1.343 + LogP_{chloroform}]/1.126} \qquad \textbf{2.1}$$

2.6 Cell studies

2.6.1 Tissue culture

Tripple-negative MDA-MB 231 cancer cell lines were grown in DMEM with 4.5 g.L.-1 glucose, L-glutamine, and phenol red. The media was supplemented with 10% (v/v) heat-inactivated Fetal bovine serum (FBS) and 5% penicillin (100 µg. mL^{-1}), streptomycin, and amphotericin B. Cells were cultivated in a T75 cm^2 vented flask (Porvair) in a humidified 5% CO_2 atmosphere at 37°C until 75% confluence was reached. To allow for cell adhesion to the wells, the cells were seeded in 96-well plates at a density of $1x10^3$ cells/well in a supplemented red-phenol DMEM mixture (100 µL). They were then incubated for 24 h in a humidified 5% CO_2 environment. All the *in vitro* cell studies were performed in triplicates.

2.6.2 Cellular drug uptake

The cellular uptake studies of the porphyrin complexes and their conjugates were evaluated using MDA-MB 231 cancer cells. MDA-MB 231 cells were seeded at a density of about $1x10^3$ cells/cm^2 in 96-well plates and allowed to grow for 24 h. The cells were treated with 5, 20, 50, 100, and 200 µg/mL of freshly produced complexes in PBS for 24 h. After treatment, cells were washed three times with PBS (7.4) to remove the sensitizers that were not absorbed by the cells. 25 µL of 1 % Triton X 100 was added in each well followed by incubation for 30 min at 37 °C in order to lyse the cancerous cells open. The absorbance intensities of the complexes were performed using a microplate reader at maximum absorbance (λ_{max}) of the porphyrin complex.

2.6.3 In vitro dark and PDT studies

The complexes and their conjugates were inoculated into 96 well plates at different concentrations: 5, 10, 20, 30, 50, 70, 100, and 200 µg/mL in culture media with 0.3% (v/v) DMSO solution. The control cells were supplemented with medium alone, with the effect of DMSO on the cells investigated by incubating the cells in 0.3 % (v/v) DMSO-DMEM media. The cells were incubated in the dark for 24 h, and thereafter, the in vitro dark cytotoxicity studies were conducted.

For PDT studies, cell samples and drug concentration were prepared similarly to those used in the dark cytotoxicity studies. 24 h after the cell treatment with the porphyrin complexes, the MDA-MB 231 cells were exposed to M625L3 LED (625 nm) for 30 minutes; cells were then re-incubated in media under growth conditions and kept in the dark for 24 h. To evaluate the effect of the treatments on the cells, 10 µL of the resazurin assay reagent was added to each well. The cells were reincubated for 4 h. Dehydrogenase enzymes in live cells can reduce resazurin salt (non-fluorescent) to form a pink, highly fluorescent salt resorufin. The amount of the resorufin in the cell samples after treatments was determined by measuring the fluorescent intensities excitation at 570 nm and emission at 590 nm using the Synergy™ 2 multimode microplate reader to quantify the percentage of cell survival. The cell survival percentage was calculated using **Eq. 2.2**.

$$\boldsymbol{Cell\,Viability}\ (\%) = \left[\frac{\boldsymbol{Treated}}{\boldsymbol{Untreated}}\right] \times \mathbf{100} \qquad \mathbf{2.2}$$

where “treated cells” is the fluorescence intensity of the treatment samples, and “untreated cells” is the fluorescent intensity of the control sample (with no sensitizer). In order to evaluate changes in their morphology, images of the cells post-treatments were captured using the Thermo Scientific™ Invitrogen™ EVOS™ FL Auto 2 Imaging System.

2.7 antimicrobial Photodynamic therapy studies

The aPDT activities of Porphyrin dyes and their conjugates were carried out against Gram (+) methicillin-sensitive *Staphylococcus aureus* (MSSA) (ATCC 259223) and methicillin-resistant *Staphylococcus aureus* (MRSA) (ATCC700699). The MSSA and MRSA bacterial strains were cultured in nutrient broth and Brain Heart Infusion Broth, respectively, then incubated at 37 °C with 5% CO_2 and agitation (*ca.* 200 rpm) in a rotary incubator for 18-24 h until an optical density (OD) of 0.6 at 620 nm was reached. The bacteria pellets were centrifuged for 15 min at 3000 rpm and rinsed three times with PBS, then they were resuspended in PBS to create a culture stock solution of 10^{-2}. The bacterium pellets were further resuspended in PBS and further diluted to create a working solution of 10^{8} CFU/mL^{-1}. The optimal working concentration of each micro-organism was determined using all the porphyrin complexes and their conjugates at 1, 5, 20, 50, and 100 µg/mL in 0.3% (v/v) DMSO:PBS.

The micro-organisms and photosensitizers solutions (100 µL) were prepared in 96 well plates and were incubated with shaking (200 rpm) for 30 min in the dark at 37 ^{O}C to allow drug uptake. Photoirradiation was carried out using M415L4 Thorlabs LEDs for 30 min, and the other set of 96 well plates were kept in the dark for 30 min for *in vitro* dark cytotoxicity studies. Using a modified method as reported in literature [**113**], 100 µL of freshly prepared broth was then added, and the plates were incubated for 18 h at 37 ^{o}C. To assess the impact of the treatments on the bacterial cells, 10 µL of resazurin assay reagent was administered to each well. The cells were re-incubated for 3 h. Fluorescence measurements (λex = 560 nm, λem = 590 nm) were done using a Synergy 2 multi-mode microplate reader (BioTek®) and in triplicates. The bacterial cell survival percentage was calculated using **Eq. 2.2**. Data on bacterial cell survival were provided as means ± standard deviation (SD).

Results and Discussion

Publications

The results discussed in this thesis (chapters **4,5** and **6)** have been published in the following peer-reviewed journals.

V. Nobatana, J. Oyim, N. Nwahara, E. Prinsloo, and T. Nyokong, The potential of photodynamic therapy combined with hyperthermia using porphyrin-nanomaterial hybrids against the triple-negative breast cancer cell line. Polyhedron, 267 (2025) 117341. https://doi.org/10.1016/j.poly.2024.117341.

V. Nobatana, J. Oyim, N. Nwahara, A. Sindelo, and T. Nyokong, The photodynamic anti-cancer and anti-bacterial behaviour of meso-substituted trans-A2B2 porphyrin conjugated silica-gold nanoparticles. Inorganica Chimica. Acta, (2025) 122584. https://doi.org/10.1016/j.ica.2025.122584.

CHAPTER THREE

Synthesis and Characterization of Porphyrins Dyes

This chapter details the synthesis and characterization of the porphyrin dyes.

3.1 Synthesis and characterizations of porphyrins and their Zinc(II) complexes

The free-base porphyrin ligands (complex **1** and **3**) and their zinc derivatives (complex **2** and **4**) were synthesized using the synthetic method in **Scheme 3.1 [114].**

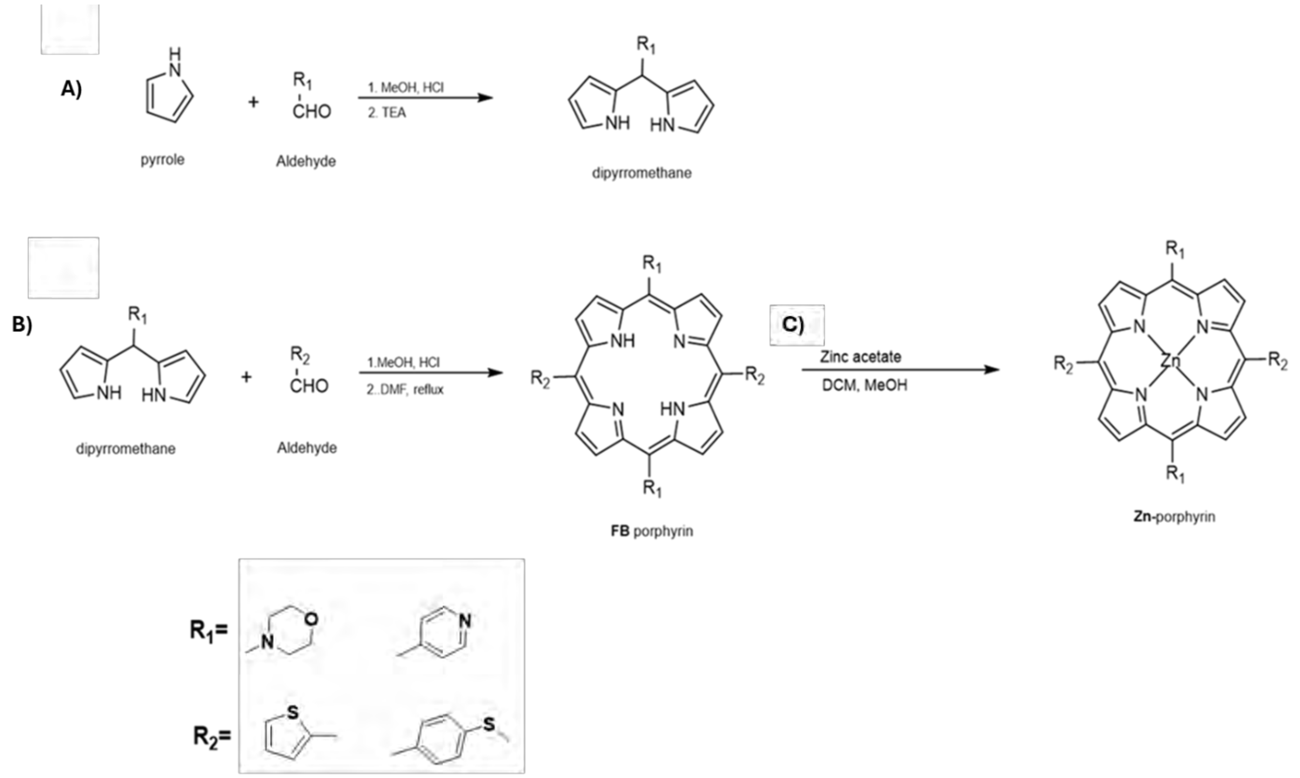

Scheme 3.1: Synthesis of **A**) dipyrromethane, **B**) porphyrin complexes **1**-**4** and their corresponding **C**) Zinc (**II**) complexes. **FB**= free base.

All porphyrin complexes were studied using UV-Visible spectroscopy, Fourier-transform infrared spectroscopy (FT-IR), MALTI-TOF mass spectra (MS), and ^{1}H NMR spectroscopy. MALTI-TOF mass spectra revealed the molecular ion peak was at m/z = 642.32 for complex **1,** which is $[M-H]^+$ of what was expected and at m/z = 705.06 for complex **2** that is $[M-H]^+$ of what was expected. The molecular peak ion was observed at m/z = 709.60 for complex **3**, that is, [M]+ of what was expected, and at m/z = 773.33 for complex **4**, that is, $[M]^+$ of what was expected. ^{1}H NMR spectrum for complex **1** was integrated to 32H, including 2H (NH) from the core of porphyrin, complex **2** to 30H, and complex **3** to 31H, where 1H (NH) from the core of porphyrin was not observed on the NMR spectrum due to strong shielding **[115]** and complex **4** to 30H.

The UV-Vis spectra of all porphyrin complexes were obtained in DMSO. The spectra of the free base porphyrin complexes (**1** and **3**) displayed Soret bands as well as four less intense Q-bands (**Fig**. **3.1A**). For complex **1** Soret band was absorbed at 429 nm, while complex **3** was at 421 nm (see **Table 3.1**). Complex **1** was red-shifted in comparison to complex **3** because it contains the electron-rich element oxygen, resulting in a redshift of the absorption band [**116**], as seen in **Fig. 3.1A** and **Table 3.1.**

Table 3.1 Optical parameters (UV-Vis) for all the porphyrin complexes and conjugates in DMSO and nanoparticles alone in water (H_2O).

Complexes	**λ_{Abs} (nm) Soret band**	**λ_{Abs} (nm) Q-bands**
1	429	523, 564, 601, 662
2	434	566, 633
3	421	514, 553, 593, 635
4	429	559, 601
AuNPs	518[a]	–
1-AuNPs	429	523, 562, 602, 662
2-AuNPs	434	570, 614
3-AuNPs	420	516, 554, 587, 646
4-AuNPs	428	558, 601
$AuSiO_2$	532[a]	–
1-$AuSiO_2$	431	512, 565, 614, 660
2-$AuSiO_2$	434	563, 635
3-$AuSiO_2$	419	515, 553, 593, 635
4-$AuSiO_2$	427	559, 601

[a] Surface plasmon resonance band

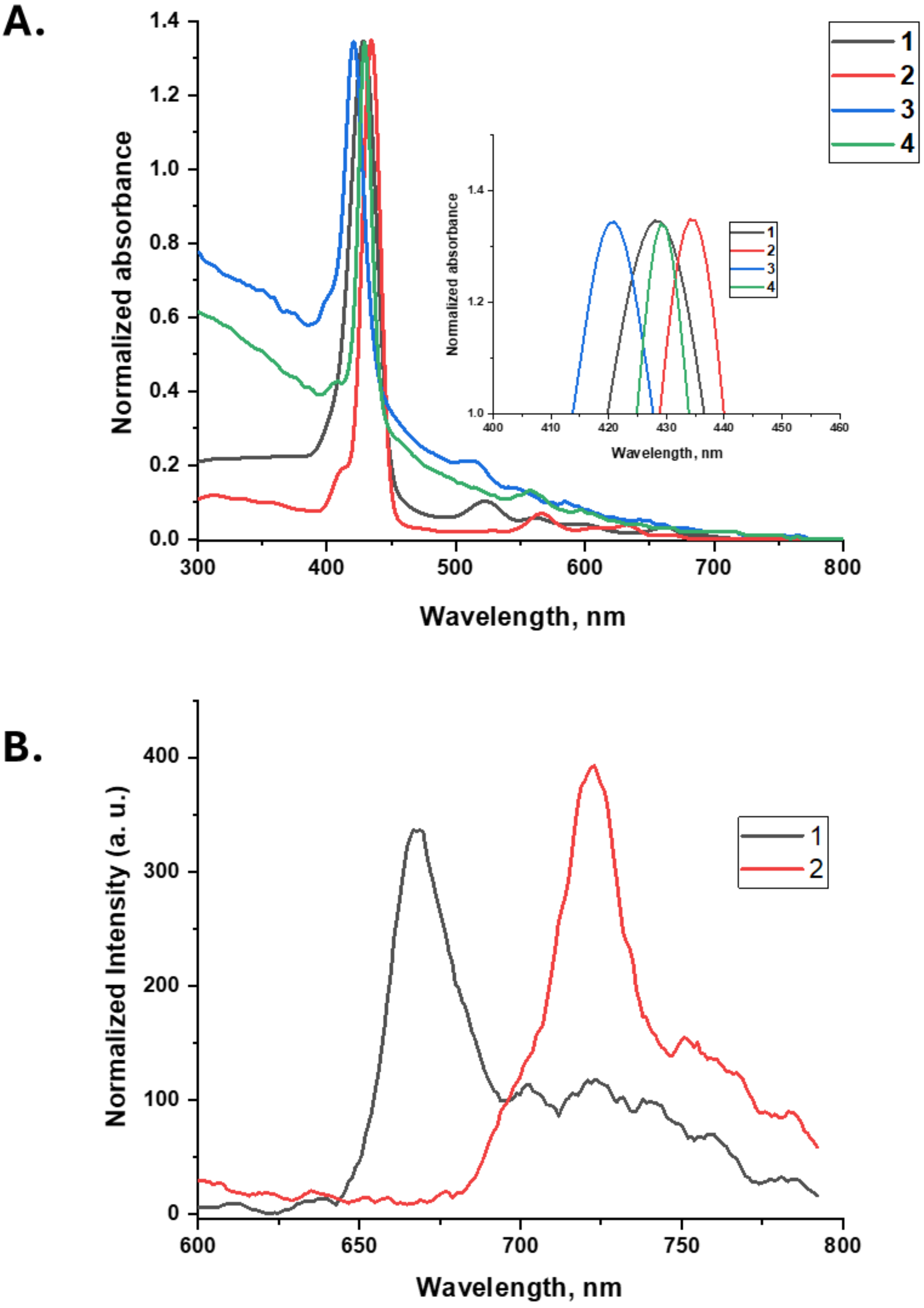

Fig. 3.1 UV-Vis spectra of porphyrin complexes (**A**) **1, 2,3,** and **4** in DMSO and (**B**) Fluorescence emission spectrum of **1** and **2**.

The four Q-bands in complexes **1** and **3** merged into two Q bands when the metalated complexes **2** and **4** formed (**Fig. 3.1 A**), with the Soret band red shifting to 434 nm and 429 nm, respectively. The introduction of heavy metals such as zinc may cause disturbance and electron delocalisation within the porphyrin macrocycle [**46,97,117**], resulting in redshifts in absorption spectra. **Fig**. **3.1B** shows fluorescence emission spectra for **1** and **2** as an example, with fluorescence emission bands observed at 667 nm and 712 nm, respectively. Fluorescence was very weak for all the porphyrin complexes used in this work.

3.2 Formation of conjugates

All porphyrin complexes were linked to AuNPs and AuSiO$_2$ through the ligand exchange method. This was through sulfur-gold [**74,118**] or nitrogen-gold affinities to afford the dye-AuNP or dye-AuSiO$_2$ nano assemblies (**Scheme 3.2**).

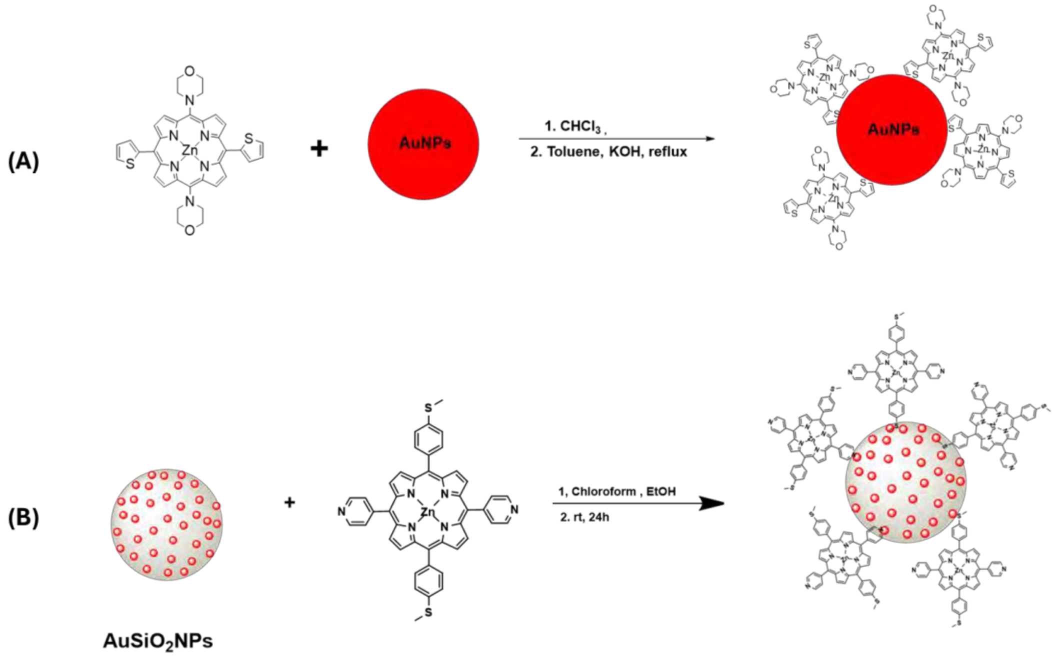

Scheme 3.2: Synthesis of **A**) **2**-AuNPs and **B**) **4**-AuSiO$_2$NPs as representative nanoconjugates.

The characterization of synthesized AuNPs and AuSiO$_2$ NPs and conjugates were achieved using various characterization techniques. Ultraviolet-visible spectroscopy (UV-Vis), dynamic light scattering (DLS), fourier transform infrared (FT-IR), X-ray diffraction (XRD) and scanning electron microscopy (SEM) were used. The conjugation through self-assembly (Au-S) was proven using X-ray photoelectron spectroscopy (XPS). The thermal stability of the conjugates and the NPs were analysed using thermal gravimetric analysis (TGA), and thermal decomposition profiles of the porphyrin, NPs, and conjugate were compared.

3.2.1 UV-Visible absorption spectroscopy

The UV–vis spectra of the gold NPs (AuNPs) and gold-coated silica NPs (AuSiO$_2$) were obtained in water **Fig. 3.2A.** It was observed that AuNPs had a peak at 518 nm, which red-shifted to 532 nm for AuSiO$_2$. All the UV-Vis absorption spectra of the nanoconjugates were obtained using DMSO (**Fig. 3.2B and C**). The Soret bands for **1**-AuNPs, **2**-AuNPs, **3**-AuNPs and **4**-AuNPs were observed at 429 nm, 434 nm, 420 nm, and 428 nm, respectively. The Soret band of the **1**-AuSiO$_2$, **2**-AuSiO$_2$, **3**-AuSiO$_2$, and **4**-AuSiO$_2$ nanoconjugates were observed at 431 nm, 434 nm, 419 nm, and 427 nm, respectively. There were no significant changes observed in the Soret band absorption spectra of the complexes upon conjugation to the NPs (**Fig. 3.2B and C)**. However, there was a red-shifting on the nanoparticles, this was ascribed to silica in the gold-coated silica nanoparticles (AuSiO$_2$) **Fig. 3.2A**.

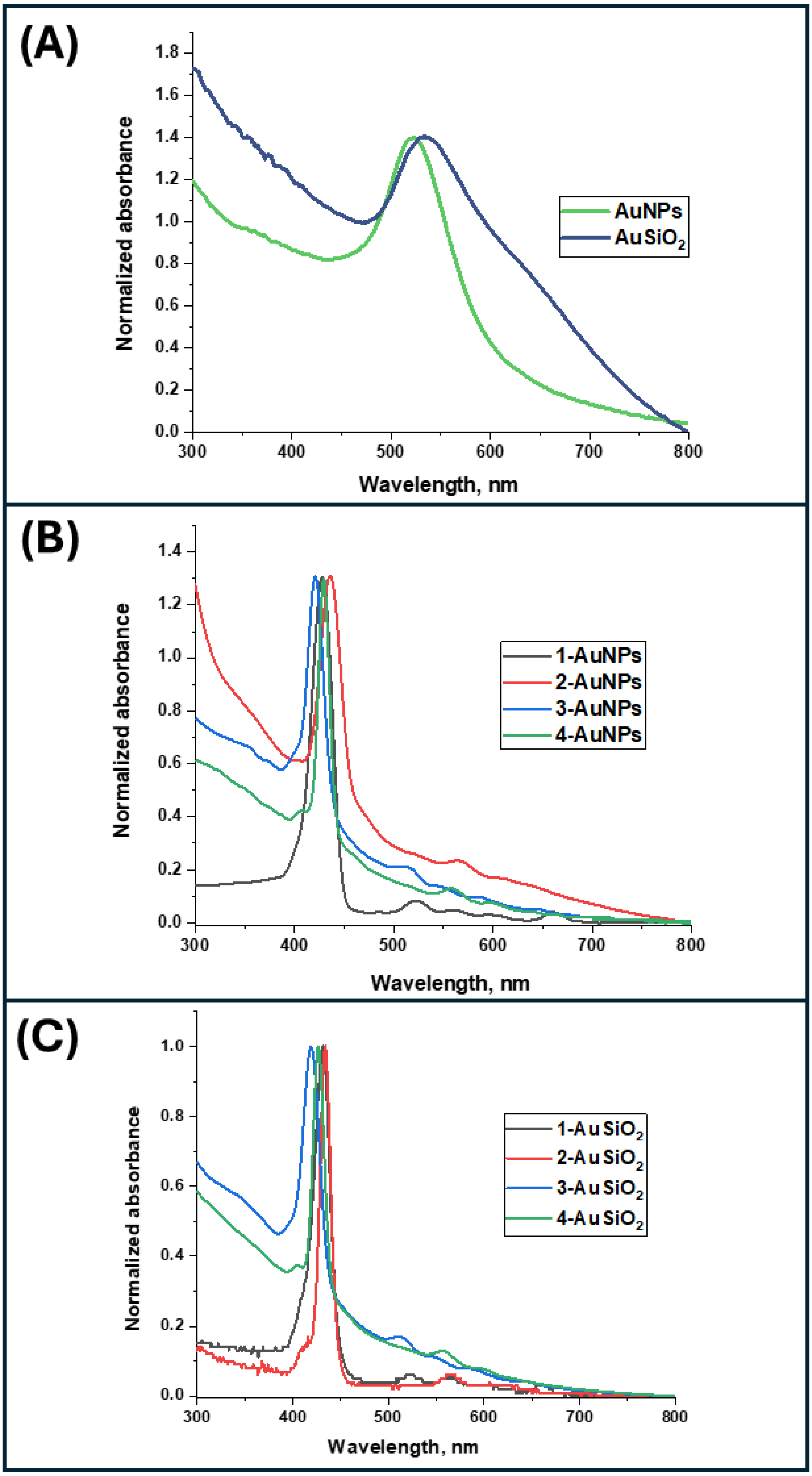

Fig. 3.2. UV-Vis spectra (**A**) AuNPs and AuSiO$_2$ in H_2O, (**B**) AuNPs conjugates, and (**C**) AuSiO$_2$ conjugates in DMSO.

3.2.2 Dynamic light scattering (DLS) and Zeta potential measurements

Dynamic light scattering (DLS) was used to determine the average particle distribution. The average diameter of AuNPs and $AuSiO_2$ NPs obtained was 11.7 and 4.27 nm, respectively, (**Fig. 3.3A** and **B), Table 3.2**). Upon the conjugation of the porphyrins to the nanoparticles (AuNPs and $AuSiO_2$), there was an increase in size, and this is due to interactions between the porphyrins and nanoparticles. The increased size of the nanoconjugates, as compared to nanoparticles alone, indicates the formation of macromolecular assemblies of AuNPs/$AuSiO_2$ and porphyrin complexes.

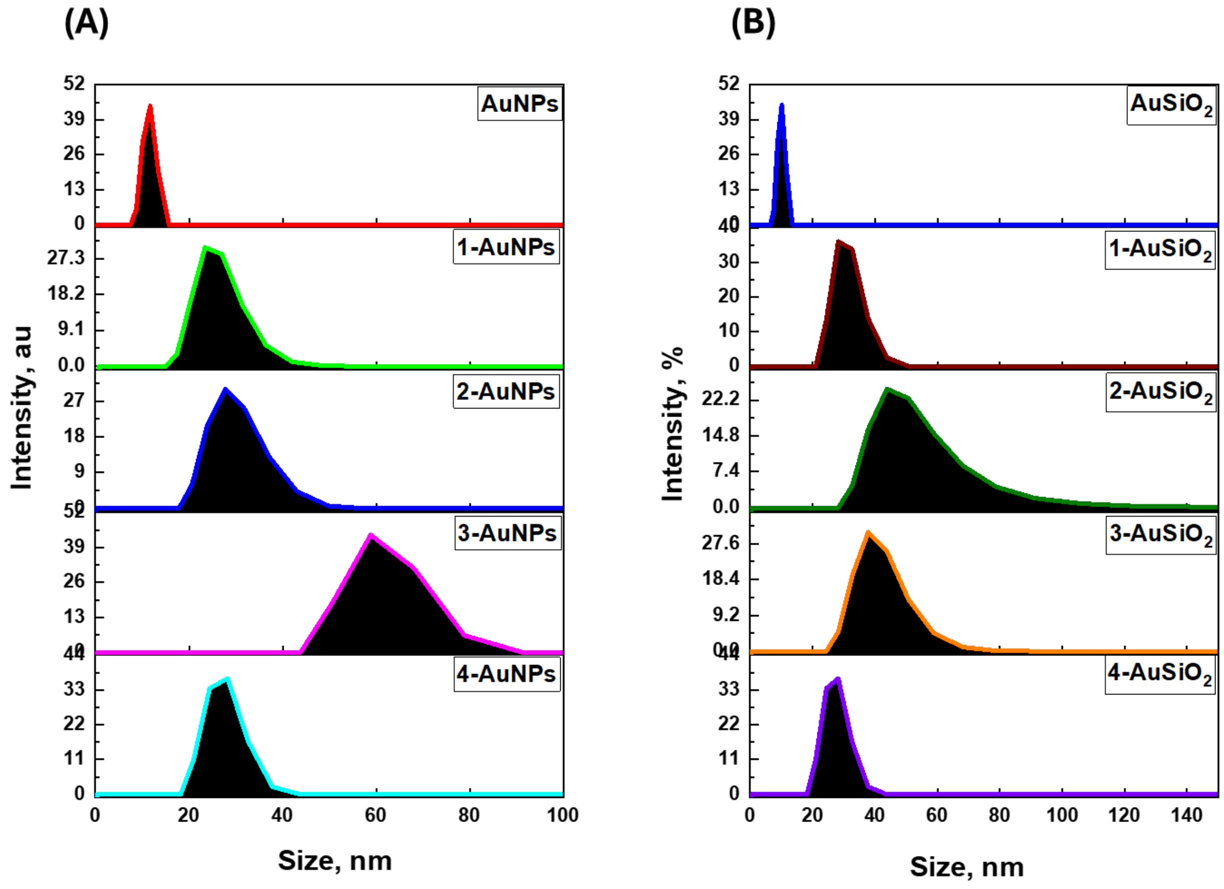

Fig. 3.3. Dynamic light scattering (DLS) distribution curve for (**A**) AuNPs and its conjugates, (**B**) $AuSiO_2$ NPs and their conjugates.

Table 3.2 Nanoparticle, and nanoconjugates sizes and Zeta potential values.

Complex / conjugate	**XRD size (nm)**	**DLS size (nm)**	**PDI**	**Zeta potential (ζ)**
AuNPs	11.84	11.7	0.78	-22.1
1-AuNPs	16.39	23.4	0.31	-6.10
2-AuNPs	24.83	27.7	0.57	-5.64
3-AuNPs	64.81	61.46	0.49	-7.84
4-AuNPs	57.08	27.1	0.38	-11.42
$AuSiO_2$	4.27	9.85	0.50	-11.62
1-$AuSiO_2$	35.06	30.98	0.43	-6.8
2-$AuSiO_2$	89.43	52.37	0.47	-10.91
3-$AuSiO_2$	11.04	40.97	0.40	-11.80
4-$AuSiO_2$	28.52	32.82	0.38	-11.71

Size, polydispersity index (PDI), and zeta potential (ζ) are some of the parameters of nanoparticles and nanoconjugates that influence their physicochemical and biological characteristics [**119**]. The PDI value determines the particle size distribution of the samples. When the sample PDI value is greater than 0.7, it suggests that the particle size distribution is broad [**120**]. It was observed that AuNPs and $AuSiO_2$ resulted in PDI values of 0.78, and 0.50, respectively, **Table 3.2.** All the nanoconjugates had a PDI value less than 0.7 (see **Table 3.2**), these PDI values indicate narrow particle dispersion. Zeta potential measures the stability of a colloidal dispersion; low values suggest that attractive forces lead to aggregation, and high positive or negative values indicate stability and the dispersion capacity to withstand aggregation [**121**]. The zeta potentials of AuNPs obtained were (-22.1 mV), and $AuSiO_2$ (-11.62 mV). A slight decrease was observed following the conjugation of nanoparticles to the porphyrin complexes, implying relatively less stability of the conjugates, with complex **2**-AuNPs having the lowest ζ value (see **Table 3.2**).

3.2.3 X-ray photoelectron spectroscopy (XPS)

The interaction between nanoparticles (AuNPs) and porphyrin complexes was assessed using XPS analysis. The survey XPS spectra of the porphyrin showed peaks for the expected components within their expected binding energy ranges. As an example, spectra for complexes **2**, **2**-AuNPs, and AuNPs are shown in **Fig. 3.4A**, Complex **2** has Zn loss (100 eV), S (162 eV), C (283 eV), N (398 eV) and O (530 eV) peaks, while AuNPs had Au (60, 366, and 371 eV) peaks and C (283 eV) and O (530 eV) peaks associated with the sodium citrate capping agents [**122,123**]. The **2**-AuNPs nanoconjugate spectrum showed peaks associated with complex **2** as anticipated and additional Au peaks stemming from the AuNPs. Using complex **2** as an example, the high-resolution XPS analysis was also utilised to assess the interactions between the AuNPs and porphyrin complexes in more detail (**Fig. 3.4B** and **C**). Deconvoluting S 2p peak for complex **2** produced two subpeaks at 161.7 and 162.8 eV, ascribed to the C-S. Similar patterns were seen in the deconvolution of the **2**-AuNPs nanoconjugate S 2p peak (**Fig. 3.4C**). The presence of C-S confirms the bond.

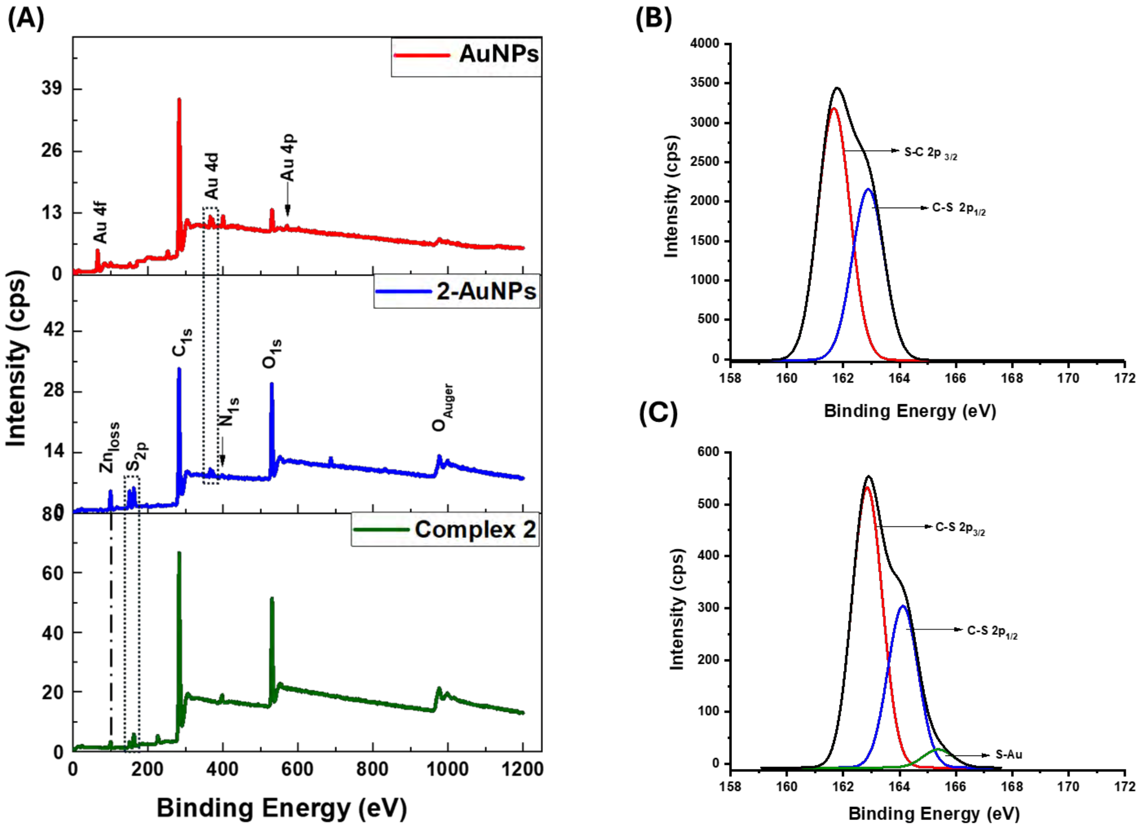

Fig. 3.4 The XPS (**A**) wide scan for AuNPs, complex **2** and **2**-AuNPs. S 2p high-resolution XPS spectra of (**B**) complex **2** and (**C**) **2**-AuNPs.

3.2.4 X-ray Diffraction (XRD)

The X-ray diffraction (XRD) characterisation technique was utilised for phase identification of synthesised NPs and nanoconjugates, with some of the complexes (**1** and **3**) shown in **Fig. 3.5,** as examples. The 111, 200, 220, 311, and 222 planes of the face-centred-cubic structures of metallic gold, which corresponds to 2θ = 38.13, 44.27, 64.54, 77.64, and 81.77°, were visible in the XRD diffraction patterns for the nanoconjugates. Sharp peaks were observed for complexes **1** between 2θ = 10° and 35°, which are sometimes observed for samples of crystalline porphyrin [**122**]. Crystalline peaks that are related to complex **1** were present in diffractograms of **1**-AuNPs along with crystalline peaks of the AuNPs. Complex **3** showed two amorphous peaks between 2θ = 17° and 33°. However, for **1**-$AuSiO_2$ and complex **3** conjugates (**3**-$AuSiO_2$ and **3**-AuNPs), only the peaks due to AuNPs and $AuSiO_2$ are observed. Some metal porphyrins show weak and relatively broad XRD patterns due to their amorphous nature [**124**].

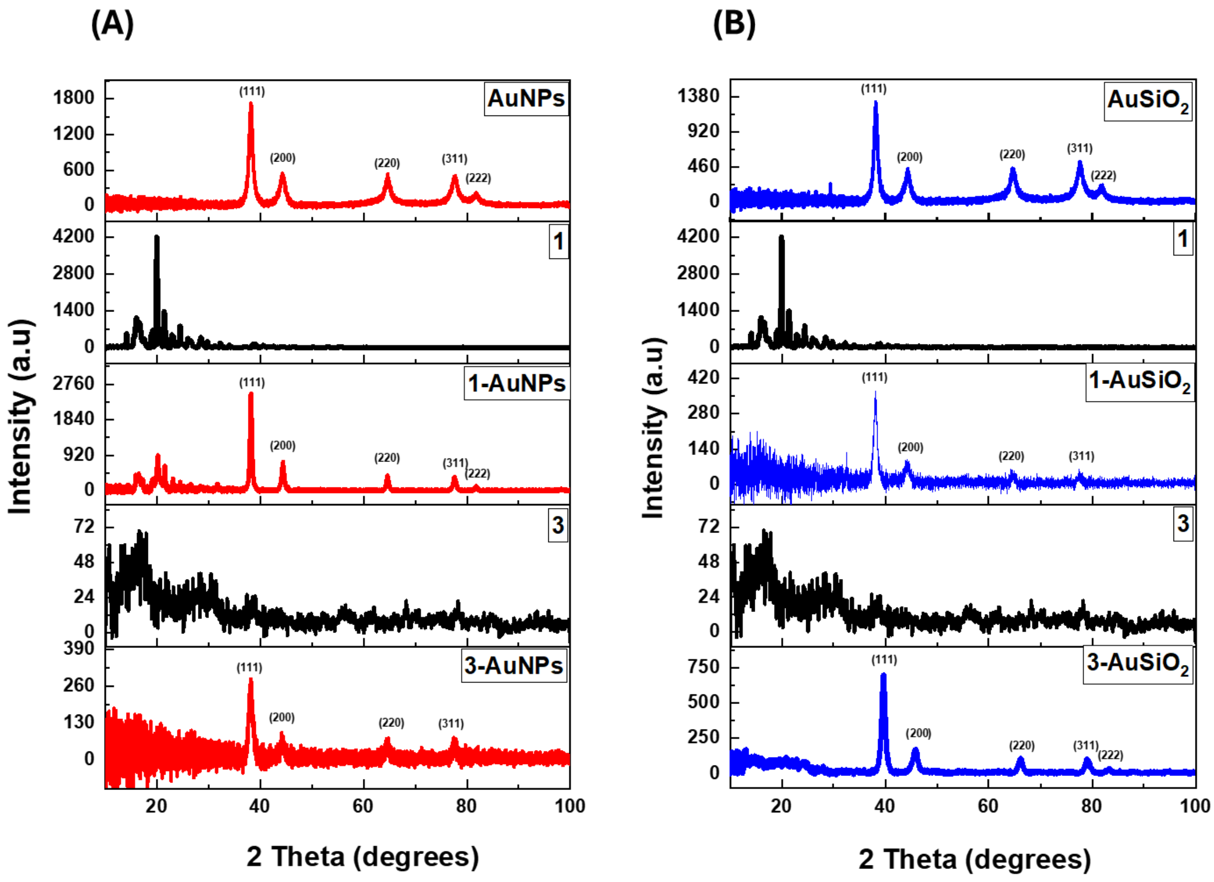

Fig. 3.5 X-ray diffraction (XRD) diffractograms of the NPs (AuNPs and $AuSiO_2$), porphyrin (**1** and **3**), and conjugates.

The average crystalline size (D) was determined using the Debye-Scherrer formula **Eq. 3.1.**

$$\boldsymbol{d} = \frac{\boldsymbol{k\lambda}}{\boldsymbol{\beta \cos \theta}} \qquad \mathbf{3.1}$$

Where k is Scherrer constant (0.9), λ is the wavelength of the X-ray source (0.15405 nm), β is the FWHM (full width at half maximum, radians), and θ is the peak position corresponding to FWHM (radians) **[125]**. The FWHM was estimated using Origin 8 professional on a Gaussian plot using the 4 characteristic peaks. The D values obtained were 11.84, 16.39, 24.83, 64.81, 57.08, 4.27, 35.06, 89.43, 11.04, and 28.52 nm for AuNPs, **1**-AuNPs, **2**-AuNPs, **3**-AuNPs, **4**-AuNPs, $AuSiO_2$, **1**- $AuSiO_2$, **2**- $AuSiO_2$, **3**- $AuSiO_2$ and **4**- $AuSiO_2$ respectively (**Table 3.2**). The DLS particle size estimations were slightly higher for most conjugates as compared to the ones from XRD, this can be attributed to the interference of the dispersant during the analysis **[126] Table 3.2.**

3.2.5 Fourier-transform infrared spectroscopy (FT-IR)

FTIR was utilized to identify the functional groups present, **Fig. 3.6A**. All porphyrin complexes **1**, **2**, **3**, and **4** had –C–H aromatic peaks between 2916 and 3150 cm^{-1}, followed by the aromatic C=N at 1552-1560 cm^{-1} and C–N peak at 1397-1489 cm^{-1}**, Fig. 3.6A**. The stretch peaks from 3332-3457 cm^{-1} are observed in complexes **1** and **3**, not in **2** and **4**, due to the presence of N-H groups in the former.

The $AuSiO_2$ NPs and its conjugates functional groups were also studied using FT-IR spectroscopy (**Fig. 3.6A**). Three distinct bands were observed on the $AuSiO_2$ NPs, the siloxane band (Si-O-Si) at 1089 cm^{-1}, the primary amine from the capping ligand (APTES) at 791 cm^{-1}, and silanol group from (APTES) at 948 cm^{-1} which were also observed on the nanoconjugates. The gold-coated silica nanoparticles also had an O-H band at 3330 cm^{-1} from H_2O, **Fig. 3.6B**. The conjugates (**1**-$AuSiO_2$, **2**-$AuSiO_2$, **3**-$AuSiO_2$ and **4**-$AuSiO_2$) (**Fig. 3.6A**) also showed distinct band peaks between 2700-3150 cm^{-1} (-C-H); these peaks were also observed in the porphyrin complexes (**1**, **2**, **3**, and **4**) alone but not on the nanoparticles. The C=O peaks between 1630-1766 cm^{-1}, stemming from the citrate group were also visible.

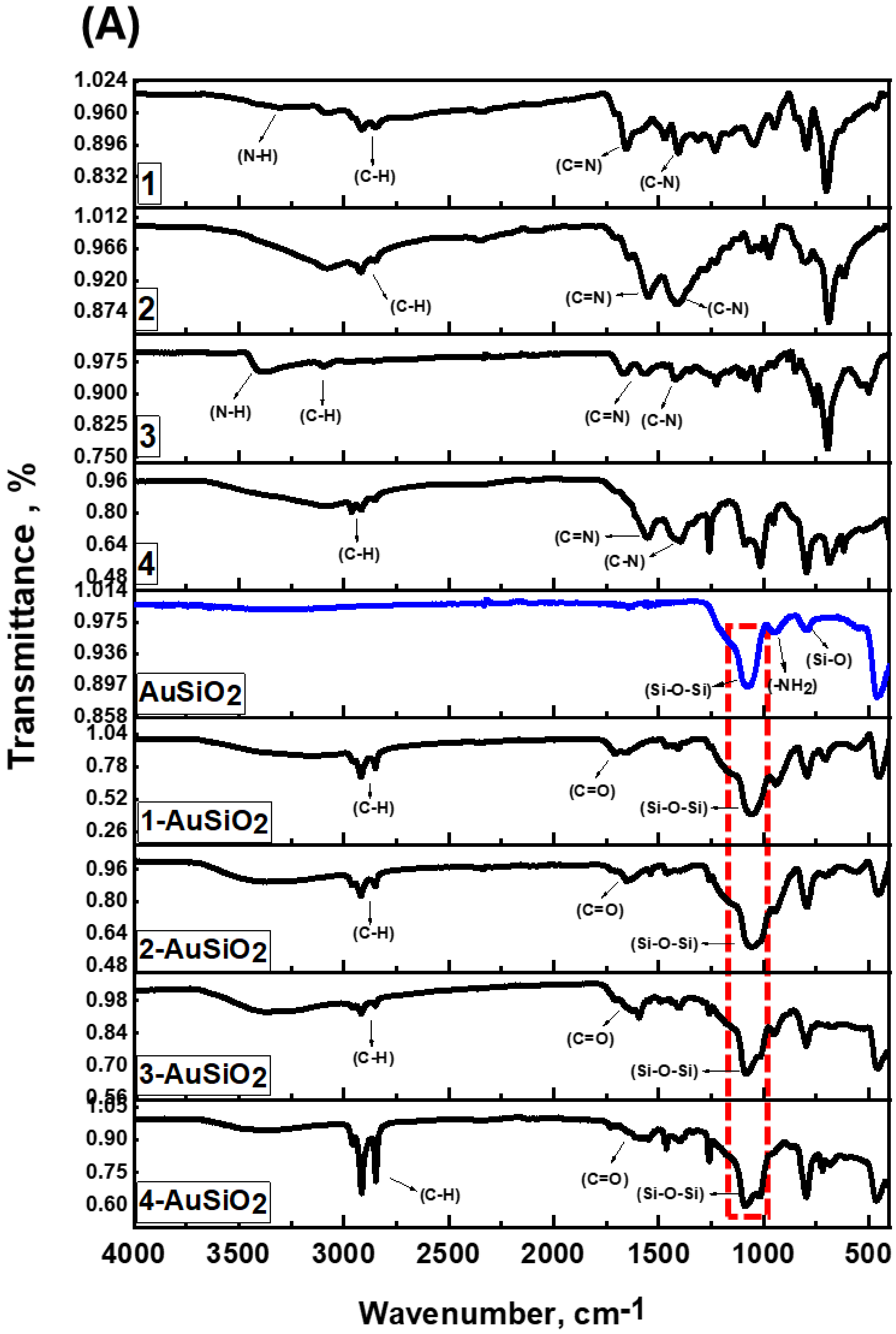
(A)
Transmittance , %
Wavenumber, cm-1
4000
3500
3000
2500
2000
1500
1000
500
1
1.024
0.960
0.896
0.832
(N-H)
(C-H)
(C=N)
(C-N)
2
1.012
0.966
0.920
0.874
(C-H)
(C=N)
(C-N)
3
0.975
0.900
0.825
0.750
(N-H)
(C-H)
(C=N)
(C-N)
4
0.96
0.80
0.64
0.48
(C-H)
(C=N)
(C-N)
AuSiO2
1.014
0.975
0.936
0.897
0.858
(Si-O-Si)
(-NH2)
(Si-O)
1-AuSiO2
1.04
0.78
0.52
0.26
(C-H)
(C=O)
(Si-O-Si)
2-AuSiO2
0.96
0.80
0.64
0.48
(C-H)
(C=O)
(Si-O-Si)
3-AuSiO2
0.98
0.84
0.70
0.56
(C-H)
(C=O)
(Si-O-Si)
4-AuSiO2
1.05
0.90
0.75
0.60
(C-H)
(C=O)
(Si-O-Si)

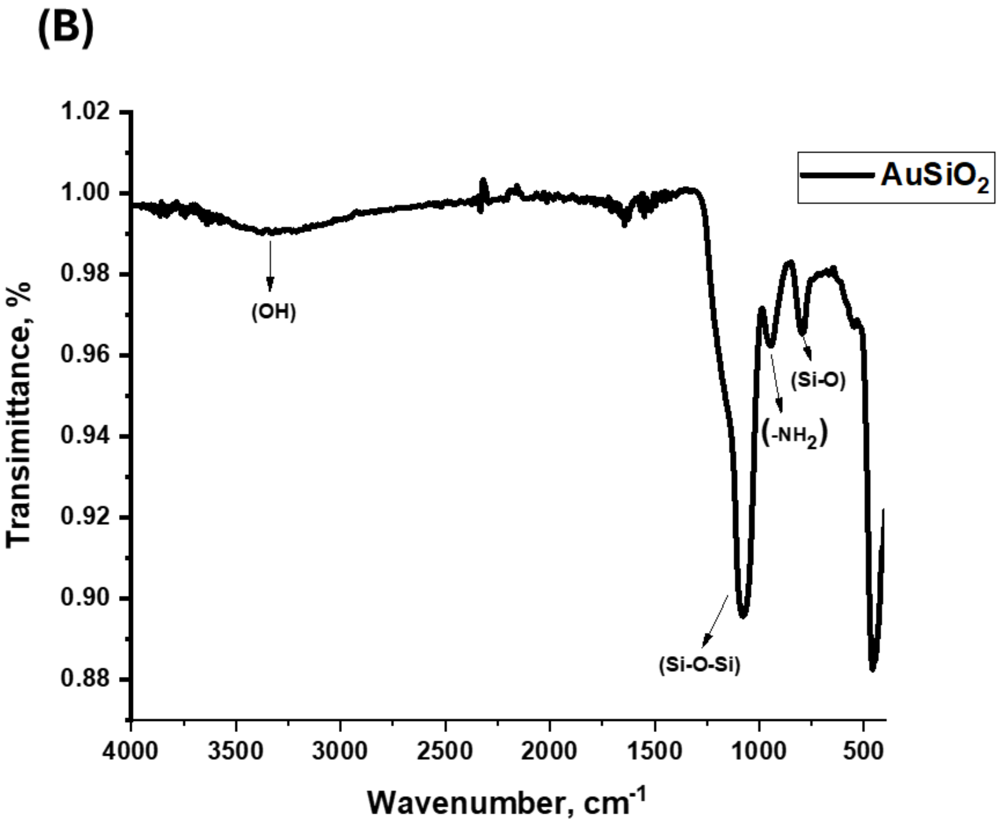

Fig. 3.6 FT-IR spectra analysis for the porphyrin complexes **(A) 1**, **2**, **3**, and **4**, $AuSiO_2$ conjugates and **(B)** $AuSiO_2$.

3.2.6 Thermogravimetric analysis (TGA)

The thermal stabilities of the nanoparticles (AuNPs and $AuSiO_2$) and the nanoconjugates were studied using thermogravimetric analysis. The thermograms were conducted in the temperature range of 50–850 °C in a nitrogen atmosphere. Shown in **Fig. 3.7A**, AuNPs showed a weight loss of 80% between 160–368 °C. The $AuSiO_2$ nanoparticles showed excellent thermal stability, and no significant weight loss was observed (**Fig. 3.7C**). Silica nanoparticles have been reported to be thermally stable from room temperature to 1500 °C **[127,128].** The stability of the porphyrin complexes (**1**, **2**, **3**, and **4**) improved upon the conjugation with the AuNPs, and **2**-AuNPs revealed thermal stability of 58 % at 850 °C and complex **2** decomposed between the temperature of 160–240 °C and 450–625 °C with a total weight loss of 90 % (**Fig. 3.7A** and **B**). It was also found that the $AuSiO_2$ conjugates showed reduced thermal stability when compared to $AuSiO_2$ nanoparticles (**Fig. 3.7C**); this could be due to the porphyrin alone.

This is shown as an example in **Fig. 3.7D** complex **3**, having a total weight loss of 84.3% at 850 °C, and **3**-$AuSiO_2$ had a total weight loss of 56 % at 850 °C. Overall, the $AuSiO_2$ conjugates had better thermal stability as compared to AuNPs conjugates (**Fig. 3.7A** and **C**).

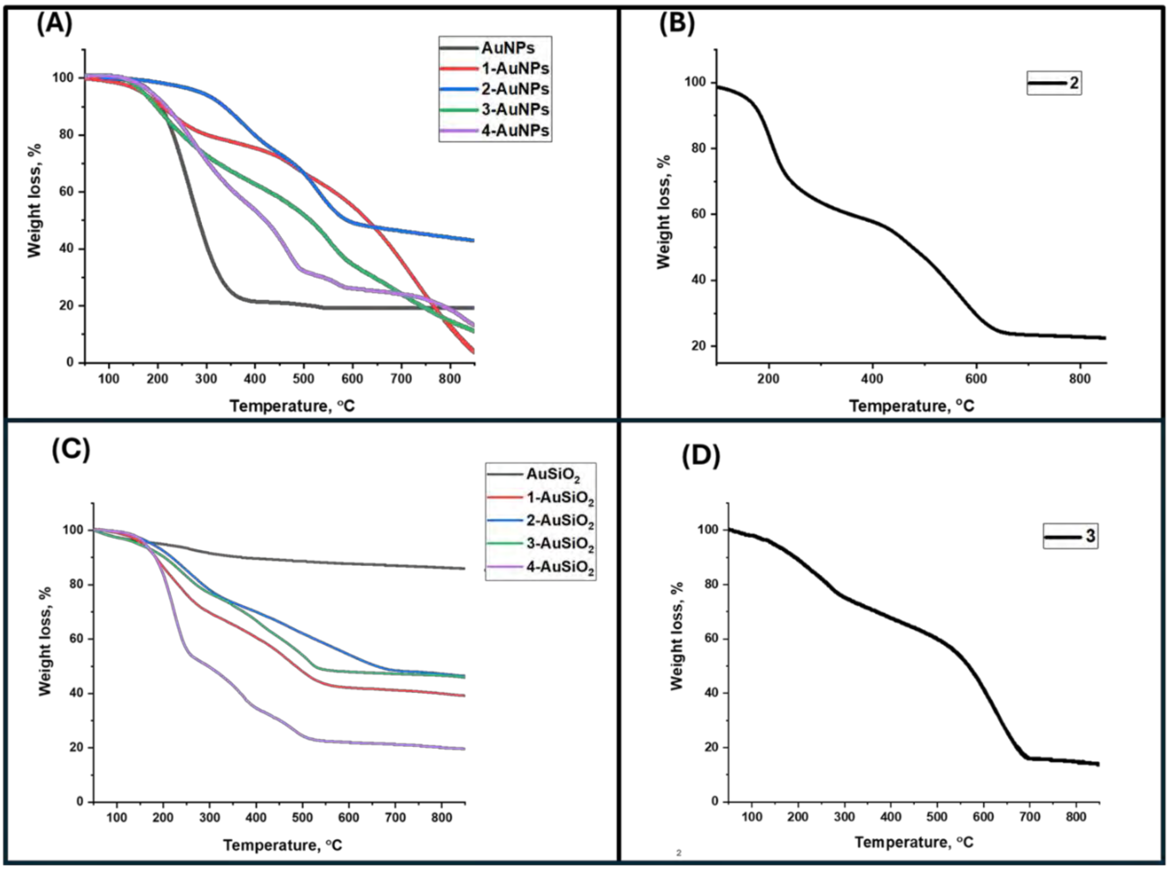

Fig. 3.7 TGA curves of the nanoparticles, conjugates (**A** and **C**) and complex **1** and **3** as examples

3.2.7 Scanning electron microscopy (SEM).

SEM images were obtained to study the surface morphology of the silica-gold nanoparticles and their nano-conjugates. **Fig. 3.8a** shows the morphology of the $AuSiO_2$ nanoparticles, where we noticed the spherical nature of the nanoparticles. **Fig. 3.8b** and **3.8c** show the morphology of **3**-$AuSiO_2$ and **4**-$AuSiO_2$ complexes, where it was observed that the porphyrin aggregated. Overall, all the conjugates showed identical morphological characteristics when SEM was utilized.

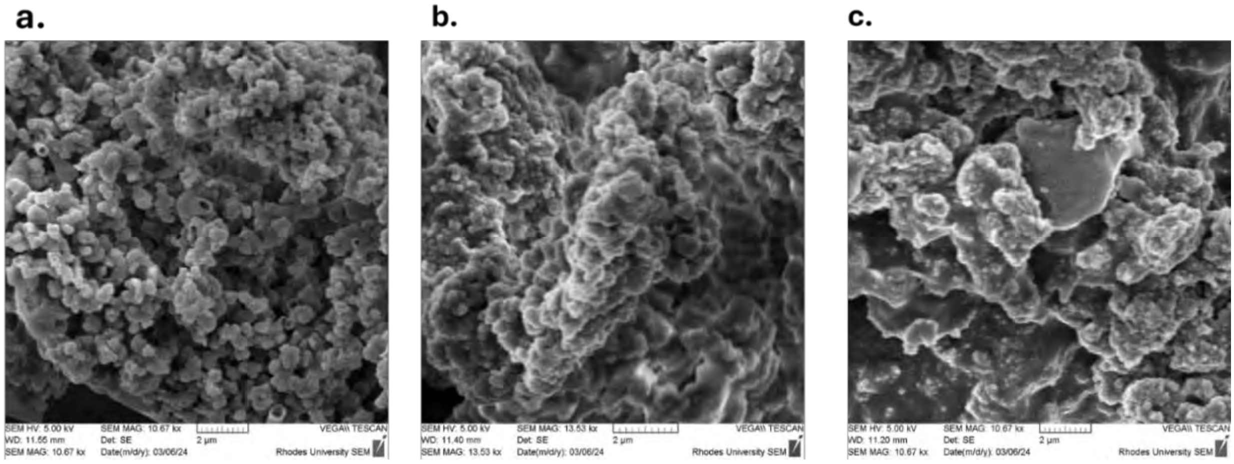

Fig. 3.8. SEM images of $AuSiO_2$ (a), **3**-$AuSiO_2$ (b), and **4**-$AuSiO_2$ (c) used examples.

3.3 The photothermal effects of AuNPs

Fig. 3.9. shows the temperature increases of complexes **1** and **2** with their nanoconjugates (**1**-AuNPs and **2-**AuNPs) at 50 µg/mL concentration irradiated with 625 nm LED for 30 min, with a starting temperature of 37 °C. A temperature increases of 4.89, 0.89, 0.19, 3.51, 3.98, 0.8, and 0.37 °C at 1800 sec, were observed for AuNPs, **1**, **2**, **1**- AuNPs, **2**-AuNPs, PBS, and 0.3 % DMSO: PBS, respectively. A detectable temperature stabilization was observed after 9 min of radiation for the AuNPs; this confirms the photothermal activity of AuNPs. There were less than 1 °C temperature increases for both the PBS and 0.3 % PBS: DMSO. A temperature increase of 5.5 °C when AuNPs in water solution was irradiated with a 635 nm LED light for 30 min has been reported by Yue and co-workers [**129**]. They also observed that the heat produced by the AuNPs is affected by the nanoparticle's size, concentration and the media used. For real biological applications, it would be preferable to use larger AuNP concentrations and smaller particle sizes as much as feasible within the selectable range [**129**].

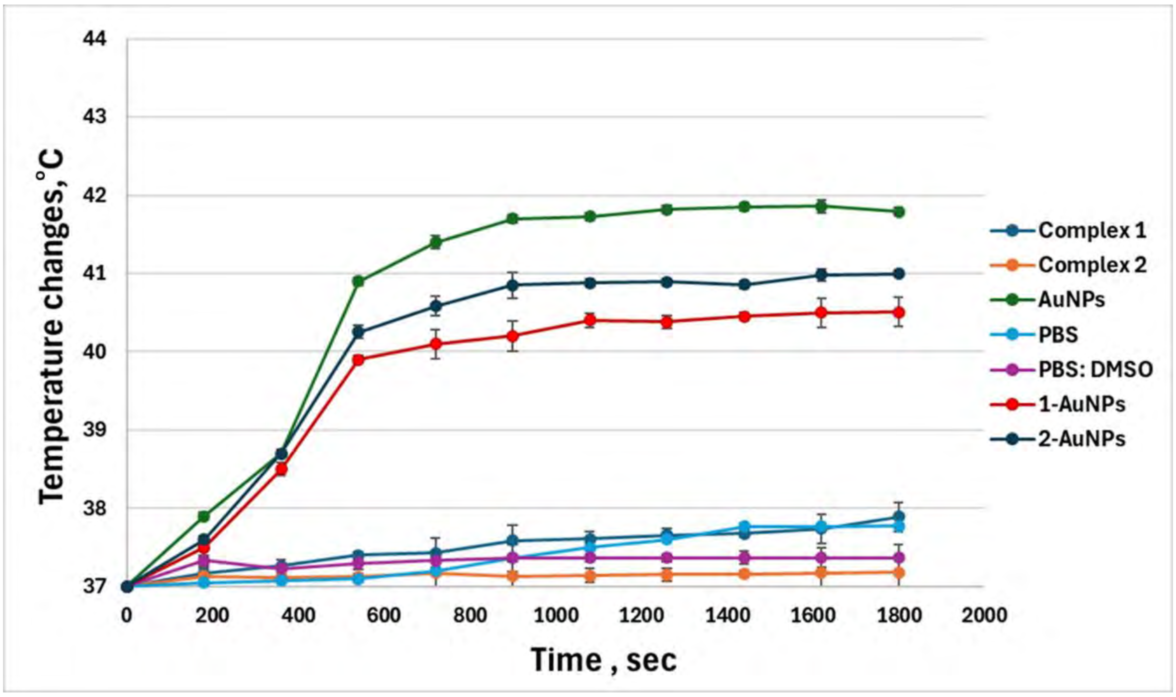

Fig. 3.9 Temperature increases as a function of time for the complexes/conjugates (50 µg/mL) in 0.3% (v/v) DMSO: PBS.

3.4 Photophysical and photochemical parameters

All photophysical and photochemical characteristics were investigated in DMSO, and the results are shown in **Table 3.3**.

Table 3.3 Photophysical parameters in DMSO

Complexes/ Conjugates	**ϕ_F**	**ϕ_Δ**	**τ_T (μs)**
1	<0.01	0.46	15
1-AuNPs	<0.01	0.57	89
1-AuSiO$_2$	0.02	0.38	83
2	<0.01	0.48	76
2-AuNPs	<0.01	0.65	115
2-AuSiO$_2$	0.01	0.59	98
3	<0.01	0.20	98
3-AuNPs	0.03	0.39	31
3-AuSiO$_2$	<0.01	0.35	17
4	<0.01	0.49	54
4-AuNPs	0.01	0.58	52
4-AuSiO$_2$	<0.01	0.51	23

3.4.1 Singlet oxygen quantum yields (ϕ_Δ).

Singlet oxygen production is one of the primary parameters that indicate the efficiency of the photosensitiser because it is responsible for cancer cells and bacterial cell obliteration through fatal oxidative stress [**130**]. Singlet oxygen is produced by an energy transfer between the excited triplet state of the photosensitiser and the ground state in molecular oxygen [**131**]. In this study, the ϕ_Δ value was obtained by monitoring the chemical degradation of DMA, a singlet oxygen quencher, and ZnTPP (ϕ_Δ^{std} =0.53), a standard in DMSO [**59**]. DMA deterioration was seen (**Fig. 3.10**), and ϕ_Δ values were determined using a literature-reported equation [**132**]. The Soret and Q bands of the porphyrin complexes remained stable (**Fig. 3.10**), indicating their photostability. The free base complexes, **1** (ϕ_Δ= 0.46) and **3** (ϕ_Δ= 0.20), as expected, showed a lower ϕ_Δ as compared to the Zn metaled porphyrin complexes, **Table 3.3**. The AuNPs conjugates, **1**-AuNPs (ϕ_Δ= 0.57), **2**-AuNPs (ϕ_Δ= 0.65), **3**-AuNPs (ϕ_Δ =0.39), and **4**-AuNPs (ϕ_Δ= 0.58) resulted in the highest ϕ_Δ values when compared to their respective porphyrin complexes, this is due to the presence of external heavy gold atom which enhances the intersystem crossing to the triplet state. It was also observed that the AuSiO$_2$ conjugates

1-AuSiO2 (ϕ_Δ =0.38), **2**- AuSiO2 (ϕ_Δ =0.59), **3**- AuSiO2 (ϕ_Δ =0.35), and **4**- AuSiO2 (ϕ_Δ =0.51) had higher ϕ_Δ values compared to their porphyrin complexes alone. The AuNPs conjugates had higher ϕ_Δ than AuSiO2 conjugates, this could be due to the presence of silica in the AuSiO2 NPs quenching the production of singlet in the AuSiO2 nanoparticles resulting in slightly lower ϕ_Δ values.

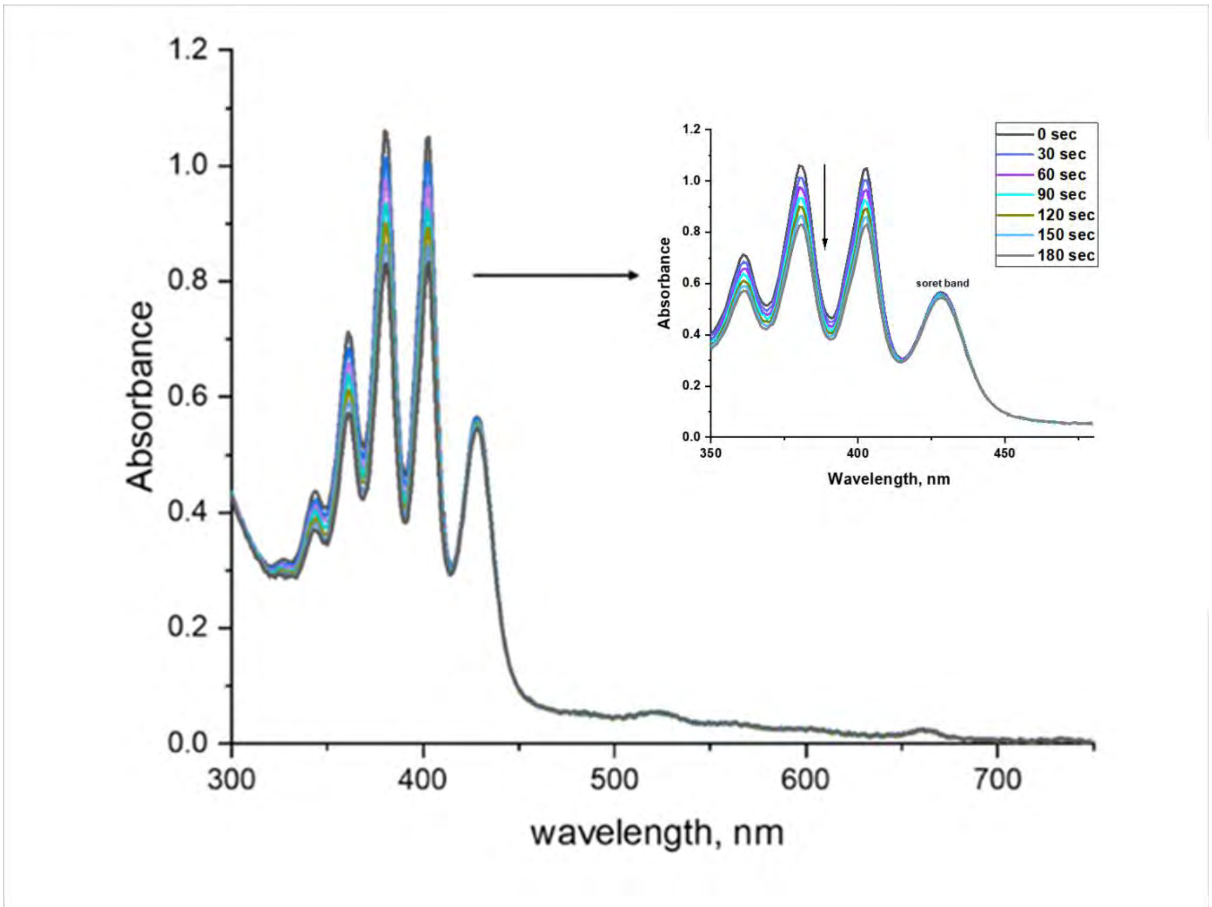

Fig. 3.10 Degradation of 9,10-dimethyl anthracene (DMA) in the presence of complex **1** (solvent, DMSO).

3.4.2 Fluorescence quantum yields (ϕ_F) and triplet lifetimes (τ_T).

The ratio of photons emitted through fluorescence to absorbed is displayed by fluorescence quantum yield (ϕ_F) values. They show the efficiency of photon emission restoring an excited molecule to its electrical ground state. Numerous factors affect this process, including electrical structure, steric contacts, and conformational interactions [**53**]. Fluorescence quantum yields (ϕ_F) were obtained using ZnTPP ($\phi_{F\,std}$=0.030) as a standard [**133**] in DMSO for porphyrins complexes, following the comparative methods reported in the literature [**52**]. The ϕ_F values for most of the complexes were relatively low, with values < 0.01, **Table 3.3**.

The triplet decay curves (**Fig. 3.11**) were fitted exponentially on ORIGIN® 8 Professional software to obtain the triplet lifetimes. The triplet lifetime (τ_T) for **1**-AuNPs (89 µs) was longer than for complex **1** (15 µs) alone, the same applies for complex **2** (76 µs) and its **2**-AuNPs (115 µs) conjugate. Interestingly, the τ_T values from complex **3** (98 µs) and **4** (54 µs) decreased upon AuNPs conjugation (**3**-AuNPs and **4**-AuNPs). The AuNPs conjugates had higher triplet lifetimes as compared to AuSiO$_2$ conjugates, hence the improved singlet oxygen quantum yield of porphyrins in the presence of AuNPs. The triplet decay curve (for complex **4** and **2**-AuNPs as an example) is shown in **Fig. 3.11**.

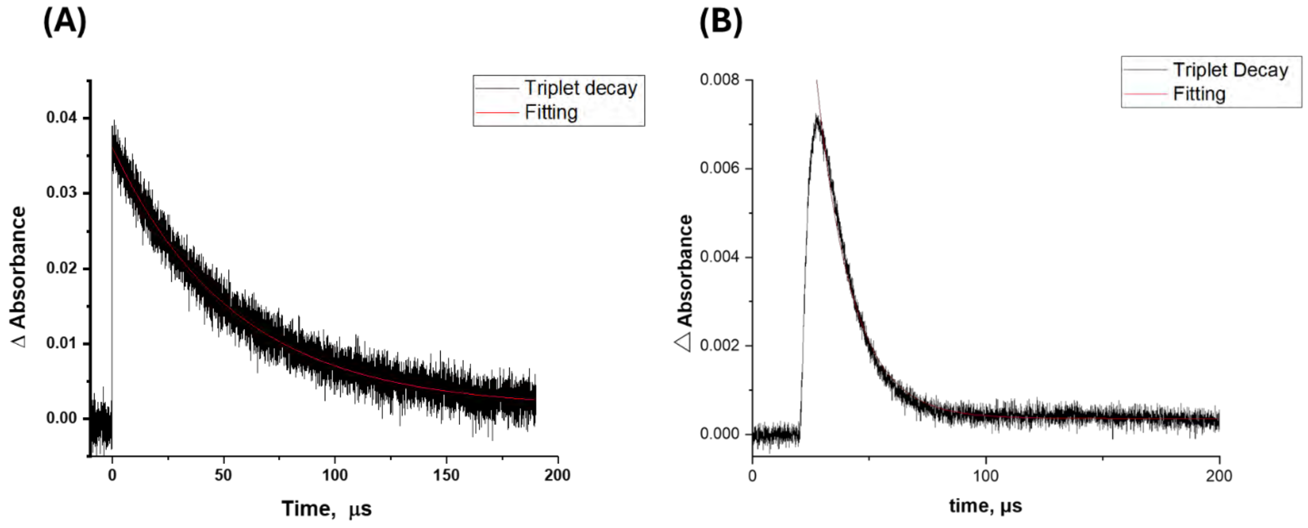

Fig. 3.11 The triplet decay curve for Complex **4** (**A**) and complex **2**-AuNPs (**B**) In DMSO, as examples.

3.5 Summary of the chapter

Asymmetric porphyrins were synthesized as potential photosensitisers for aPDT and PDT. AuNPs and AuSiO$_2$ were also synthesized and conjugated to the porphyrin complexes. The conjugates and porphyrin complexes were fully characterized by different characterizing techniques. The conjugation of porphyrin-AuNPs and porphyrin-AuSiO$_2$ was done through Au-

S/N bond. The photophysiochemical properties of compounds were studied, and it was observed that the ϕ_F of all porphyrins were low. However, upon conjugation of porphyrin complexes to the nanoparticles (AuNPs and $AuSiO_2$) there was an increase in ϕ_Δ.

CHAPTER FOUR

IN VITRO PHOTODYNAMIC THERAPY ACTIVITY OF PORPHYRIN DYES.

This chapter discusses the *in vitro* dark cytotoxicity and PDT activities toward Tripple-negative breast cancer cells (MDA-MB-231) using the as-prepared porphyrin complexes, nanoparticles and their corresponding conjugates.

4.1 Introduction

This study focuses on A_2B_2 porphyrin dyes (complexes **1-4**), the impact of ligand modifications and nanoparticle conjugation (AuNPs and $AuSiO_2$) on their PDT activities. The porphyrin dyes in this study are expected to have advantageous PDT activities because of their high ϕ_Δ values. In *vitro* studies were carried out against triple-negative cancer cells, MDA-MB-231.

4.1.1 *In Vitro* dark cytotoxicity.

The cells were treated with porphyrin complexes and their nanoconjugates (AuNPs and $AuSiO_2$) at 5-200 µg/mL concentration range and incubated in the dark at 37 °C for 24 h. The dark cytotoxicity was evaluated by calculating the percentage of live cells relative to untreated cell samples using the resazurin cell viability kit. At all concentrations, the cell survival percentage of all porphyrin complexes and their conjugates was above 75%, which is insignificant and innocuous against the MDAMB-231 cells, **Fig. 4.1.** The IC_{50} values of all the complexes were >25 in the dark, **Table 4.1**. A photosensitizer dye suitable for PDT application when not irradiated (dark) should have either no or very little cytocidal activities [**4,134,135**]. One of the unfavourable aspects of photosensitizer dyes used in PDT is dark cytotoxicity, which causes cytocidal actions that are non-selective towards both malignant and healthy cells [**4,134,135**].

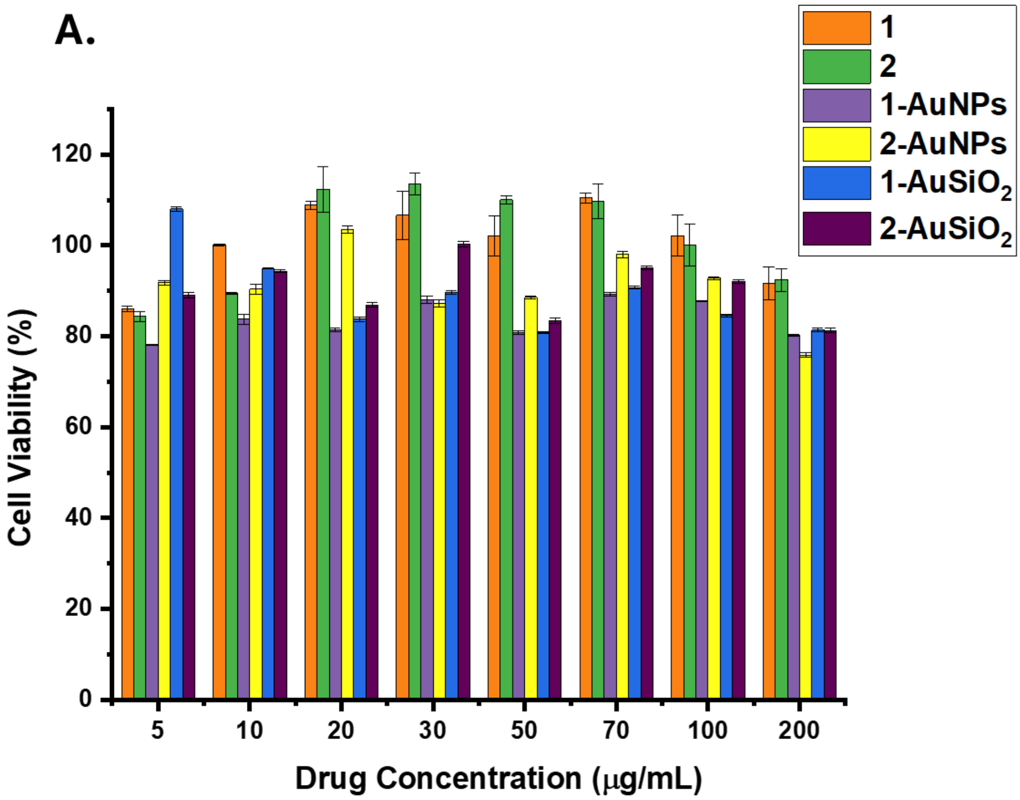
A.
Cell Viability (%)
0
20
40
60
80
100
120
5
10
20
30
50
70
100
200
Drug Concentration (μg/mL)
1
2
1-AuNPs
2-AuNPs
1-AuSiO$_2$
2-AuSiO$_2$

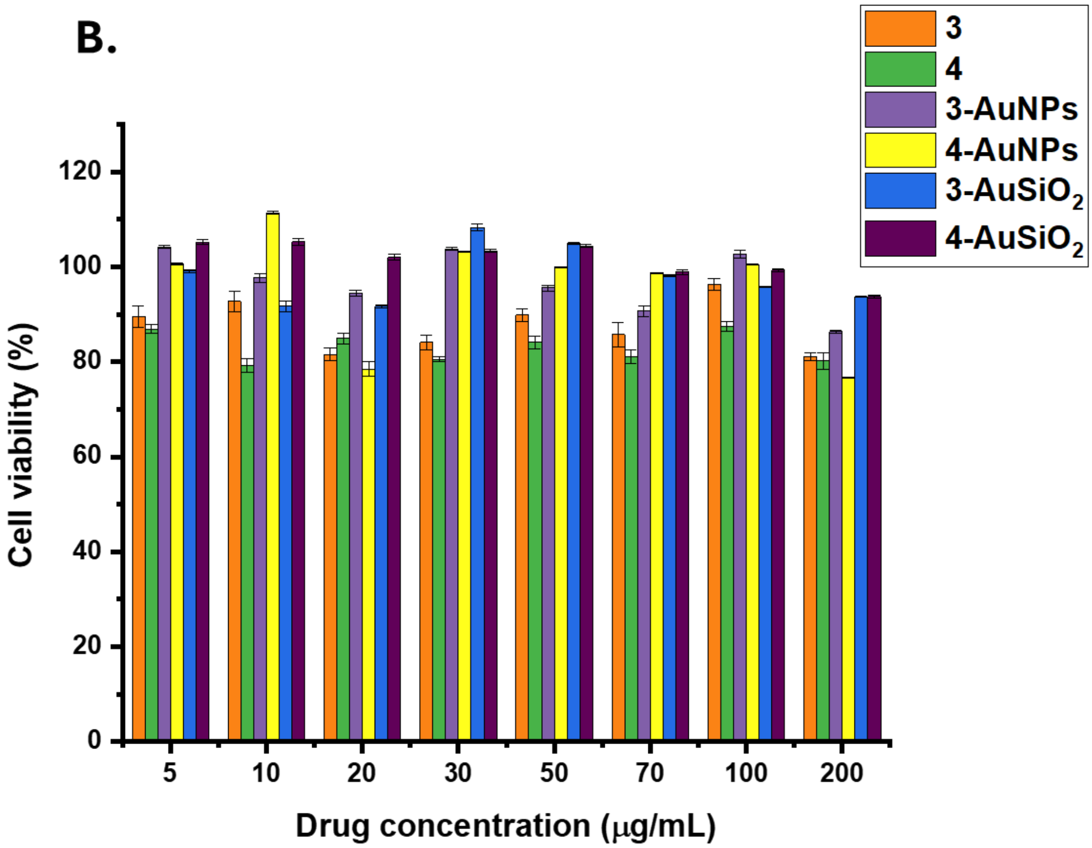
B.
Cell viability (%)
0
20
40
60
80
100
120
5
10
20
30
50
70
100
200
Drug concentration (μg/mL)
3
4
3-AuNPs
4-AuNPs
3-AuSiO$_2$
4-AuSiO$_2$

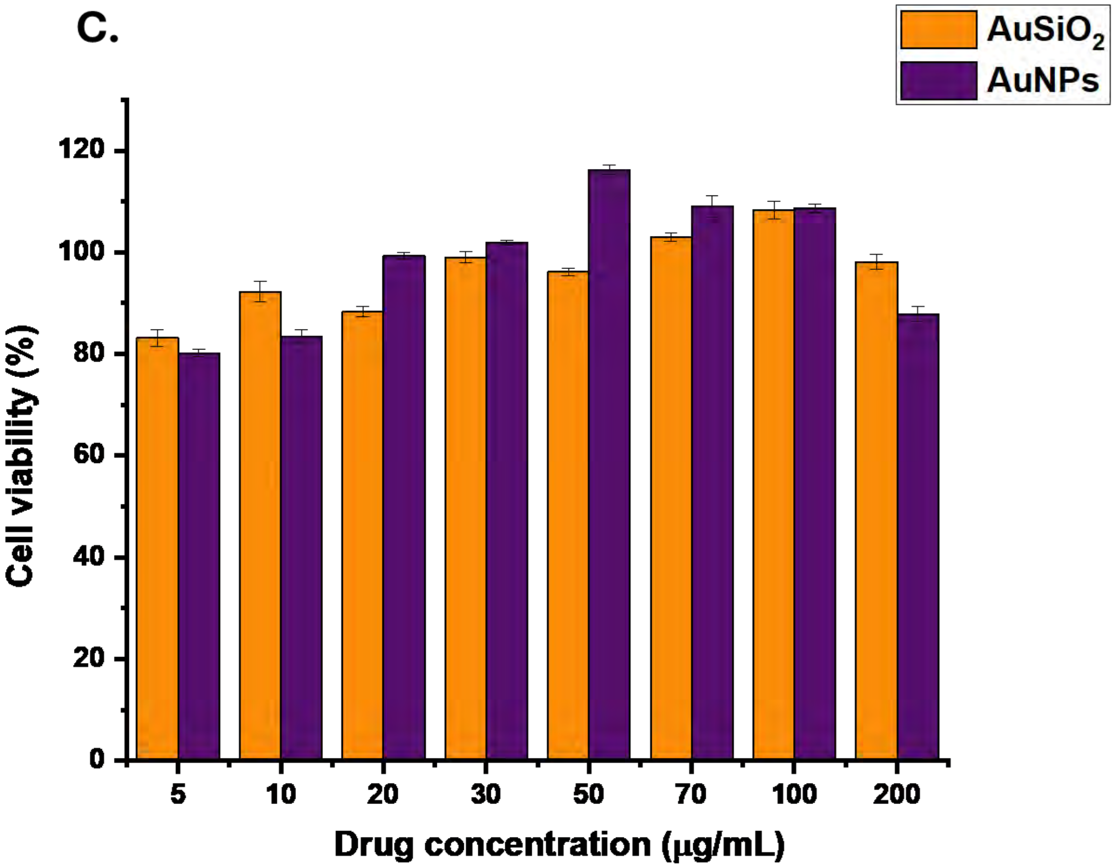

Fig. 4.1. Histograms depicting the viability percentage of MDA-MB-231 cells when treated in the dark with complex **1**, **2**, **3**, and **4** and their conjugates (AuNPs and AuSiO$_2$) *in vitro*.

Table 4.1 Cell viability (%), phototoxic index (PI) and IC_{50} values for porphyrin complexes and nanoconjugates against MDA-MB-231 cancer cells at 200 µg/mL.

Complexes	**Cell Viability %**			**IC_{50}**	
	Light [b]	**Dark [a]**	**PI[c]**	**Light [b]**	**Dark [a]**
1	40.29	91.63	2.27	16.52	>25
2	39.67	92.45	2.33	15.90	>25
3	52.88	81.08	1.53	19.81	>25
4	45.56	80.17	1.76	16.42	>25
1-AuNPs	13.73	80.29	5.85	5.50	>25
2-AuNPs	12.09	75.89	6.28	5.78	>25
3-AuNPs	14.28	86.37	6.05	5.93	>25
4-AuNPs	13.24	76.68	5.80	5.49	>25
1-$AuSiO_2$	15.58	81.39	5.22	5.41	>25
2-$AuSiO_2$	14.06	81.33	5.78	5.43	>25
3-$AuSiO_2$	18.41	93.69	5.10	5.83	>25
4-$AuSiO_2$	15.95	93.81	5.88	5.36	>25
AuNPs	105.18	98.13	0.93	18.58	>25
$AuSiO_2$	98.93	87.86	0.88	22.77	>25

[a] 24 h incubation dark cytotoxicity data, [b] phototoxicity data against MDA-MB-231 cancer cell line upon exposure to a Thorlabs 625 nm LED (30 min). [c] PI = phototoxic index (The ratio of dark to light toxicity).

4.1.2 In vitro photodynamic therapy (PDT).

In vitro PDT studies, the cells were treated with porphyrin complexes and their nanoconjugates at 5-200 µg/mL concentration range and irradiated for 30 min at a continuous light dose of 625 nm Thorlabs LED, **Fig. 4.2**. The IC_{50} values (**Table 4.1**) were used to calculate the concentration required for the conjugates/complexes to destroy 50% of the cells. It was observed that the unmetalled porphyrins (**1** and **3**) performed poorly when compared to their respective metalated porphyrins complexes (**2** and **4**), and this is due to the better singlet oxygen quantum yields production of the metalated porphyrins (**Fig. 4.2**). At the highest concentration (200 µg/mL) complexes **1**, **2**, **3**, and **4** had the cell viability of 40.29%, 39.67%, 52.88% and 45.56% respectively. The AuNPs conjugates **1**-AuNPs (13.73 %), **2**-AuNPs (12.09 %), **3**-AuNPs (14.28 %), **4**-AuNPs (13.24 %) and AuSiO$_2$ conjugates **1**-AuSiO$_2$ (15.58%), **2**-AuSiO$_2$ (14.06%), **3**-AuSiO$_2$ (18.41%) and **4**-AuSiO$_2$ (15.95%), had better PDT performance when compared to their respective unconjugated porphyrins (**1,2,3** and **4**); and they have relatively low IC$_{50}$ values, high PI > 5.0, and low cell viability values < 20% (at higher dye concentration of 200 µg/mL) (**Fig. 4.2, Table 4.1**). This is owing to the favourable synergistic effects of the nanoparticles, which include greater Φ_Δ values, selective accumulation in cancer tumours due to enhanced solubility in aqueous solvents, retention and enhanced drug delivery characteristics [**136**]. Interestingly, the PDT activity of the AuNPs nanoconjugate (**1**-AuNPs, **2**-AuNPs, **3**-AuNPs and **4**-AuNPs) were slightly enhanced relative to that of the AuSiO$_2$ nanoconjugates (**1**-AuSiO$_2$, **2**-AuSiO$_2$, **3**-AuSiO$_2$ and **4**-AuSiO$_2$). This is demonstrated by the slightly lower cell viability values, including a higher PI ratio for the AuNP nanoconjugate; because gold nanoparticles are known to be photothermal and can absorb light into heat through a mechanism called localised surface plasmon resonance (LSPR), which is effective in destroying cancer cells [**136,137**].

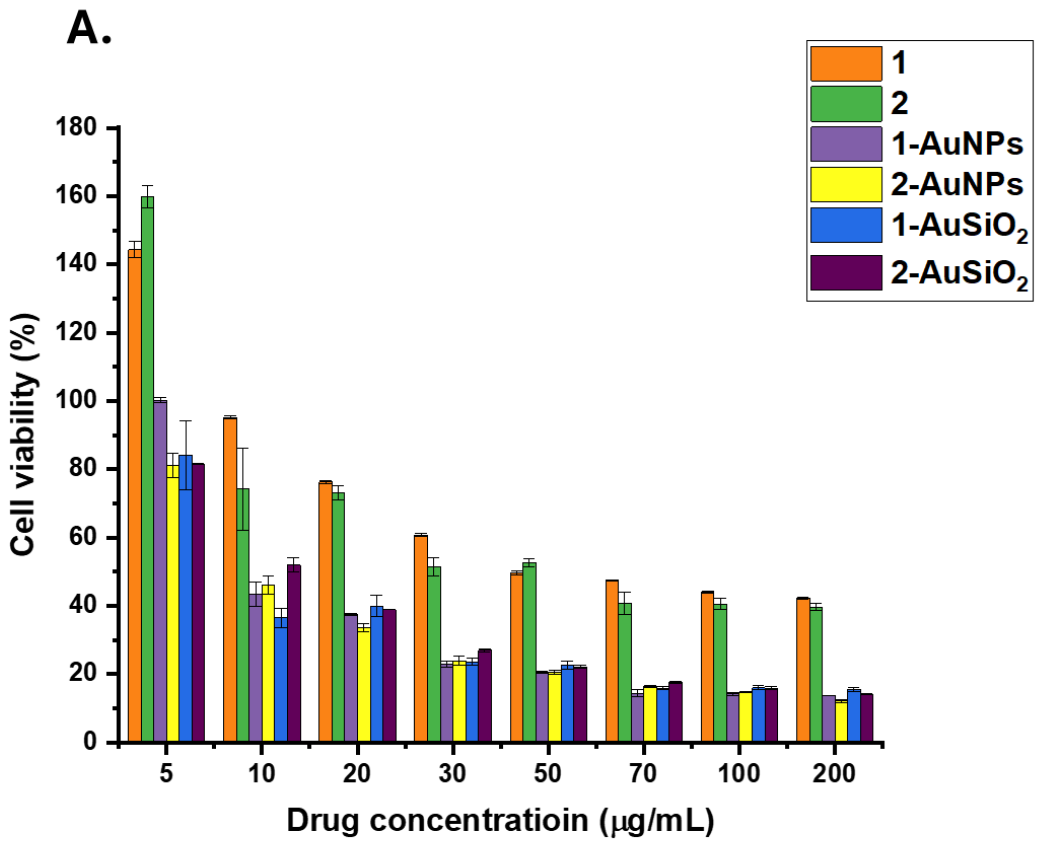
A.
1
2
1-AuNPs
2-AuNPs
1-AuSiO$_2$
2-AuSiO$_2$
Cell viability (%)
0
20
40
60
80
100
120
140
160
180
5
10
20
30
50
70
100
200
Drug concentratioin (μg/mL)

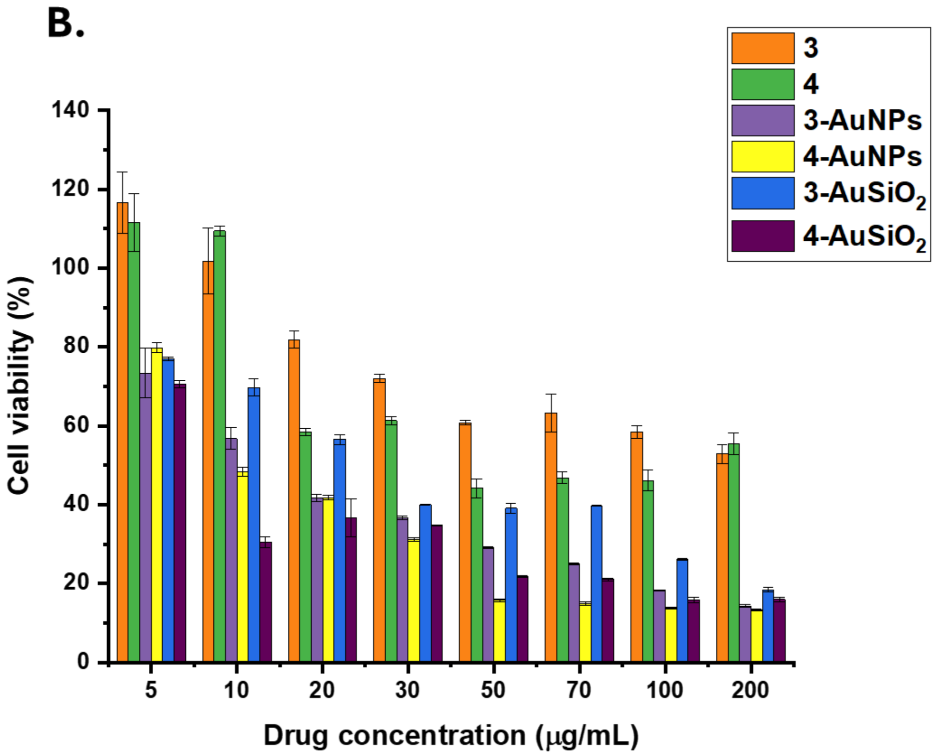
B.
3
4
3-AuNPs
4-AuNPs
3-AuSiO$_2$
4-AuSiO$_2$
Cell viability (%)
0
20
40
60
80
100
120
140
5
10
20
30
50
70
100
200
Drug concentration (μg/mL)

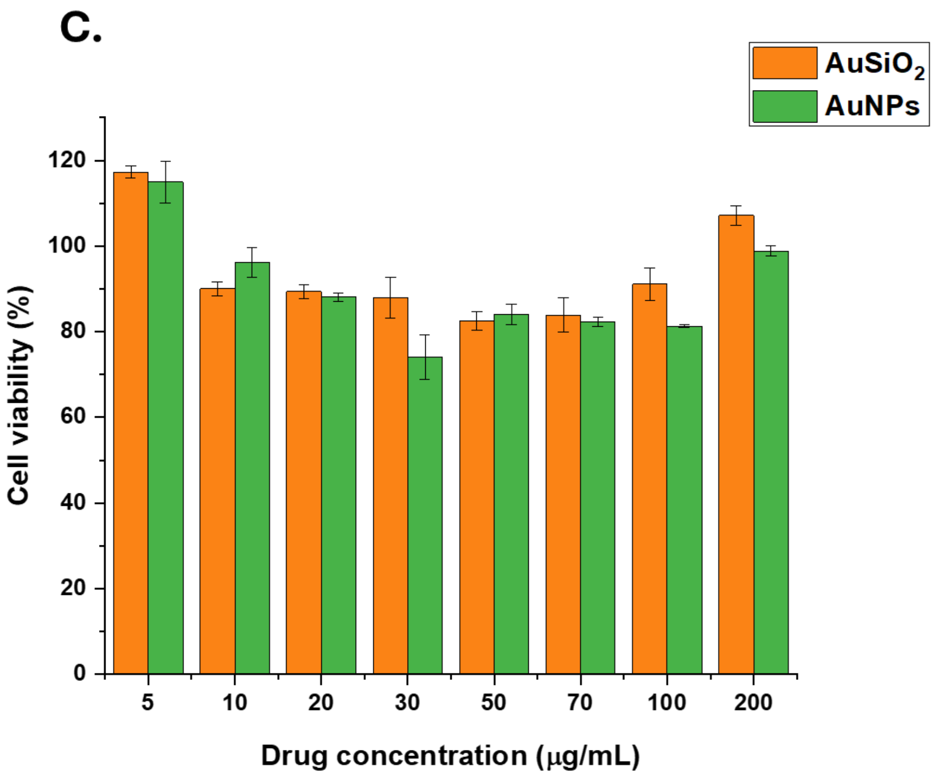

Fig. 4.2. Histograms showing the MDA-MB-231 cell viability (%) after PDT activity of (**A**) Complex **1**, **2** and their nanoconjugate, (**B**) Complex **3**, **4** and their nanoconjugates, (**C**) AuNPs and AuSiO$_2$ NPs *in vitro*.

Microscopic imaging was used to investigate the change in cellular morphology after 24 h (**Fig. 4.3A**) and 48 h (**Fig. 4.3B**) after treatment. **Fig**. **4.3A** and **B** provide an example of images of cells that were not treated and those that were treated with **2**-AuNPs (5, 50 and 200 μg/mL). The MDA-MB-231 cells that are in good health retain their eye-like shape and stick to surfaces. This morphology is observed in the non-treated control samples (**Fig. 4.3A** and **B**), which exhibit primarily living cells.

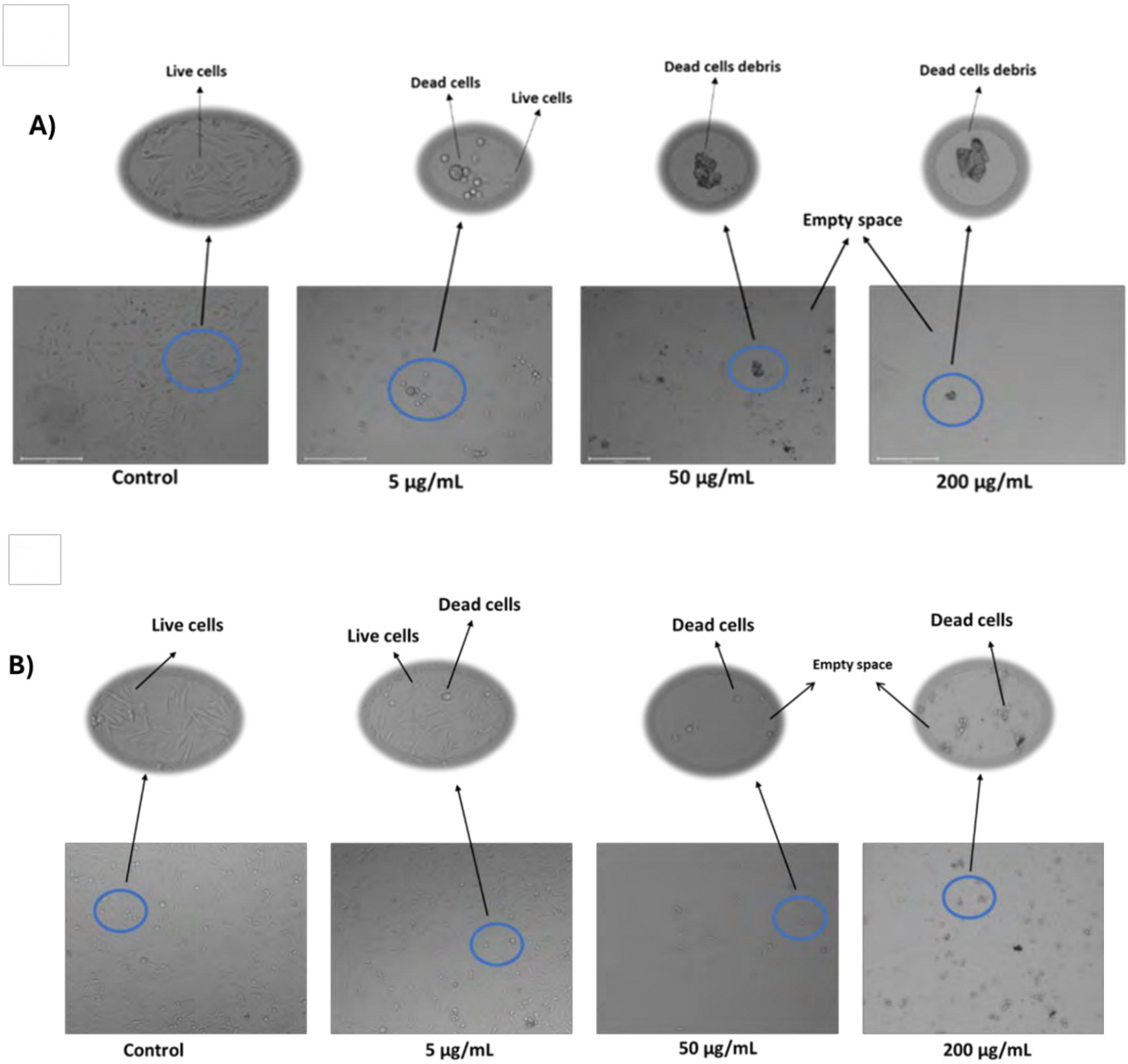

Fig. 4.3. The microscopic images of MDA-MB-231 cells were used as a control (before) and after being treated with **2**-AuNPs in the presence of light at different concentrations 24 h (**A**) and 48 h (**B**) after treatment. Scale: 275 µm.

After the PDT treatment (24 h after), a change in the cellular morphology was seen in the cells. In comparison to the healthy cells, the afflicted cells have shrunk to comparatively smaller sizes and have a round appearance, as can be seen from the treatment image in **Fig. 4.3A** and **B**. Additionally, the dead cells stop adhering to the surface of the 96-well plate and start to rise and float in the cell culture media. When washing, the floating cells are removed, leaving empty spaces on the surfaces, as seen in **Fig. 4.3A** and **B**, with the cells treated with 50 and 200 µg/mL; because of non-adherence, cell death is also suggested by this observation. The MDA-MB-231 cells were also observed 48 h after treatment, and no cell growth was observed (**Fig. 4.3B**).

4.1.3 Cellular uptake

The cellular uptake of all complexes and conjugates was determined by measuring the absorbance of internalized photosensitizer drug after incubating with MDA-MB-231 cancer cells for 24h. The cellular uptake plays an important role in the PDT activity of the photosensitizer [**138**]. **Fig. 4.4A**, shows that $AuSiO_2$ has better cellular uptake compared to AuNPs; this is due to the silica presence in the nanoparticles. The cellular uptake of the porphyrin complexes (complexes **1, 2, 3,** and **4**) were compared to their nanoconjugates, and it was observed that the nanoconjugates had better cellular uptake as compared to the porphyrin complexes alone, as shown in **Fig. 4.4B** and **C.** The presence of the AuNPs and $AuSiO_2$ NPs improved the uptake of the porphyrin complexes. At the highest concentration of 200 µg/mL, the cellular uptake (absorbance) of the porphyrins were 0.11, 0.10, 0.19, and 0.13 for complexes **1**, **2**, **3**, and **4,** respectively (**Fig. 4.4B** and **C)**. The AuNPs conjugates had cellular uptake absorbance of 0.65, 0.28, 0.51, and 0.24 for **1**-AuNPs, **2**-AuNPs, **3**-AuNPs and **4**-AuNPs, respectively, at the concentration of 200 µg/mL. The $AuSiO_2$ conjugates had cellular uptake absorbance of 0.68, 0.69, 0.31, and 0.35 for **1**- $AuSiO_2$, **2**- $AuSiO_2$, **3**- $AuSiO_2$ and **4**- $AuSiO_2$, respectively, at the concentration of 200 µg/mL. Because of the excellent selectivity of gold nanoparticles and silica-gold nanoparticles, nanoconjugates exhibited better uptake than porphyrin complexes alone.

A.

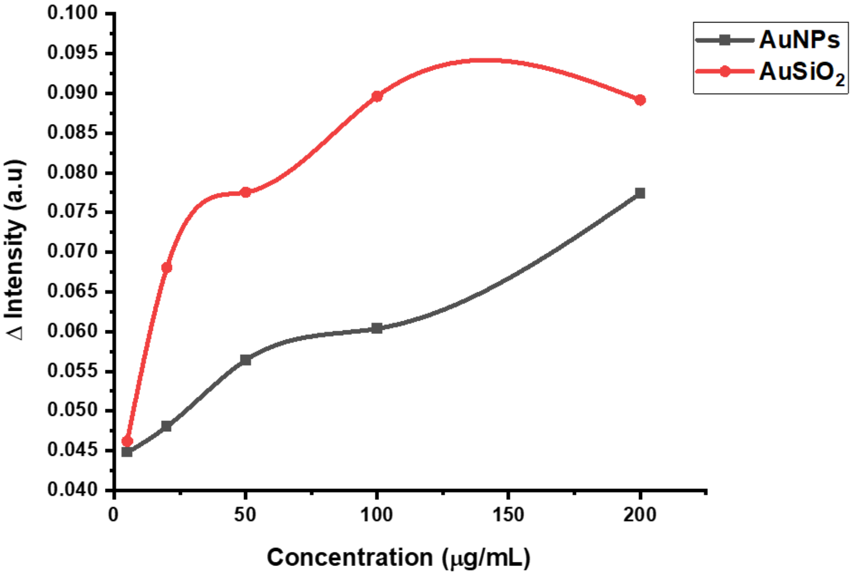
AuNPs
AuSiO$_2$
Δ Intensity (a.u)
0.100
0.095
0.090
0.085
0.080
0.075
0.070
0.065
0.060
0.055
0.050
0.045
0.040
0
50
100
150
200
Concentration (μg/mL)

B.

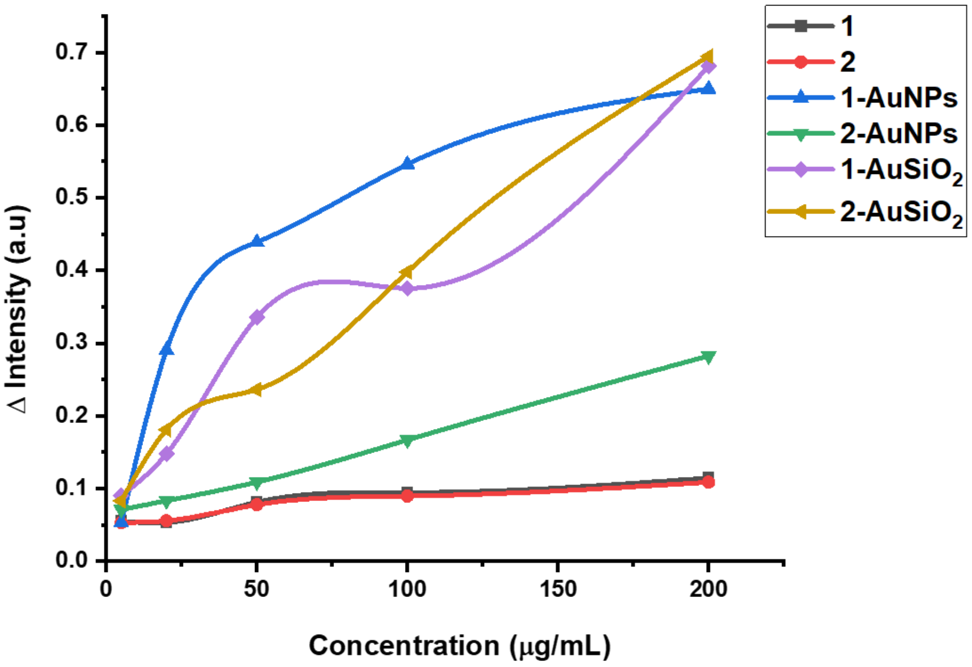
1
2
1-AuNPs
2-AuNPs
1-AuSiO$_2$
2-AuSiO$_2$
Δ Intensity (a.u)
0.7
0.6
0.5
0.4
0.3
0.2
0.1
0.0
0
50
100
150
200
Concentration (μg/mL)

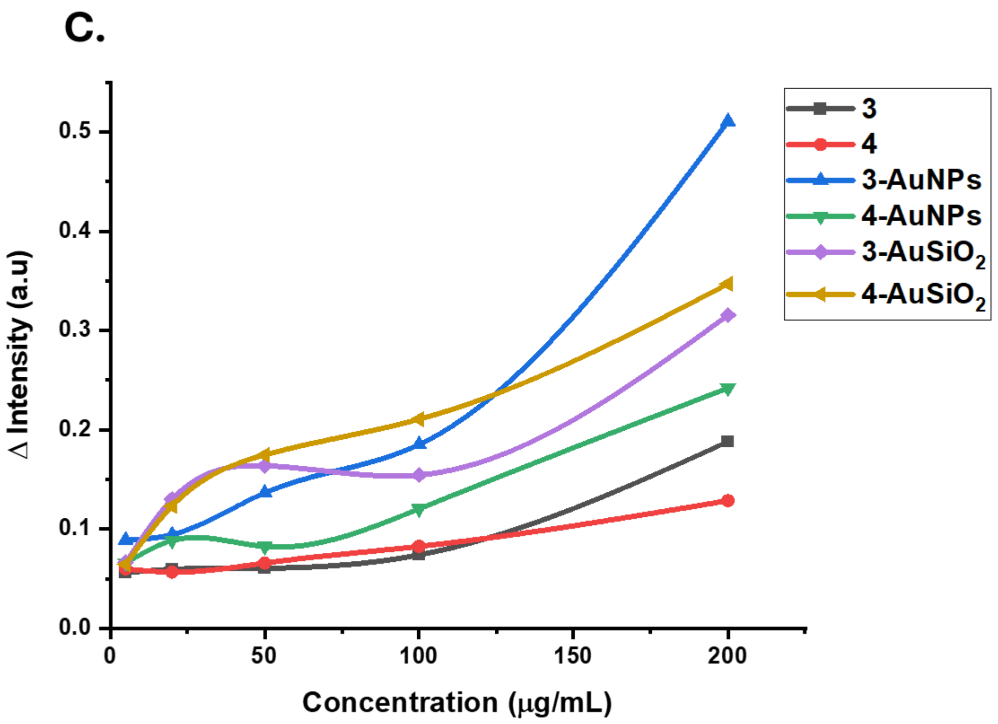

Fig. 4.4 MDA-MB-231 cellular uptake over 24h at different concentrations for (**A**) AuNPs and AuSiO2, (**B**) Complex 1, 2 and their nanoconjugate, (**C**) Complex **3, 4** and their nanoconjugates.

4.2 Chapter summary

The zinc (II) porphyrin dyes exhibited favourable PDT activities since they have slightly higher singlet quantum yield values compared to the free base porphyrins. Conjugation of the porphyrin complexes to the AuNPs and $AuSiO_2$ nanoparticles resulted in enhanced PDT activity. It was also observed that all the complexes and conjugates had no significant dark toxicity towards the MDA-MB-231 cells. The enhanced PDT activity is due to the synergistic effects of the AuNPs and $AuSiO_2$, which enhances the drug penetration into the cancer cells and cellular uptake.

CHAPTER FIVE

Antimicrobial Photodynamic Therapy (aPDT) OF PORPHYRIN DYES.

This chapter outlines detailed antimicrobial photodynamic therapy in vitro photoinactivation studies of methicillin resistance *Staphylococcus aureus* (MRSA) and methicillin-recessive *Staphylococcus aureus* (MSSA) using the as-prepared porphyrin complexes, nanoparticles and their corresponding conjugates.

5.1 Lipophilicity

Amphiphilic complexes exhibit both hydrophilic and lipophilic properties. It has been shown that an increase in the amphiphilicity character of photosensitisers (PSs) is directly related to their attraction to bacteria, which, therefore, increases cellular absorption and overall aPDT performance [**61,139-141**]. A compound that has a negative $\log_P$ value is more hydrophilic and has a stronger affinity for the aqueous phase; when $\log_P = 0$, the compound is evenly distributed across the lipid and aqueous phases and a positive $\log_P$ value indicates a larger concentration in the lipid phase **[141, 142]**. The chloroform-water partitioning coefficient (log $P_{o/w}$) was used to measure the complexes' capacity to penetrate biomembranes or bind to liposomes. The Log $P_{o/w}$ values for the complexes were determined using a procedure reported before [**141**], and the calculations were done using **Eq. 2.1** [**141**]**. Table 5.1** shows the lipophilicity values for all porphyrins. A molecule with Log_P values between 0−5 has the right balance of drug localisation in the aqueous and lipophilic portions of the cells, with superior cellular absorption, penetration, and biodistribution. Notably, porphyrins with the morpholine and thiophene group exhibited negative log P values (hydrophilic), with complex **2 (**log $P_{o/w} = -0.705$**)** having the lowest $\log_P$ value compared to its free-base counterpart (complex **1**). Porphyrin **4** (log $P_{o/w} = 1.141$) displayed the most positive log P values (lipophilic), attributed to the presence of nitrogen groups (**Table 5.1**).

Table 5.1 Water partition coefficient values (Log $P_{o/w}$) of all the porphyrin complexes

Porphyrin Complexes	**Log $P_{o/w}$**
1	-0.074
2	-0.705
3	0.215
4	1.141

5.2 **Antimicrobial studies**

All the antimicrobial studies were conducted using 0.3% DMSO in PBS since the porphyrin complexes were not completely water soluble. aPDT studies were performed in triplicates to ensure the accuracy, validity, and reliability of the data. Gram (+) bacterial strains *Staphylococcus aureus* were employed to study the antibacterial activity of the synthesized complexes. **Eq. 5.1** was employed to quantify the % viable bacterial cells.

$$\text{Viable bacterial cells (\%)} = \frac{treated\ bacterial\ cells}{untreated\ bacterial\ cells}\, x100 \qquad \textbf{[5.1]}$$

5.2.1. *In vitro* aPDT cytotoxicity studies against methicillin-sensitive *S. aureus* (MSSA).

The antimicrobial activities of porphyrin complexes and their conjugates were studied against MSSA and was prepared in 0.3% DMSO. Colony-forming units per mL (CFU/mL) of 10^8 bacteria were incubated with corresponding porphyrin concentrations of 1, 5, 20, 50 and 100 µg/mL. **Table 5.2** summarizes the bacterial % cell viability for all porphyrins and their AuNPs/AuSiO$_2$ nanoconjugates toward planktonic cells of methicillin-sensitive *Staphylococcus aureus* (MSSA), in the absence of light and after 30 min irradiation with 415 nm with a Thorlabs M415L4 LED. All the complexes exhibited high dark toxicity against MSSA with bacterial cell viability of <40%, as shown in **Fig. 5.1A** and **B.** On the other hand, upon light illumination for 30 min, all the porphyrin conjugates exhibited cytotoxicity of <11% in the concentration ranges of 20-100 µg/mL against MSSA, with **4**-AuNPs and **2**-AuSiO$_2$ having the highest activity (**Fig. 5.1 A and B**) (**Table 5.2**), with bacterial cell viability of approximately 0.0% for both complexes. MSSA was also susceptible to Methicillin with cell viability of 2.82± 0.07% at 100 µg/mL (**Fig. 5.1E**).

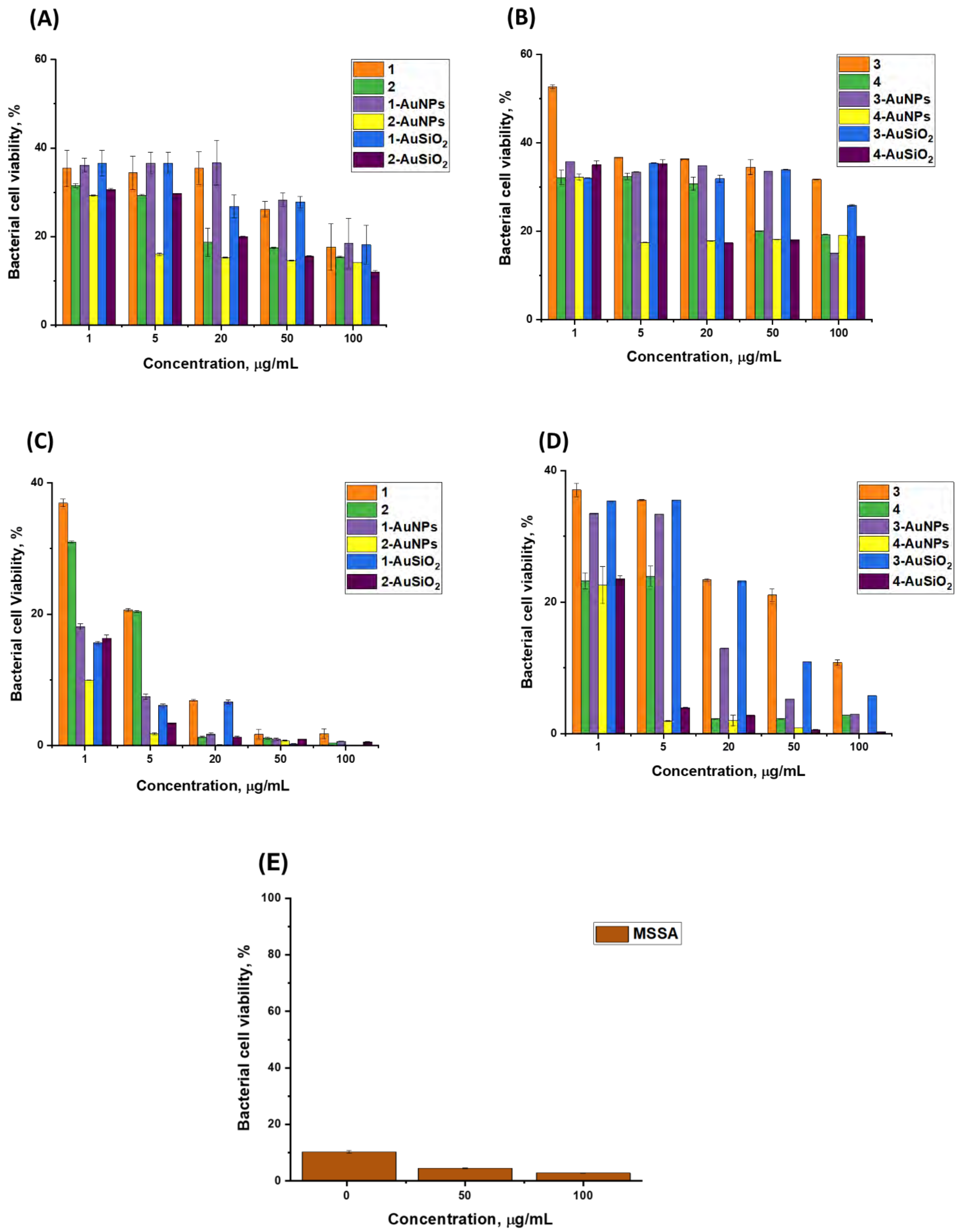

Fig. 5.1 The dark (**A** and **B**) and phototoxicity (**C** and **D**) studies of complexes **1**, **2**, **3**, and **4** and their AuNPs and AuSiO$_2$ conjugates against MSSA in 0.3% DMSO and (**E**) Methicillin drug treatment against MSSA.

Table 5.2. The bacterial % cell viability values at 100 µg/mL concentrations of all porphyrin complexes and their conjugates against planktonic cells of MSSA and MRSA after irradiation with 415 nm LED for 30 min.

Complexes /conjugates	**MSSA**		**MRSA**	
	DARK	**LIGHT**	**DARK**	**LIGHT**
1	17.62±5.2%	1.79±0.72%	89±0.95%	41.69±1.24%
2	15.41±0.15%	0.36±0.0%	71.95±1.87%	21.69±1.24%
3	31.77±0.1%	10.82±0.4%	91.93±0.3%	80.66±0.1%
4	19.28±0.0%	2.80±0.0%	37.56±0.2%	52.61±5.4%
1-AuNPs	18.46±5.65%	0.33±0.0%	86.88±6.7%	0.14±0.0%
2-AuNPs	14.09±0.0%	0.05±0.0%	94.16±0.49%	0.0±0.0%
3-AuNPs	15.03±0.0%	2.99±0.0%	80.00±0.1%	37.78±0.7%
4-AuNPs	19.15±0.0%	0.0±0.0%	84.51±0.2%	0.15±0.2%
1-AuSiO$_2$	18.14±4.3%	0.57±0.0%	85.30±1.86%	8.74±1.20%
2-AuSiO$_2$	12.01±0.3%	0.0±0.0%	99.08±0.1%	0.74±0.1%
3-AuSiO$_2$	25.89±0.1%	5.77±0.0%	94.61±0.3%	75.23±0.2%
4-AuSiO$_2$	18.87±0.0%	0.30±0.0%	70.01±1.5%	5.51±0.0.5%

5.2.2. *In vitro* aPDT cytotoxicity studies against methicillin-resistant S. *aureus* (MRSA).

Concentration optimisation studies of all the porphyrin complexes and their conjugates were performed on MRSA for 30 min irradiation time, as shown in **Fig. 5.2**. The MRSA bacterial cells were treated with the same range of concentrations as used in the MSSA bacterial studies (section 5.2.1). **Table 5.2** summarizes the bacterial % cell viability for the porphyrin complexes and their nanoconjugates toward planktonic cells of Methicillin-resistant *Staphylococcus aureus* (MRSA). It can be clearly seen that all the complexes exhibited low dark toxicity of >70%, as shown in **Fig. 5.2A** and **B**. Upon light exposure for 30 min, **1**-AuNPs (0.14± 0.0%), **2**-

AuNPs (0.0), **4**-AuNPs (0.15± 0.2%), **2**-$AuSiO_2$ (0.74± 0.1%) and **4**-$AuSiO_2$ (5.51± 0.5%), exhibited lowest bacterial cell viability of at 100 µg/mL against MRSA. Complex **3** and its nanoconjugates exhibited the lowest cytotoxicity values (**Table 5.2)**, with bacterial cell viability above 30% at 100 µg/mL. **Fig. 5.2E** also showed the resistance of MRSA towards Methicillin with bacterial cell viability of 82.64± 4.13% at 100 µg/mL. Overall, the MRSA showed more resistance against all the porphyrin complexes and their conjugates between the concentration ranges of 1-50 µg/mL as compared to MSSA (**Figs. 5.1 and 5.2**). Methicillin resistance *Staphylococcus aureus* (MRSA) is encoded by the mecA gene, which is found on a genomic region known as the staphylococcal cassette chromosome mec (SCCmec) element, which has five different forms. SCCmec is a flexible genetic element that can exchange between different staphylococcal species causing it to be resistant to most drugs [**142,143**], which could be the reason for the resistance towards the complexes used in this work.

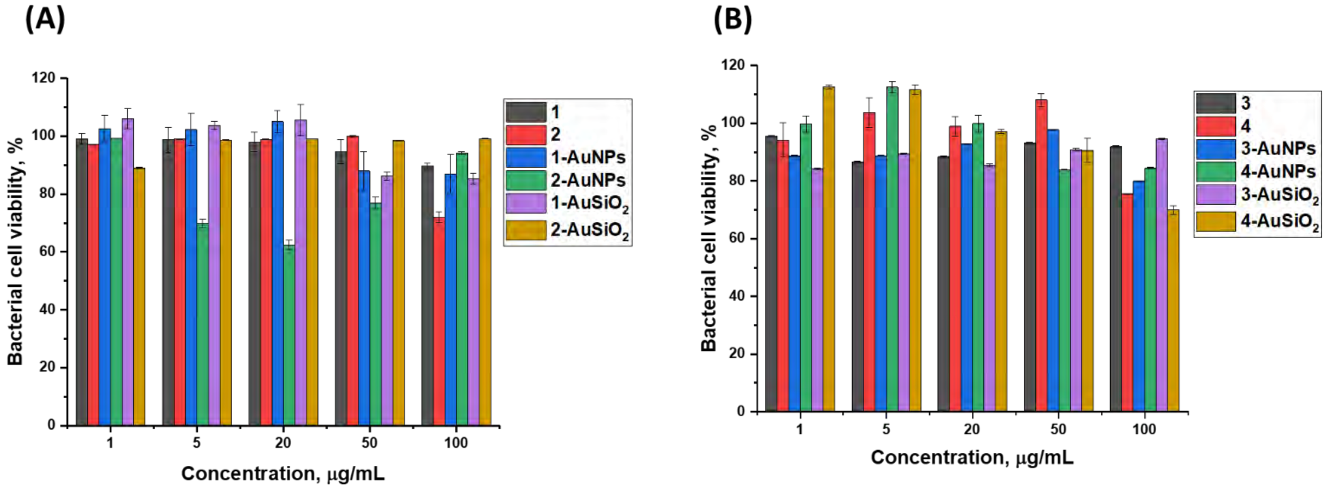

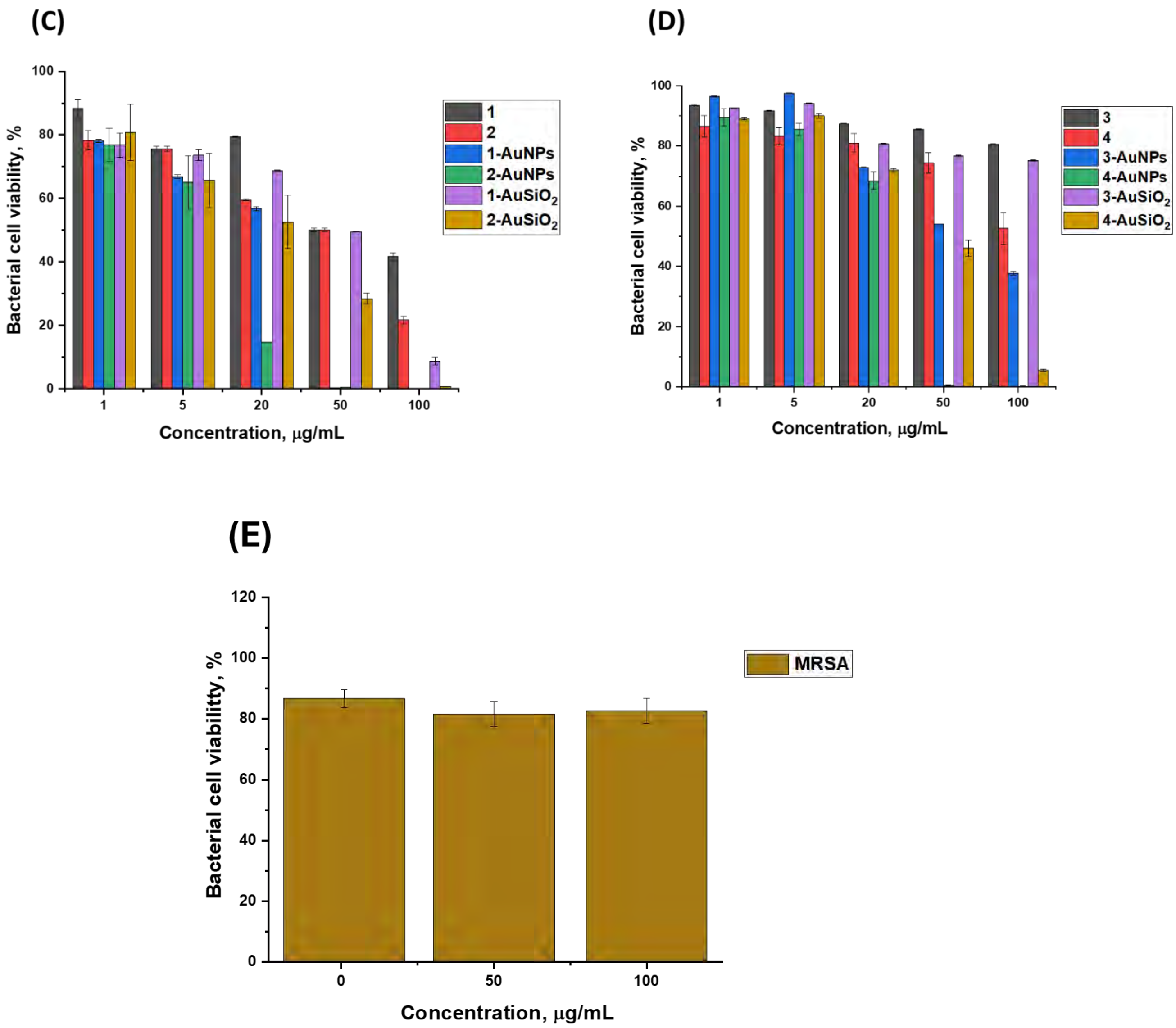

Fig. 5.2 The dark (**A** and **B**) and phototoxicity (**C** and **D**) studies of complexes **1**, **2**, **3**, and **4** and their AuNPs and AuSiO$_2$ conjugates against MRSA in 0.3% DMSO and (**E**) Methicillin drug treatment against MRSA.

Fig. 5.3 shows 96 well plates of complex **2** against (**A**) methicillin-resistant *S. aureus* and (**B**) methicillin-sensitive *S. aureus* upon 30 min irradiation with 415 nm Thorlabs LED at concentrations range of 1-100 µg/mL after incubation for 3 h with resazurin assay dye. Dehydrogenase enzymes in live bacterial cells can reduce resazurin salt (non-fluorescent) to form a pink, highly fluorescent salt resorufin. The intensity of the fluorescence is a measure of the number of viable cells.

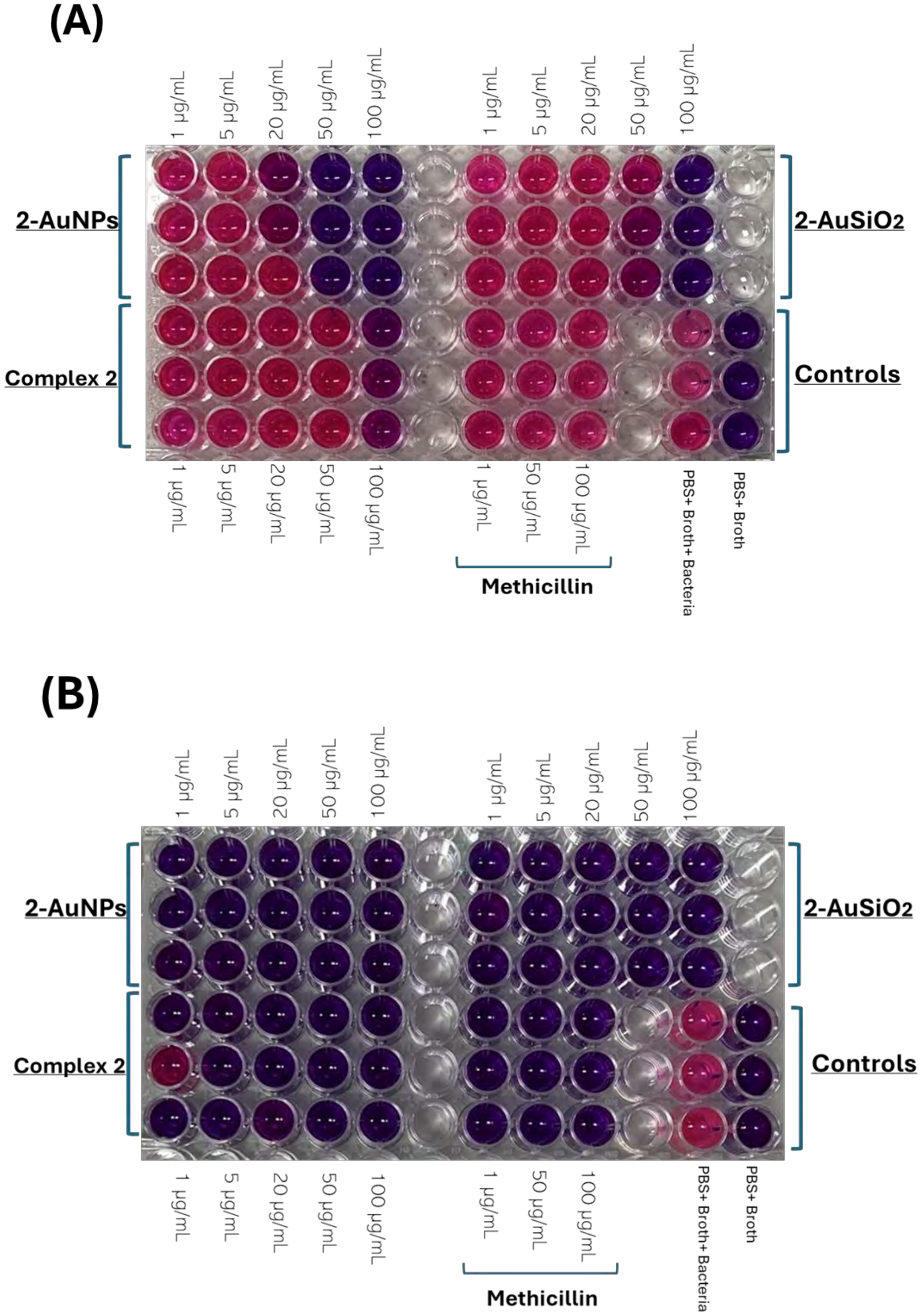

Fig 5.3 96 well plates of complex **2** against (**A**) methicillin-resistant S. *aureus* and (**B**) methicillin-sensitive S. *aureus* upon 30 min irradiation with 415 nm Thorlabs LED.

After 3 h of incubation, the change in colour of the resazurin dye was observed. In comparison to the dead bacterial cells, the healthy metabolically active bacterial cells reduce the blue, non-fluorescent dye resazurin to a pink indicating cell viability and growth, **Fig. 5.3A** (1-20 µg/mL) and **Fig. 5.3B** (1µg/mL). The dead bacterial cells metabolic processes stop, inhibiting the reduction of the resazurin dye to resorufin thus the colour remains blue as seen in **Fig. 5.3A** in the higher concentrations (50 and 100 µg/mL) and **Fig. 5.3B.** MRSA cells are resistant to methicillin, the bacterial cells remains active after the methicillin treatment and reduces the blue dye to pink (**Fig. 5.3A**), contrary to MRSA, MSSA cells are sensitive to methicillin and can be killed by the lowest concentration (1 µg/mL) thus there was no colour change observed (**Fig. 5.3B**). The results In **Fig. 5.3A** and **B** are in strong agreement with cell viability results in **Fig**. **5.1** and **5.2** for complex **2** and its AuNPs/AuSiO$_2$ conjugates.

5.3 Summary of the chapter

In vitro antimicrobial photodynamic therapy activity of all porphyrin complexes **1**, **2**, **3**, and **4** and their AuNPs/AuSiO$_2$ conjugates **1**-AuNPs/AuSiO$_2$, **2**-AuNPs/AuSiO$_2$, **3**-AuNPs/AuSiO$_2$, and **4**-AuNPs/AuSiO$_2$ were assessed on both methicillin-resistant *S. aureus* and methicillin-sensitive *S. aureus*. Both dark and light toxicity were assessed at concentrations range of 1-100 µg/mL over 30 min. The conjugates were found to have significantly higher photodynamic antimicrobial activity (aPDT) against planktonic Gram-(+) cells of methicillin-sensitive *Staphylococcus aureus* (MSSA) as compared to methicillin-resistant *Staphylococcus aureus* (MRSA). The aPDT against methicillin-sensitive *S. aureus* activities of the nanoconjugates were significantly enhanced upon conjugation to AuNPs/AuSiO$_2$ and exhibited high dark toxicity, with bacterial cell viability of <40%. Interestingly, all the complexes showed the highest aPDT activity against MRSA at the highest concentration of 100 µg/mL with low dark toxicity of bacterial cell viability of >70 %. Overall, the MRSA showed more resistance against all the porphyrin complexes and their conjugates between the concentration ranges of 1-50 µg/mL as compared to MSSA.

CHAPTER SIX

Conclusions

This chapter outlines conclusive remarks based on the studies conducted. Recommendations for further studies are provided.

6.1 Conclusions

This thesis reports for the first time on the asymmetrical A_2B_2 sulfur substituted porphyrins conjugated to AuNPs and $AuSiO_2$ through the Au-S/N bond for in vitro PDT of MDA-MB-231 cancerous cells and aPDT photoinactivation of Gram-positive methicillin-sensitive and methicillin-resistant *S. aureus* bacterial strains. Confirmation of the successful syntheses of the porphyrins, nanoparticles, and conjugates was assessed using appropriate analytical instruments. The porphyrins were self-assembled on the exposed AuNPs surface via Au-S or Au-N bond formation. XPS and FTIR were employed to prove the conjugations and bond formations on nanoconjugates.

All the porphyrin (**1** and **3**) complexes were metalated with zinc metal to improve the photophysicochemical properties. Methylthiophenyl and the thiophene meso-substituents porphyrins were used since they are known to have higher toxicity against a broad spectrum of microbes. Complex **2** (ϕ_Δ = 0.48) and **4** (ϕ_Δ = 0.49) were observed to have relatively improved singlet oxygen quantum yields compared to their free-base porphyrins, complex **1**(ϕ_Δ = 0.46) and **3** (ϕ_Δ = 0.20), and this was expected since the heavy zinc metal atom is known to facilitate the intersystem crossing from the singlet excited PSs to the triplet excited states which positively impact the singlet oxygen generation. The photothermal effect of AuNPs was evaluated by measuring temperature changes under irradiation, and a detectable temperature stabilization was observed after 30 min at 4.89 °C. Upon the formation of the conjugates, overall improved singlet oxygen quantum yields were observed, and this was attributed to the presence of the NPs, which brings external heavy atom effect.

6.2 Future recommendation

Towards the development of potential photosensitizers for PDT and aPDT, exploration of solubility strategies, such as the introduction of cationic species such as quaternary ammonium moieties, axial ligation with water-soluble derivatives, including core-functionalization of the dyes with hexadentate coordination ions, such as Sn(IV), that introduce axial ligands from above and below the porphyrin ring should be explored. Encapsulation of PSs drugs using micelles and liposomes can enhance their solubility properties.

Conjugation of the porphyrin dyes to up-conversion metallic nanoparticles or nano-assemblies, including conjugation with cancer receptors moieties, such as antibodies that have specific affinities to the cancer cells or bacteria cell walls, can improve the performances of PS dyes.

References

1. S. Rajesh, E. Koshi, K. Philip, and A. Mohan, Antimicrobial photodynamic therapy: An overview. J. Indian Soc. of Periodontol., 15 (2011) 323.
2. M. Carrel, E.N. Perencevich, and M.Z. David, USA300 methicillin-resistant *Staphylococcus aureus*, United States, 2000–2013. Emerg. Infect. Dis., 21 (2015) 1973.
3. H. Abrahamse, and M.R. Hamblin, New photosensitizers for photodynamic therapy. Biochem. J., 473 (2016) 347.
4. G. Gunaydin, M. Emre Gedik, and S. Ayan, Photodynamic Therapy for the Treatment and Diagnosis of Cancer-A Review of the Current Clinical Status. Front. Chem., (2021) 686303.
5. C. Moorthi, R. Manavalan, and K.J. Kathiresan, Nanotherapeutics to overcome conventional cancer chemotherapy limitations. Pharm. Pharm. Sci., 14 (2011) 67.
6. O. Casanovas, Limitations of therapies exposed. Nat., 484 (2012) 44.
7. J. Chen, T. Fan, Z. Xie, Q. Zeng, P. Xue, T. Zheng, Y. Chen, X. Luo, and H. Zhang, Advances in nanomaterials for photodynamic therapy applications: Status and challenges. Biomater., 237 (2020) 119827.
8. A. Moten, D. Schafer, and M. Ferrari, Redefining global health priorities: Improving cancer care in developing settings. J. Glob. Health, 4 (2014) 010304.
9. M. Roser, F. Spooner, and H. Ritchie, Our World in Data. (2018). https://ourworldindata.org/causes-of-death (Accessed: 06-10-2024)
10. World Health Organization (2024, August 1), Global cancer burden growing, amidst mounting need for services. https://www.who.int/news/item/01-02-2024-global-cancer-burden-growing--amidst-mounting-need-for-services
11. L. Yin, J.J. Duan, X.W. Bian, and S.C. Yu, Triple-negative Breast Cancer Molecular Subtyping and Treatment Progress. Breast Cancer Res., 22 (2020) 1.
12. N. Plekhova, O. Shevchenko, O. Korshunova, A. Stepanyugina, I. Tananaev, and V. Apanasevich, Development of Novel Tetrapyrrole Structure Photosensitizers for Cancer Photodynamic Therapy. Bioeng., 9 (2022) 82.

13. A.B. Ormond, and H.S. Freeman, Dye sensitizers for photodynamic therapy. Mater., 6 (2013) 817.

14. M. Lan, S. Zhao, W. Liu, C.S. Lee, W. Zhang, and P. Wang, Photosensitizers for photodynamic therapy. Adv. Healthc. Mater., 8 (2019) 1900132.

15. K.N. Maloth, N. Velpula, N. Kodangal, S. Sngmesh, M. Vellamchetla, K. Ugrappa, and S. Meka, Photodynamic Therapy – A Non-invasive Treatment Modality for Precancerous Lesions. J. Lasers Med. Sci., 7 (2016) 30.

16. A.F. Dos Santos, D.R.Q. De Almeida, L.F. Terra, M.S. Baptista, and L. Labriola, Photodynamic therapy in cancer treatment - an update review. J. Cancer Metastasis Treat., 5 (2019) 25.

17. A. Escudero, C. Carrillo-Carrió, C. Castillejos, E. Romero-Ben, C. Rosales-Barrios, and N. Khiar, Photodynamic therapy: photosensitizers and nanostructures. Mater. Chem. Front., 5 (2021) 3788.

18. S. Kwiatkowski, B. Knap, D. Przystupski, J. Saczko, E. Kędzierska, K. Knap-Czop, J. Kotlińska, O. Michel, K. Kotowski, and J. Kulbacka, Photodynamic therapy-mechanisms, photosensitizers and combinations. Biomed. Pharmacother, 106 (2018) 1098.

19. P. Washer and H. Joffe, The "hospital superbug":Social representation of MRSA. Social Sci. Medicine, 63 (2006) 2141.

20. N. Kashef, and M.R. Hamblin, Can microbial cells develop resistance to oxidative stress in antimicrobial photodynamic inactivation?. Drug Resist. Updat., 31 (2017) 31.

21. H. Mahmoudi, A. Bahador, M. Pourhajibagher, and M. Yousef Alikhani, Antimicrobial Photodynamic Therapy: An Effective Alternative Approach to Control Bacterial Infections. Laser Appl. Med. Sci. Res. Cent., 9 (2018) 154.

22. J. Ghorbani, D. Rahban, S. Aghamiri, A. Teymouri, and A. Bahador, Photosensitizers in antibacterial photodynamic therapy: An overview. Laser Ther., 27 (2018) 293.

23. R. Youf, M. Müller, A. Balasini, F. Thétiot, M. Müller, A. Hascoët, U. Jonas, H. Schönherr, G. Lemercier, T. Montier, and T. Le Gall, Antimicrobial photodynamic therapy: Latest developments with a focus on combinatory strategies. Pharmaceutics, 13 (2021) 1.

24. F. Cieplik, D. Deng, W. Crielaard, W. Buchalla, E. Hellwig, A. Al-Ahmad, and T. Maisch, Antimicrobial photodynamic therapy–what we know and what we don't. Crit. Rev. Microbiol, 44 (2018) 571.

25. J.E. McGowan Jr, Antimicrobial resistance in hospital organisms and its relation to antibiotic use. Rev. Infect. Dis., 5 (1983) 1033.

26. M. Tahoun, C.T. Gee, V.E. McCoy, P.M. Sander, and C.E. Müller, Chemistry of porphyrins in fossil plants and animals. RSC Adv., 11 (2021) 7552.

27. M.A García-Sánchez, F. Rojas-González, E.C. Menchaca-Campos, S.R. Tello-Solís, R.I.Y. Quiroz-Segoviano, L.A. Diaz-Alejo, E. Salas-Bañales, and A. Campero, Crossed and linked histories of tetrapyrrolic macrocycles and their use for engineering pores within sol-gel matrices. Molecules, 18 (2013) 588.

28. C.S.Y. Lin, M.J. Lee, S.B. Park, and M.C. Kiernan, Purple pigments: the pathophysiology of acute porphyric neuropathy. Clin. Neurophysiol., 122 (2011) 2336.

29. C.J. Watson, and E.A. Larson, The urinary coproporphyrins in health and disease. Physiol. Rev., 27 (1947) 478.

30. A.R. Battersby, Tetrapyrroles: the pigments of life. Nat. Prod. Rep., 17 (2000) 507.

31. Z. Chen, A. Lohr, C.R. Saha-Möller, and F. Würthner, Self-assembled π-stacks of functional dyes in solution: structural and thermodynamic features. Chem. Soc. Rev., 38 (2009) 564.

32. O.I. Koifman, and T.A. Ageeva, Main Strategies for the Synthesis of meso-Arylporphyrins. Russ. J. Org. Chem., 58 (2022) 443.

33. M. Da, G.H. Vicente, and K.M. Smith, Syntheses and Functionalizations of Porphyrin Macrocycles. Curr. Org. Synth., 11 (2014) 3.

34. P. Rothemund, and A.R. Menotti, Porphyrin Studies. IV.1 The Synthesis of α,β,γ,δ-Tetraphenylporphine. J. Am. Chem. Soc., 63 (1941) 267.

35. A.D. Adler, F.R. Longo, and W. Shergalis, Mechanistic investigations of porphyrin syntheses. I. Preliminary studies on ms-tetraphenylporphin. J. Am. Chem. Soc., 86 (1964) 3145.

36. A.D. Adler, F.R. Longo, J.D. Finarelli, J. Goldmach, J. Assour, and L. Korsakof, A simplified synthesis for Meso-Tetraphenylporphine. J. Org. Chem., 32 (1967) 476.

37. M.G.H. Vicente, and K.M. Smith, Porphyrins and Derivatives Synthetic Strategies and Reactivity Profiles. Curr. Org. Chem., 4 (2000) 139.

38. J.S. Lindsey, The synthesis of meso-substituted porphyrins. Montanari F and Casella L (Eds.). Metalloporphyrins Catalyzed Oxidations. Kluwer Academic Publishers, Netherlands, (1994) 49.

39. K.M. Smith. Development of porphyrin syntheses. New J. Chem., 40 (2016) 5644.

40. J. Zhang, C. Jiang, J.P.F. Longo, R.B. Azevedo, H. Zhang and L.A. Muehlmann, An updated overview on the development of new photosensitizers for anticancer photodynamic therapy. Acta Pharm. Sin. B., 8 (2018) 137.

41. P. Faugeras, J. Vergnaud, R. Lucas, B. Boe, K. Teste, and R. Zerrouki, Iodine-catalyzed one-pot synthesis of unsymmetrical meso-substituted porphyrins. Tetrahedron, 66 (2010) 1994.

42. B.F. Nascimento, M. Pineiro, A.M.D.A. Rocha Gonsalves, M. Ramos Silva, A. Matos Beja, and J.A. Paixão, Microwave-assisted synthesis of porphyrins and metalloporphyrins: a rapid and efficient synthetic method. J. Porphyr. Phthalocyanines, 11 (2007) 77.

43. C.O. Kappe, A. Stadler, and D. Dalinger, In Microwaves in Organic and Medicinal Chemistry. R. Mannhold R., Kubinyi H., Folkers G. John Wiley & Sons, Germany, 52 (2012).

44. H. Lu, and N. Kobayashi, optically active porphyrin and phthalocyanine systems. Chem. Rev., 116 (2016) 6184.

45. M. Gouterman, Spectra of Porphyrins. J. Mol. Spectrosc., 6 (1961) 138.

46. R. Giovannetti, The Use of Spectrophotometry UV-Vis for the Study of Porphyrins, In Macro to nano spectroscopy. J. Uddin, IntechOpen, Camerino Italy, 2012.

47. C. Weiss, H. Kobayashi, and M. Gouterman, Spectra of porphyrins: Part III. Self-consistent molecular orbital calculations of porphyrin and related ring systems. J. Mol. Spectrosc., 16 (1965) 415.

48. B. Valeur, and M.N. Berberan-Santos, Molecular fluorescence: principles and applications. John Wiley & Sons: Hoboken, New Jersey, 2012.

49. K. Michael, Characterization of electronic transitions in complex molecules. Discuss. Faraday Soc., 9 (1950) 14.

50. A. Matarazzo, and R.H. Hudson, Fluorescent adenosine analogs: a comprehensive survey. Tetrahedron, 11 (2015) 1627.

51. S.W. Hell, and M. Kroug, Ground-state-depletion fluorescence microscopy: A concept for breaking the diffraction resolution limit. Appl. Phys. B., 60 (1995) 495.

52. S. Fery-Forgues, and D. Lavabre, Are fluorescence quantum yields so tricky to measure? A demonstration using familiar stationery products. J. Chem. Educ., 76 (1999) 1260.

53. H.L. Kee, J. Bhaumik, J.R. Diers, P. Mroz, M.R. Hamblin, D.F. Bocian, J.S. Lindsey, and D. Holten, Photophysical characterization of imidazolium-substituted Pd(II), In(III), and Zn(II) porphyrins as photosensitizers for photodynamic therapy. J. Photochem. Photobiol. A: Chem., 200 (2008) 346.

54. M. Imran, M. Ramzan, A.K. Qureshi, M.A. Khan, and M. Tariq, Emerging applications of porphyrins and metalloporphyrins in biomedicine and diagnostic magnetic resonance imaging. Biosens., 8 (2018) 95.

55. J.M. Dabrowski, M. Krzykawska, L.G. Arnaut, M.M. Pereira, C.J.P. Monteiro, S. Simões, K. Urbańska and G. Stochel, Tissue Uptake Study and Photodynamic Therapy of Melanoma-Bearing Mice with a Nontoxic, Effective Chlorin. Chem. Med. Chem., 6 (2011) 1715.

56. R. Baskaran, J. Lee, and S.G. Yang, Clinical development of photodynamic agents and therapeutic applications. Biomater. Res., 22 (2018) 25.

57. S. Hackbarth, B. Ro, W. Spiller, H. Kliesch and D.J. Worle, Singlet Oxygen Quantum Yields of Different Photosensitizers in Polar Solvents and Micellar Solutions. J. Porphyr. Phthalocyanines, 2 (1998) 145.

58. F. Ricchelli, Photophysical properties of porphyrins in biological membranes, J. Photochem. Photobiol. B: Biol., 29 (1995) 109.

59. R.W. Redmond, and J.N. Gamlin, A compilation of singlet oxygen yields from biologically relevant molecules. Photochem. Photobiol., 70 (1999) 391.

60. T.Y. Ohulchanskyy, D.J. Donnelly, M.R. Detty, and P.N. Prasad, Heteroatom substitution induced changes in excited-state photophysics and singlet oxygen generation in chalcogenoxanthylium dyes: Effect of sulfur and selenium substitutions. J. Phys. Chem. B., 108 (2004) 8668.

61. B. Babu, R.C. Soy, J. Mack, and T. Nyokong, Non-aggregated lipophilic water-soluble tin porphyrins as photosensitizers for photodynamic therapy and photodynamic antimicrobial chemotherapy. New J. Chem., 44 (2020) 11006.

62. S.R. Mudshinge, A.B. Deore, S. Patil, and C.M. Bhalgat, Nanoparticles: Emerging carriers for drug delivery, Saudi Pharm. J., 19 (2011) 129.

63. P. García Calavia, G. Bruce, L. Pérez-García, and D.A. Russell, Photosensitiser-gold nanoparticle conjugates for photodynamic therapy of cancer. Photochem. Photobiol. Sci., 17 (2018) 1534.

64. G. Pasparakis, Recent developments in the use of gold and silver nanoparticles in biomedicine. WIREs: Nanomed. Nanobiotechnol., 14 (2022) 1817.

65. M.J. Mitchell, M.M. Billingsley, R.M. Haley, M.E. Wechsler, N.A. Peppas, and R. Langer, Engineering precision nanoparticles for drug delivery. Nat. Rev. Drug Discov., 20 (2021) 101.

66. J. Sun, S. Kormakov, Y. Liu, Y. Huang, D. Wu, and Z. Yang, Recent Progress in Metal-Based Nanoparticles Mediated Photodynamic Therapy. Molecules, 23 (2018) 1704.

67. A. Albanese, P.S. Tang, and W.C. Chan, The Effect of Nanoparticle Size, Shape, and Surface Chemistry on Biological Systems. Annu. Rev. Biomed. Eng.,14 (2012) 1.

68. R. Singh, Jr. J.W. Lillard, Nanoparticle-based targeted drug delivery. Exp. Mol. Pathol., 86 (2009) 215.

69. S. Tran, P.J. DeGiovanni, B. Piel, and P. Rai, Cancer nanomedicine: a review of recent success in drug delivery. Clin. Trans. Med., 6 (2017) 1.

70. M.G. Mokwena, C.A. Kruger, M.T. Ivan, and H. Abrahamse, A review of nanoparticle photosensitizer drug delivery uptake systems for photodynamic treatment of lung cancer. Photodiagnosis Photodyn. Ther., 22 (2018) 147.

71. Z. Cheng, M. Li, R. Dey, and Y. Chen, Nanomaterials for cancer therapy: current progress and perspectives. J. Hematol. Oncol., 14 (2021) 1.

72. S. Shariatzadeh, N. Moghimi, F. Khalafi, S. Shafiee, M. Mehrabi, S. Ilkhani, F. Tosan, P. Nakhaei, A. Alizadeh, R.S. Varma, and M. Taheri, Metallic Nanoparticles for the Modulation of Tumor Microenvironment; A New Horizon. Front. Bioeng. Biotechnol., 10 (2022) 847433.

73. S. Barazzouk, L. Bekalé, and S. Hotchandani, Enhanced photostability of chlorophyll-a using gold nanoparticles as an efficient photoprotector. J. Mater. Chem., 22 (2012) 25316.

74. M.A. Sherwani, S. Tufail, A.A. Khan, and M. Owais, Gold nanoparticle-photosensitizer conjugate based photodynamic inactivation of biofilm producing cells: potential for treatment of C. albicans infection in BALB/c mice. PLoS One, 10 (2015) 0131684.

75. A.Z. Wilczewska, K. Niemirowicz, K.H. Markiewicz, and H. Car, 2012. Nanoparticles as drug delivery systems. Pharmacol. Rep., 64 (2012) 1020.

76. M. Sivasubramanian, Y.C. Chuang, and L.W. Lo, Evolution of nanoparticle-mediated photodynamic therapy: from superficial to deep-seated cancers. Mol., 24 (2019) 520.

77. T.C. Pagonis, J. Chen, C.R. Fontana, H. Devalapally, K. Ruggiero, X. Song, F. Foschi, J. Dunham, Z. Skobe, H. Yamazaki, and R. Kent, Nanoparticle-based endodontic antimicrobial photodynamic therapy. J. Endod., 36 (2010) 322.

78. Z. Jing, Q. Du, X. Zhang, and Y. Zhang, Nanomedicines and nanomaterials for cancer therapy: Progress, challenge and perspectives. Chem. Eng. J., 446 (2022) 137147.

79. F. Lavaee, M. Motamedifar, and G. Rafiee, The effect of photodynamic therapy by gold nanoparticles on *Streptococcus* mutans and biofilm formation: An in vitro study. Lasers Med. Sci., (2021) 1.

80. H. Montaseri, C.A. Kruger, and H. Abrahamse, Recent advances in porphyrin-based inorganic nanoparticles for cancer treatment. Int. J. Mol. Sci., 21 (2020) 3358.

81. E.B. Dickerson, E.C. Dreaden, X. Huang, I.H. El-Sayed, H. Chu, S. Pushpanketh, J.F. McDonald, and M.A. El-Sayed, Gold nanorod assisted near-infrared plasmonic

photothermal therapy (PPTT) of squamous cell carcinoma in mice. Cancer Lett., 269 (2008) 57.

82. T.P. Mthethwa, S. Tuncel, and T. Nyokong, Photophysical and photochemical properties of a novel thiol terminated low symmetry zinc phthalocyanine complex and its gold nanoparticles conjugate. Dalton Trans., 42 (2013) 4922.

83. P. Calzavara-Pinton, M. Rossi, S. Raffaella, and V. Marina, Photodynamic Antifungal Chemotherapy. Photochem. Photobiol., 88 (2012) 512.

84. A. Rai, and C.C. Perry, Antibiotic mediated synthesis of gold nanoparticles with potent antimicrobial activity and their application in antimicrobial coatings. J. Mater. Chem., 20 (2010) 6789.

85. R. Ranganathan, S. Madanmohan, A. Kesavan, G. Baskar, Y.R. Krishnamoorthy, R. Santosham, D. Ponraju, S.K. Rayala, and G. Venkatraman, Nanomedicine: Towards development of patient-friendly drug-delivery systems for oncological applications. Int. J. Nanomedicine, 7 (2012) 1043.

86. A.C. Anselmo and S. Mitragotri, Nanoparticles in the clinic: An update. Bioeng. Transl. med., 4 (2019) 10143.

87. J. Gomez-Marquez, and K. Hamad-Schifferli, Local development of nanotechnology-based diagnostics. Nat. Nanotechnol., 16 (2021) 484.

88. Y. Liu, Y. Yao, J. Fu, W. Hu, J. Feng, J. Wan and C. Yu, Large-scale synthesis of fractal silica nanoparticles: understanding the impact of solvents. Micropor. Mesopor. Mat., 316 (2021) 110976.

89. J. Fu, J. Jiao, W. Ban, Y. Kong, Z. Gu, H. Song, X. Huang, Y. Yang, and C. Yu, Large-scale synthesis of self-assembled shuttlecock-shaped silica nanoparticles with minimized drag as advanced catalytic nanomotors. Chem. Eng. J., 417 (2021) 127971.

90. W. Stöber, A. Fink, and E. Bohn, Controlled growth of monodisperse silica spheres in the micron size range. J. colloid. Interface Sci., 26 (1968) 62.

91. Z. Zhelev, H. Ohba, and R. Bakalova, Single Quantum Dot-Micelles Coated with Silica Shell as Potentially Non-Cytotoxic Fluorescent Cell Tracers. J. Am. Chem. Soc., 128 (2006) 6324.

92. X. Zhao, R.P. Bagwe, and W. Tan, Development of Organic-Dye-Doped Silica Nanoparticles in a Reverse Microemulsion. Adv. Mater., 16 (2004) 173.

93. Z. Chaudhary, G.M. Khan, M.M. Abeer, N. Pujara, B. Wan-Chi Tse, M.A. McGuckin, A. Popat, and T. Kumeria, Efficient photoacoustic imaging using indocyanine green (ICG) loaded functionalized mesoporous silica nanoparticles. Biomater. Sci., 7 (2019) 5002.

94. M.M. Abeer, A.K. Meka, N. Pujara, T. Kumeria, E. Strounina, R. Nunes, A. Costa, B. Sarmento, S.Z. Hasnain, B.P. Ross, and A. Popat, Rationally designed dendritic silica nanoparticles for oral delivery of exenatide. Pharm., 11 (2019) 418.

95. A. Raza, F.B. Sime, P.J. Cabot, J.A. Roberts, J.R. Falconer, T. Kumeria, and A. Popat, Liquid CO_2 Formulated Mesoporous Silica Nanoparticles for pH-Responsive Oral Delivery of Meropenem, ACS Biomater. Sci. Eng., 7 (2021) 1836.

96. R.C. Soy, B. Babu, D.O. Oluwole, N. Nwaji, J. Oyim, E. Amuhaya, E. Prinsloo, J. Mack, and T. Nyokong, Photophysicochemical properties and photodynamic therapy activity of chloroindium (III) tetraarylporphyrins and their gold nanoparticle conjugates. J. Porphyr. and Phthalocyanines, 23 (2019) 34.

97. A. Kotiaho, R. Lahtinen, A. Efimov, H. Lehtivuori, N.V. Tkachenko, T. Kanerva, and H. Lemmetyinen, Synthesis and time-resolved fluorescence study of porphyrin-functionalized gold nanoparticles. J. Photochem. Photobiol. A: Chem., 212 (2010) 129.

98. R.C. Soy, D. Mafukidze, J. Mack, and T. Nyokong, The Photodynamic Antibacterial Activity Properties of a Series of Indium (III) Porphyrins and their Gold and Silver Nanoparticle Conjugates. Eur. J. Inorg. Chem., 27 (2024) 202400072.

99. O. Penon, M.J. Marín, D.A. Russell, and L. Pérez-García, Water soluble, multifunctional antibody-porphyrin gold nanoparticles for targeted photodynamic therapy. J. colloid interface Sci., 496 (2017) 100.

100. S.H. Cheng, C.H. Lee, C.S. Yang, F.G. Tseng, C.Y. Mou, C.Y. and L.W. Lo, Mesoporous silica nanoparticles functionalized with an oxygen-sensing probe for cell photodynamic therapy: potential cancer theranostics. J. Mater. Chem., 19 (2009) 1252.

101. E. Secret, M. Maynadier, A. Gallud, A. Chaix, E. Bouffard, M. Gary-Bobo, N. Marcotte, O. Mongin, K. El Cheikh, V. Hugues, and M. Auffan, Two-photon excitation of porphyrin-functionalized porous silicon nanoparticles for photodynamic therapy. Adv. Mater., 26 (2014) 7643.

102. A.C. Scanone, N.S. Gsponer, M.G. Alvarez and E.N. Durantini, Photodynamic properties and photoinactivation of microorganisms mediated by 5, 10, 15, 20-tetrakis (4-carboxyphenyl)

porphyrin covalently linked to silica-coated magnetite nanoparticles. J. Photochem. and Photobiol. A: Chem., 346 (2017) 452.

103. A.K. Paul, D.T. Jayaram, P.S. Babu, N. Adarsh, S. Thurakkal, A.S. Nair and D. Ramaiah, Synthesis and in vitro photobiological studies of porphyrin capped gold nanoparticles. J. Chem. Sci., 130 (2018) 1.

104. J. Wang, Y. Zhong, X. Wang, W. Yang, F. Bai, B. Zhang, L. Alarid, K. Bian, and H. Fan, pH-dependent assembly of porphyrin–silica nanocomposites and their application in targeted photodynamic therapy. Nano Lett., 17 (2017) 6916.

105. A.S. Oliveira, D. Licsandru, R. Boscencu, R. Socoteanu, V. Nacea, and L.F. Vieira Ferreira, A singlet oxygen photogeneration and luminescence study of unsymmetrically substituted mesoporphyrinic compounds. Int. J. Photoenergy, (2009) 413915.

106. S. Susmel, and C. Comuzzi, 5-Phenyl-dipyrromethane and 5-(4-pyridyl)-dipyrromethane as modular building blocks for bio-inspired conductive molecularly imprinted polymer (cMIP). An electrochemical and piezoelectric investigation. RSC Adv., 5 (2015) 78379.

107. A.E.F. Oliveira, A.C. Pereira, M.A. Resende, and L.F. Ferreira, Gold Nanoparticles: A Didactic Step-by-Step of the Synthesis Using the Turkevich Method, Mechanisms, and Characterizations. Analytica 4, (2023) 250.

108. E. Dube, D.O. Oluwole, and T. Nyokong, Improved Photophysical and Photochemical Properties of Thiopheneethoxy Substituted Metallophthalocyanines on Immobilization onto Gold-speckled Silica Nanoparticles. Photochem. Photobiol., 94 (2018) 521.

109. K.S. Lee, and M.A. El-Sayed, Gold and silver nanoparticles in sensing and imaging: Sensitivity of plasmon response to size, shape, and metal composition. J. Phys. Chem. B., 110 (2006) 19220.

110. T. Bürgi, Nanoscale Properties of the gold-sulphur interface: from self-assembled monolayers to clusters. Nanoscale, 7 (2015) 15553.

111. M. Protsiv, C. Ley, J. Lankester, T. Hastie, J. Parsonnet, Decreasing human body temperature in the United States since the Industrial Revolution. eLife, 9 (2020) 4955.

112. C. Hansch, P.P. Maloney, T. Fujita, and R.M. Muir, Correlation of biological activity of phenoxyacetic acids with Hammett substituent constants and partition coefficients. Nature, 194 (1962) 178.

113. C. Chakansin, J. Yostaworakul, C. Warin, K. Kulthong, and S. Boonrungsiman, Resazurin rapid screening for antibacterial activities of organic and inorganic nanoparticles: Potential, limitations and precautions. Anal. Biochem., 637 (2022) 114449.

114. S. Mondal, T. Pain, K. Sahu, and S. Kar, Large-Scale Green Synthesis of Porphyrins. ACS Omega, 6 (2021) 22922.

115. Y. Nakamura, N. Aratani, K. Furukawa, and A. Osuka, Synthesis and characterizations of free base and Cu(II) complex of a porphyrin sheet. Tetrahedron, 64 (2008) 11433.

116. B.W. Atwater, Substituent effects on the excited-state properties of platinummeso-tetraphenylporphyrins. J. Fluoresc., 2 (1992) 237.

117. A. Giraudeau, H.J. Callot, and M. Gross, Effects of Electron-Withdrawing Substituents on the Electrochemical Oxidation of Porphyrins, Inorg. Chem., 18 (1979) 201.

118. T. Bürgi, Properties of the gold–sulphur interface: from self-assembled monolayers to clusters. Nanoscale. 7 (2015) 15553. https://doi.org/10.1039/C5NR03497C.

119. H. Patrick, P. Tobias, A. Florian, P. Andre, V. Johannes, V. Daniel, W. Gregor, V.R. Wolfang, O. Joachim, and W. Stefan, Exploration of MOF nanoparticles sizes using various physical characterization methods - is what you measure what you get?. Cryst Eng. Comm., 23 (2016) 4359.

120. M. Danaei, M. Dehghankhold, S. Ataei, F. Hasanzadeh Davarani, R. Javanmard, A. Dokhani, S. Khorasani, and M.R. Mozafari, Impact of particle size and polydispersity index on the clinical applications of lipidic nanocarrier systems. Pharmaceutics, 10 (2018) 57.

121. I. Ostolska, and M. Wi´sniewska, Application of the zeta potential measurements to explanation of colloidal Cr2O3 stability mechanism in the presence of the ionic polyamino acids. Colloid Polym. Sci., 292 (2014) 2453.

122. Y. Mikhlin, M. Likhatski, Y. Tomashevich, A. Romanchenko, S. Erenburg, and S. Trubina, XAS and XPS examination of the Au-S nanostructures produced via the reduction of aqueous gold(III) by sulfide ions. J. Electron Spectrosc. Relat. Phenom., 177 (2010) 24.

123. J. Chastain, and R.C. King jr, Handbook of X-ray photoelectron spectroscopy. Perkin-Elmer Corporation, 40 (1992) 221.

124. M. Morisue, I. Ueno, T. Nakanishi, T. Matsui, S. Sasaki, M. Shimizu, J. Matsui, and Y. Hasegawa, Amorphous porphyrin glasses exhibit near-infrared excimer luminescence. RSC Adv., 7 (2017) 22679.

125. S.P. Dubey, M. Lahtinen, and M. Sillanpää, Tansy fruit mediated greener synthesis of silver and gold nanoparticles. Process Biochem., 45 (2010) 1065.

126. T.G.F. Souza, V.S.T. Ciminelli, and N.D.S. Mohallem, A comparison of TEM and DLS methods to characterize size distribution of ceramic nanoparticles, J. Phys. Conf. Ser., 733 (2016) 012039.

127. V. Polshettiwar, D. Cha, X. Zhang, and J.M. Basset, High-surface-area silica nanospheres (KCC-1) with a fibrous morphology. Angew. Chem. Int. Ed., 49 (2010) 9652.

128. M. Bouhrara, C. Ranga, A. Fihri, R.R. Shaikh, P. Sarawade, A.H. Emwas, M.N. Hedhili, and V. Polshettiwar, Nitridated fibrous silica (KCC-1) as a sustainable solid base nanocatalyst. ACS Susain. Chem. Eng., 1 (2013) 1192.

129. K. Yue, J. Nan, X. Zhang, J. Tang, and X. Zhang, Photothermal effects of gold nanoparticles induced by light emitting diodes. Appl. Therm. Eng., 99 (2016) 1093.

130. M.C. DeRosa, and R.J. Crutchley, Photosensitized singlet oxygen and its applications, Coord. Chem. Rev., 233 (2002) 351.

131. A.P. Castano, T.N. Demidova, and M.R. Hamblin, Mechanisms in photodynamic therapy: part one—photosensitizers, photochemistry and cellular localization. Photodiagnosis. Photodyn. Ther., 1 (2004) 279.

132. T. Nyokong, E. Antunes, The Handbook of Porphyrin Science. Kadish K.M., Smith R.M., Guilard R.M. World Scientific, Singapore, 7 (2010).

133. M. Taniguchi, J.S. Lindsey, D.F. Bocian, and D. Holten, Comprehensive review of photophysical parameters (ε, Φf, τs) of tetraphenylporphyrin (H2TPP) and zinc tetraphenylporphyrin (ZnTPP)–Critical benchmark molecules in photochemistry and photosynthesis. J. Photochem. Photobiol. C: Photochem. Rev., 46 (2021) 100401.

134. E.S. Nyman, and P.H. Hynninen, Research advances in the use of tetrapyrrolic photosensitizers for photodynamic therapy. J. Photochem. Photobiol. B., 73 (2004) 1.

135. A. Martinez De Pinillos Bayona, P. Mroz, C. Thunshelle, and M.R. Hamblin, Design features for optimization of tetrapyrrole macrocycles as antimicrobial and anticancer photosensitizers. Chem. Biol. Drug Des., 89 (2017) 192.

136. D. Alba-Molina, M.T. Martín-Romero, L. Camacho, and J.J. Giner-Casares, Ion-mediated aggregation of gold nanoparticles for light-induced heating. Appl. Sci., 7 (2017) 916.

137. S.A. Sibani, P.A. McCarron, A.D. Woolfson, and R.F. Donnelly, Photosensitiser delivery for photodynamic therapy. Part 2: systemic carrier platforms. Expert Opin. Drug Deliv., 5 (2008) 1241.

138. B.K. Jalali, S.S. Shik, L. Karimzadeh–Bardeei, E. Heydari, and M.H.M. Ara, Photothermal treatment of glioblastoma cells based on plasmonic nanoparticles. Lasers Med. Sci., 38 (2023) 122.

139. J.C. Maziere, R. Santus, P. Morliere, J.P. Reyftmann, C. Candide, L. Mora, S. Salmon, C. Maziere, S. Gatt, L. Dubertret, Cellular uptake and photosensitizing properties of anticancer porphyrins in cell membranes and low and high density lipoproteins. J. Photochem. Photobiol. B: Biol., 6 (1990) 61.

140. B.M. Amos-Tautua, O.J. Fakayoe, S. Vuuren, S.P. Songca, and O.S. Oluwafemi, Non-distorted visible light-absorbing thiol-PEGylated gold-coated superparamagnetic iron oxide nanoparticles–porphyrin conjugates and their inhibitory effects against nosocomial patho, MRS Commun., 9 (2019) 1335.

141. E. Alves, L. Costa, C.M.B. Carvalho, J.P. Tomé, M.A. Faustino, M.G. Neves, A.C. Tomé, J.A. Cavaleiro, A. Cunh, and A. Almeida, Charge effect on the photoinactivation of gram-negative and gram-positive bacteria by cationic meso-substituted porphyrins, BMC Microbiol., 9 (2009) 70.

142. T. Ito, X.X. Ma, F. Takeuchi, K. Okuma, H. Yuzawa, and K. Hiramatsu., Novel type V staphylococcal cassette chromosome mec driven by a novel cassette chromosome recombinase, ccrC. Antimicrob. Agents Chemother., 48 (2004) 2637.

143. Y. Katayama, T. Ito, and K. Hiramatsu, A new class of genetic element, staphylococcus cassette chromosome mec, encodes methicillin resistance in *Staphylococcus aureus*. Antimicrob. Agents Chemother., 44 (2000) 1549.

Appendix

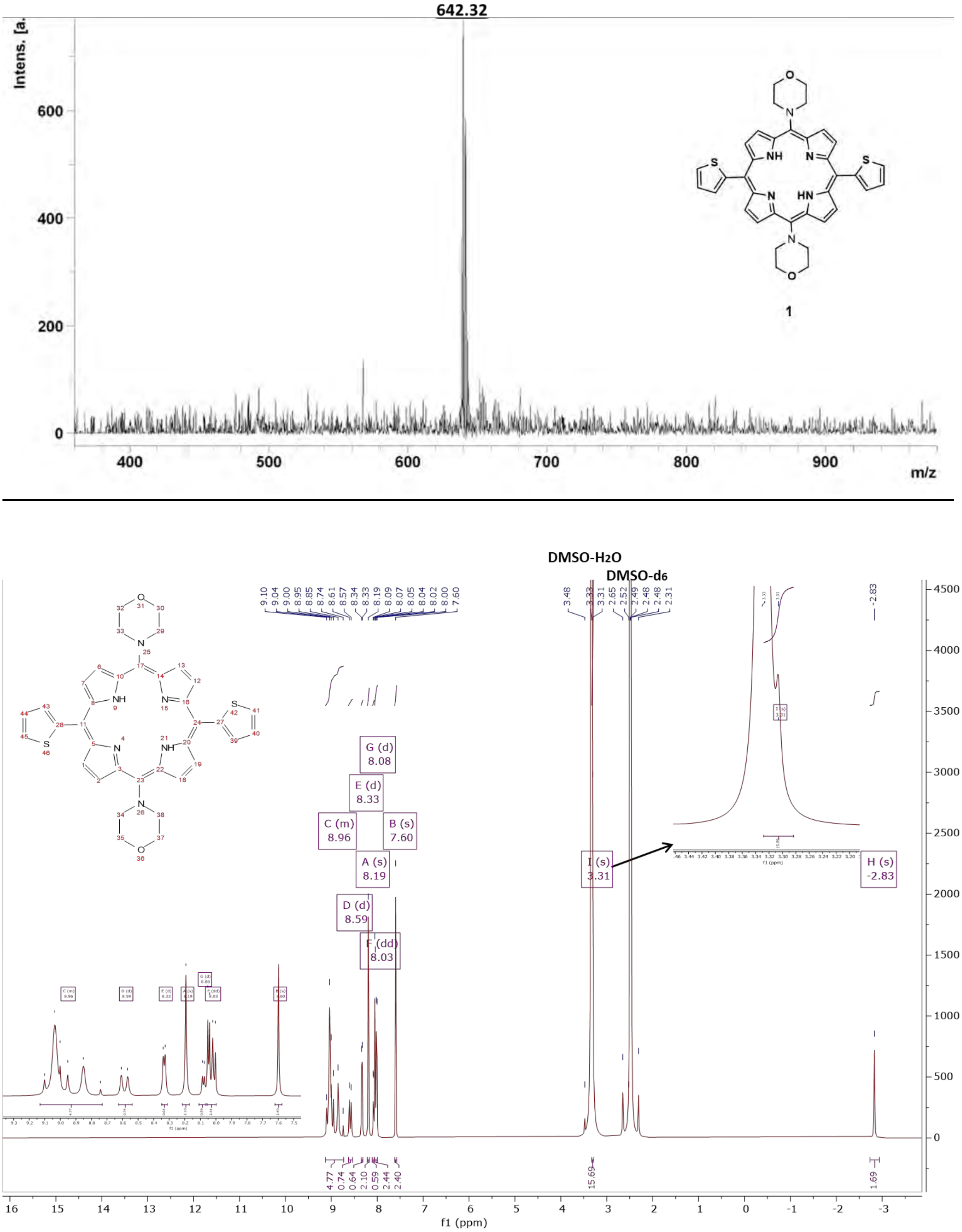

Fig. A1. MALDI-TOF MS data for complex **1** using α-cyano-4-hydroxycinnamic acid as the matrix and ^{1}H NMR in DMSO-d$_6$.

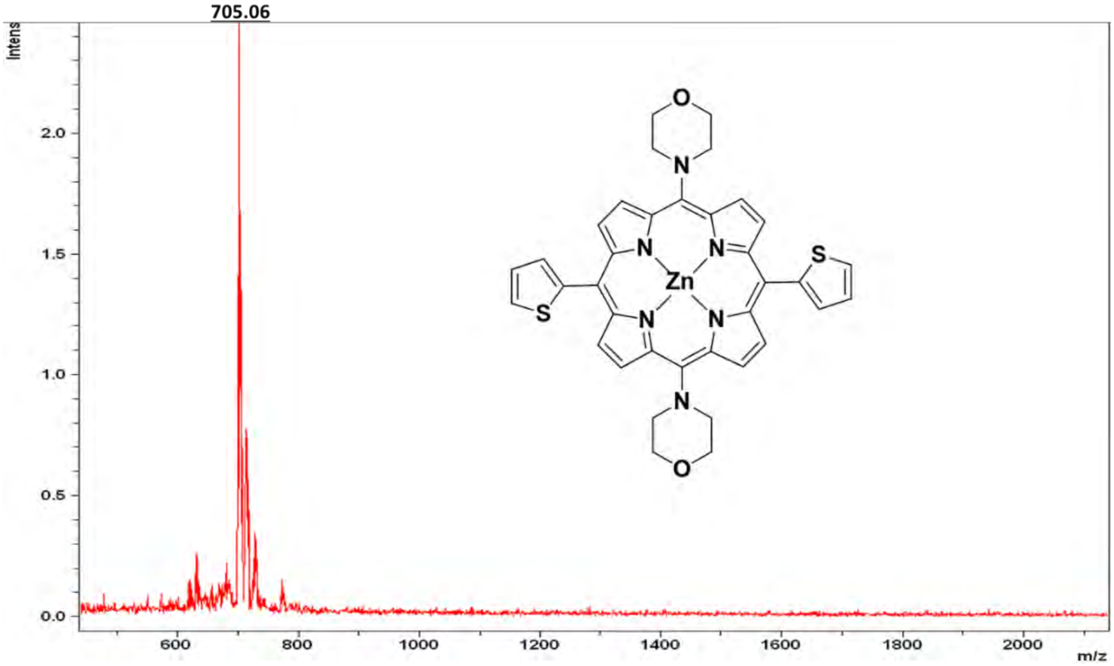

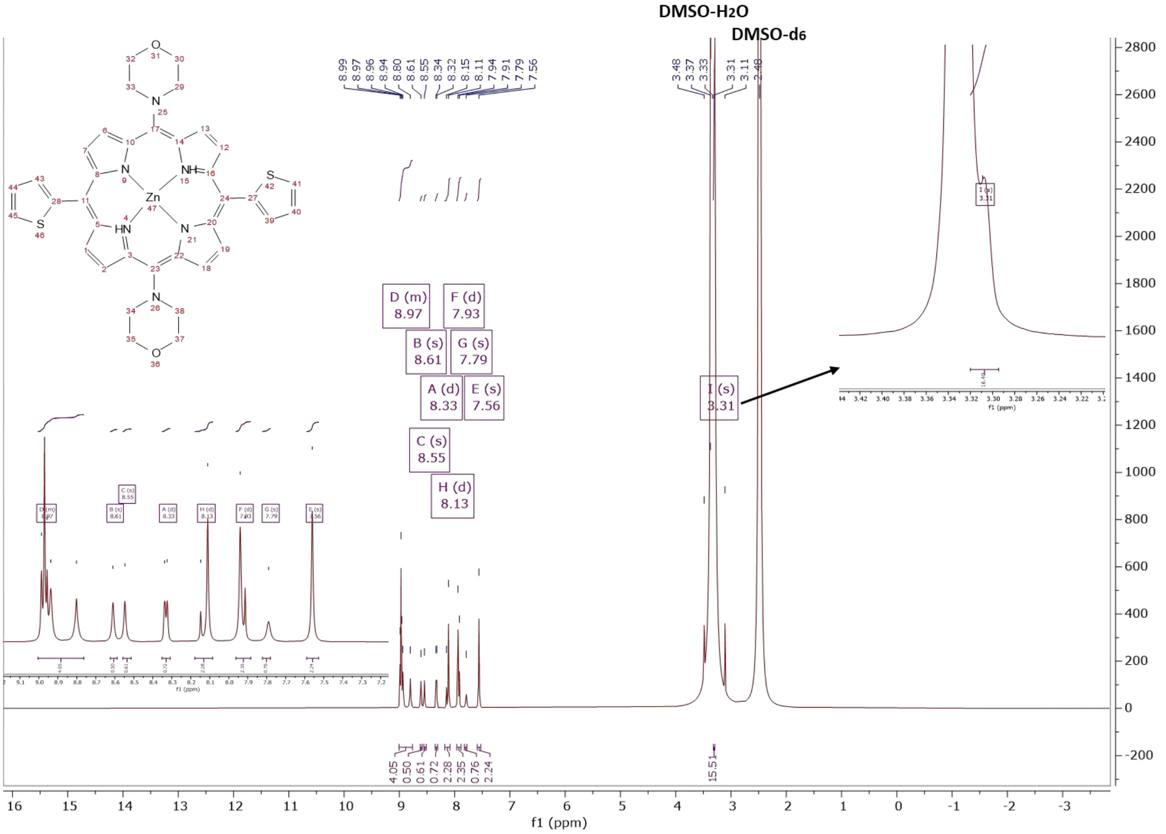

Fig. A2. MALDI-TOF MS data for complex **2** using α-cyano-4-hydroxycinnamic acid as the matrix and 1H NMR in DMSO-d_6.

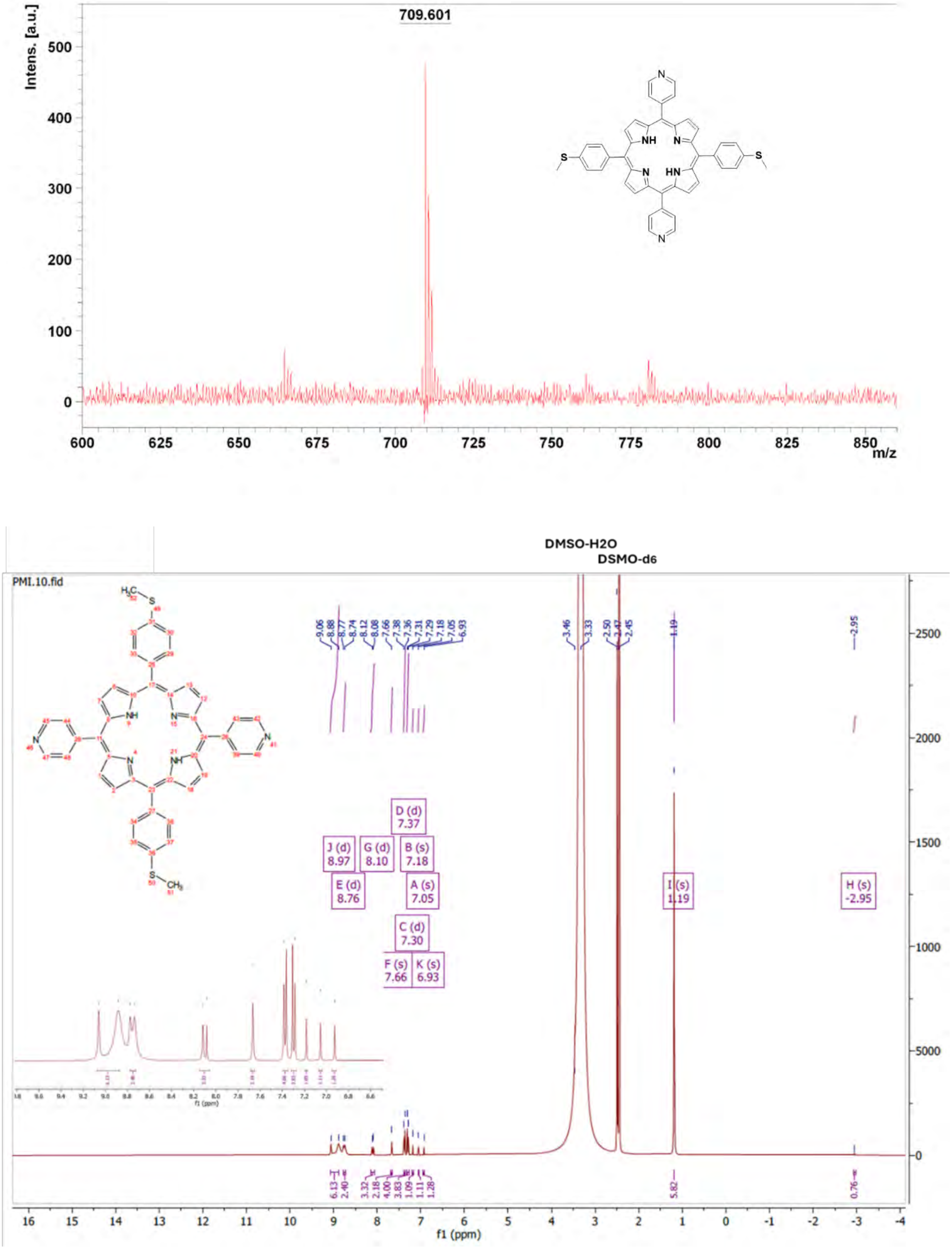

Fig. A3. MALDI-TOF MS data for Complex **3** using α-cyano-4-hydroxycinnamic acid as the matrix and ^{1}H NMR in DMSO-d$_6$.

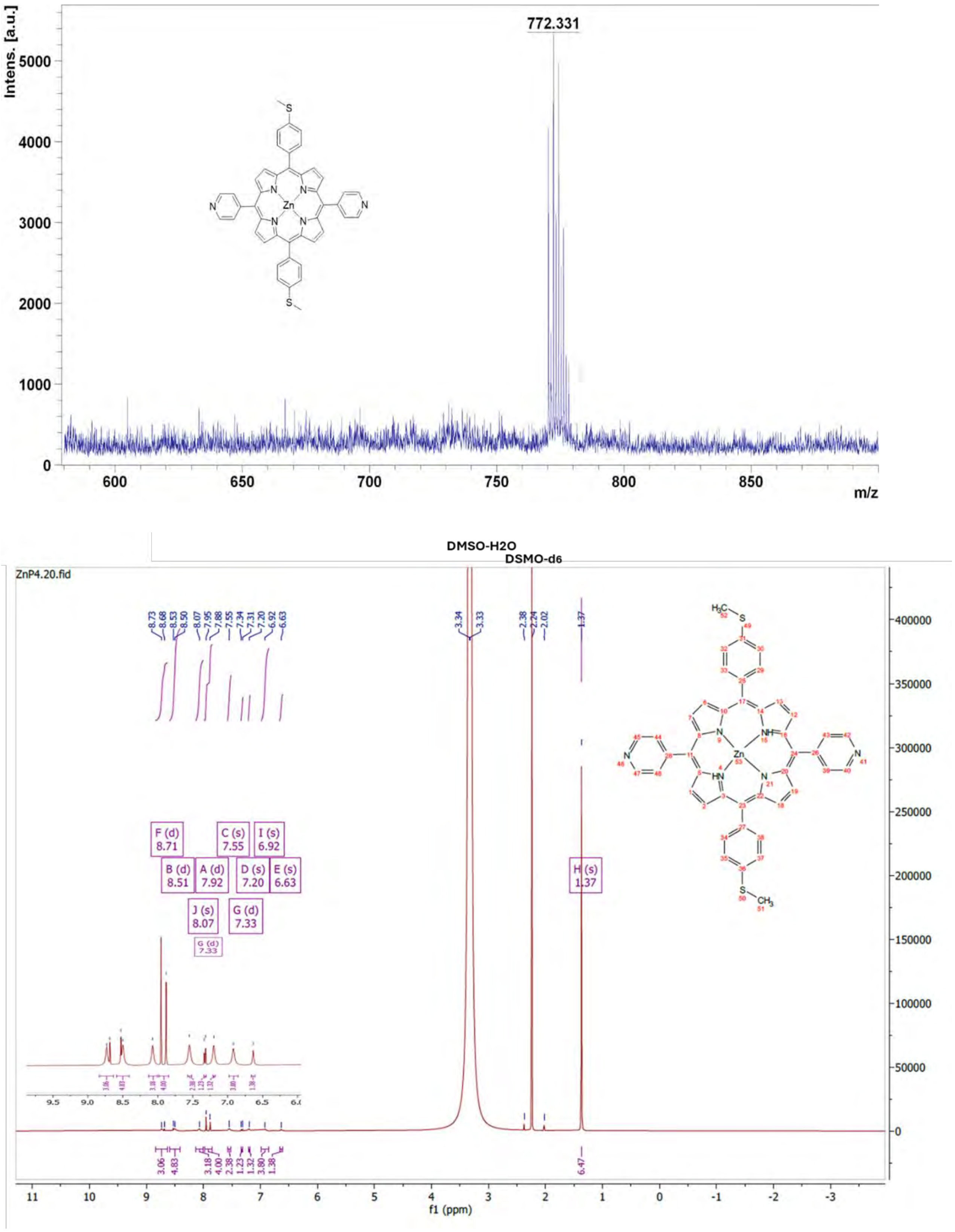

Fig. A4. MALDI-TOF MS data for complex **4** using α-cyano-4-hydroxycinnamic acid as the matrix and ^{1}H NMR in DMSO-d$_6$.